RESONANT X-RAY DIFFRACTION FROM CHARGE DENSITY WAVES IN 1-T TANTALUM DISULFIDE

A Dissertation

Presented to the Faculty of the Graduate School

of Cornell University

in Partial Fulfillment of the Requirements for the Degree of

Doctor of Philosophy

by

Jun-Dar Su

May 2008

RESONANT X-RAY DIFFRACTION FROM CHARGE DENSITY WAVES IN 1-T TANTALUM DISULFIDE

Jun-Dar Su, Ph.D.

Cornell University 2008

By tuning the incident x-ray energy close to the Ta-L_3 edge, we studied resonant (elastic) x-ray diffraction (RXD) from the charge density waves (CDWs) of 1T-TaS_2. Our goal was to separate the scattering from the periodic modulation of the conduction electron density and from that of the lattice distortion wave. In addition to resonant diffraction studies, various x-ray techniques, including XANES, polarization analysis, and a temperature study, were utilized. We find that two physical effects prevent separating the CDW charge modulation scattering at the primary CDW satellites $\mathbf{G} \mp \mathbf{k}_{\mathrm{CDW}}$ using energy or polarization. (i) The core-hole lifetime of the Ta-L_3 resonance is much larger than the CDW band gap in 1T-TaS_2 and smears out the CDW anomaly in the electronic density of states. (ii) Resonant scattering from Ta 5d band states not associated with the CDW dominates over resonant scattering from the charge modulation, smearing out the polarization signature. Our results highlight the principles of RXD when the technique is used to study novel states found in the conduction bands of transition metal compounds and point out which types of systems are most promising.

BIOGRAPHICAL SKETCH

Jun-Dar Su was born in Taipei, Taiwan, in 1976. His interest about science was first initiated by his mother, Suling Yu, who used to take Jun-Dar to her lab at the university. Jun-Dar can still vividly remember the demonstration he saw at an age of five about a titration experiment. Jun-Dar's father, Shih-Wen Su, focused more on Jun-Dar's education on literature and history, which soon became Jun-Dar's favorite subjects in school. As he grew, Jun-Dar learned to look deep into the reasons of every question he could possibly asked and found. Luckily he met many good teachers and friends in his high school and his college. Together they studied history, mathematics, and physics, and Jun-Dar began to learn Newton, Maxwell, and Boltzmann. At Cornell Jun-Dar got a chance to teach in two undergraduate courses. While enjoying sharing with others what he has known about the governing laws of nature, he continuously felt this tremendous need to learn more about what he has not known. Ultimately Jun-Dar wants to pursuit his career is academia, perhaps to address the problem of why life is such a complex system that can really work. Being an experimentalist, Jun-Dar is really happy about the training he have received. He will continue his journey by looking for the answers to those questions on his list, and he knows there will always be Mother Nature watching his quest of truth.

To my parents and Yibi

ACKNOWLEDGEMENTS

The research work could not have succeeded without the help from many people to whom I am deeply indebted. I would like express my most sincere gratitude to my thesis advisor, Professor Joel Brock, who always provided me with so many opportunities and freedom to explore the world of physics. No matter how busy he was, his door was always open to us for any discussion. I have learned not just science from Joel. Should someday I become a qualified person in my own research, his image as an intellectual will be what I have been trying to emulate on myself.

I would also like to thank my dearest colleague, friend, and advisor, Dr. Ken Finkelstein, for teaching why we enjoy research so much (among many other things). Earlier this year, I found Ken and I frequently ran into each other every time I was out for a walk in this beautiful springtime. Ken was driving, but he would stop. We talked, not just saying hi. Those were my most memorable days on this beloved campus, Cornell.

Many thanks to Professor Rob Thorne, who provided not only the best crystals in the world but also the critical encouragement while I was finishing this study about the CDWs.

I would also like take this chance to acknowledge my fellow graduate student colleagues: Gökhan Arikan, John Ferguson, and Robin Sampson, for all the discussions and help in the past years. I benefit from Robin's earlier study on $1T$-TaS_2, which was really where this project began to take off.

I am further indebted to Professor Sol Gruner, Arthur Woll, Aaron Fleet, and Darren Dale. Whenever I became in doubt about where I was going, they gave me the valuable advice and help me to continue.

We began this research project without knowing much about resonant x-ray

diffraction. We have worked with many very best researchers in this field. I am grateful to Dr. John Hill for his generous help at NSLS when we went there for the experiment. I would like to thank Dr. Peter Abbamonte for sharing with us his insight about resonant x-ray scattering. Additional thanks go to Dr. Mark Sutton, who taught me to study the CDW speckles.

I would like to thank the CHESS staff. Without their help, the experimental work of this study could not have be completed.

Most of all, I would like to express my deepest gratitude to my family and Yibi, whose endless love have given me strength to pursue my goal. I am deeply indebted to my late grandmother for the many sacrifices she has made for me.

TABLE OF CONTENTS

LIST OF TABLES

LIST OF FIGURES

LIST OF ABBREVIATIONS

CDW	charge density wave
CMW	charge modulation wave
LDW	lattice distortion wave
XANES	X-ray Absorption Near-edge Structure
DOS	density of states
STM	scanning tunneling microscopy
FLR	Fukuyama-Lee-Rice
IC -	incommensurate - (phase)
NC -	nearly-commensurate - (phase)
C -	commensurate - (phase)
LBCO	$La_{2-x}Ba_xCuO_4$
MCP	mobile carrier peak
UHB	upper Hubbard band
LTT	low-temperature tetragonal (phase)
SCDW	surface charge density wave
BZ	Brillouin zone

LIST OF SYMBOLS

$\mathbf{r}$	position vector/operator
$\mathbf{p}$	momentum operator of electron
$\mathbf{q}$ $(\mathbf{q}')$	wavevector of incident (scattered) x-rays
$\mathbf{Q}$	scattering vector
$\mathbf{k}$	wavevector of electrons
$\mathbf{k}_{\text{CDW}}$	CDW wavevector
$\mathbf{k}_F$	wavevector at the Fermi surface
$\mathbf{R}$	lattice coordinate
$\mathbf{a}_0, \mathbf{b}_0, \mathbf{c}_0$	lattice vector of crystal
$\mathbf{G}$	reciprocal lattice
$\mathbf{a}_0^*, \mathbf{b}_0^*, \mathbf{c}_0^*$	reciprocal lattice vector of crystal
ω	x-ray frequency
$\hat{\text{e}}$	polarization vector
Γ	core-hole lifetime/classical damping coefficient
N	number of unit cells in a lattice
$U_{\mathbf{k}}, V_{\mathbf{k}}$	coefficients of the Bogoliubov transformation
v_c	volume of unit cells
$\widetilde{g}_{\mathbf{q}}$	coupling constant in Peierls' model
b	asymmetry parameter
z_0	sample thickness
ε_0	permittivity of free space
$\hbar$	Planck's constant divided by 2π
k_B	Boltzmann constant
c	speed of light
r_0	classical electron radius
e	electron charge
m_e	electron mass
M	ion mass
λ	wavelength of x-rays
$\mathbf{E}$	electric field
I	x-ray intensity
ϵ	electron energy
$E(\mathbf{k})$	dispersion relation of the CMW
ρ_1	magnitude of the CMW
ρ_e (ρ_a)	electronic density distribution of an electron (atom)
$\mathbf{u}_0$	magnitude of the LDW
$\Delta\mathbf{u}_0$	atomic displacement
ϕ_E	phase of the CMW
ϕ_L	phase of the LDW
$\{\mathbf{k}\}$	set of wavevectors involved in the state reconstruction of a CDW
Δ	CDW gap/order parameter
W	transition rate

T^{MF}	CDW critical temperature in the mean-field theory
T^{3D}	CDW critical temperature in the three-dimensional model
ϱ (N_e)	electronic DOS after (before) the formation of the CDW state
ϱ^{γ}	DOS of photons
η	extinction depth
$\omega_{\mathrm{D}}^{\mathrm{total}}$	angular Darwin width
σ^{ab}	absorption cross-section
f^0	atomic form factor
f' (f'')	real (imaginary) part of a dispersion correction
f	atomic form factor with the dispersion correction
$\tilde{f}_{\alpha\beta}$	CMW modulation of the atomic form factor
$\mathbf{T}$	atomic form factor tensor
F	structure factor
$\tilde{F}$	modulated structure factor
ψ	Bloch wave function
ϕ	atomic orbital
ρ_{CDW}	CDW charge density
μ	absorption coefficient
μ_r	relative absorption coefficient
$a_{\mathbf{k}}^{\dagger}$ $(a_{\mathbf{k}})$	creating (annihilation) operator for the electron $\mathbf{k}$
$b_{\mathbf{q}}^{\dagger}$ $(b_{\mathbf{q}})$	creating (annihilation) operator for the phonon $\mathbf{q}$

CHAPTER 1

INTRODUCTION

The goal of this thesis is to measure the spatial structure of novel quantum mechanical states of the valence electrons in condensed matter. In particular, I am interested in delocalized states and their collective excitations, as they form the backbone of today's discussion in condensed-matter physics. Examples of novel quantum mechanical states include the superconducting ground state [1], the quantum Hall ground state [2], and various types of density waves [3]. I chose to work with charge density waves (CDWs) for they are relatively well understood systems.

The CDW state is the ground state of lower-dimensional conductors. Due to the unique geometry of the Fermi surfaces, electrons can develop strong correlations in lower dimensions [4, 6]. The valence electrons form a periodic structure on the otherwise flat charge density. Figure 1.1(a) is a STM image of a two-dimensional CDW [4]. As far as the underlying lattice is concerned, the CDW also entails a modulation of the atomic positions. The lattice has become distorted. Accordingly the system is found in a novel state, which is indeed spontaneous, and both the lattice and the conduction band charge density are modulated with a single spatial frequency. With respect to a metallic state, this new state is energetically favorable. It is referred to as the CDW ground state [7]. A very useful theory that describes the CDW state based on the idea of electron-lattice interactions is the Peierls theory. Interested readers are referred to Ref. [1] for a formal discussion about the formation of CDWs and the other associated phenomena.

Throughout this dissertation, we will call the charge modulation and the lattice distortion as the charge modulation wave (CMW) and the lattice distortion wave (LDW), respectively. In this language, waves are nothing but spatial variations with well-defined periodicities. Let us then use $\mathbf{k}_{\mathrm{CDW}}$ to denote the wavevector. In

(a)

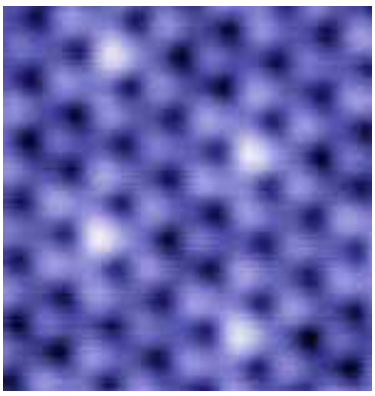

(b)

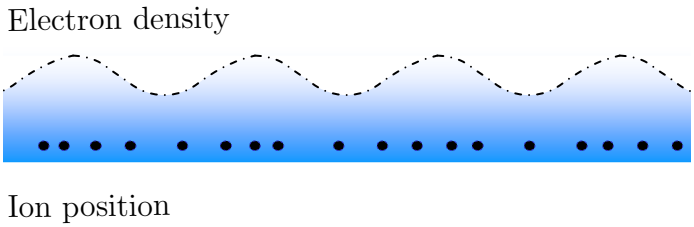

Figure 1.1: (a) A two-dimensional CDW [4]. The STM measures the spatial distribution of the *filled* states on the surface of $2H$-$NbSe_2$. The bright spots correspond to a high density of electrons. The periodic structure formed by the electrons is clearly seen in this superb image. (b) A schematic CDW in one-dimension. Both the lattice distortion wave and the charge modulation wave share the same period equal to approximately five times of the lattice constant.

one dimension [3], our CDW, which we shall assume to be sinusoidal, consists of two separate components:

$$\rho_{\rm CDW}(\mathbf{x}) = \rho_1 \cos\Big(\mathbf{k}_{\rm CDW}\cdot\mathbf{x} + \phi_E(\mathbf{x})\Big) \quad \text{(CMW)} \tag{1.1}$$

$$\Delta\mathbf{u}_n = \mathbf{u}_0 \sin\Big(\mathbf{k}_{\rm CDW}\cdot na + \phi_L(\mathbf{x})\Big) \quad \text{(LDW)} \tag{1.2}$$

where we have assumed the lattice constant is a. Figure 1.1(b) depicts a physical situation with $k_{\rm CDW} \approx \dfrac{2\pi}{5a}$. For the LDW, $\Delta\mathbf{u}_n$ is the displacement of the atom sitting at the nth lattice site. The distorted lattice can be reconstructed by adding the displacements to the original lattice coordinates: $\mathbf{u}_n = na + \Delta\mathbf{u}_n$. Under the assumption of sufficiently low temperature, the amplitudes ρ_1 and $\mathbf{u}_0$ are considered to be constants [3]. Yet the CMW and the LDW can both still be modulated through their phases. In Eq (1.1) and (1.2) we have taken this into account by having the phases ϕ_E and ϕ_L be position-dependent functions.

We shall now discuss the physical significance of the two independent phase functions. When $\phi_E = \phi_L$, the CMW has its maximum coincide with the ionic density maximum due to the LDW. In this case, the CDW is in a low-energy state; the CMW and the LDW achieve electrostatic equilibrium. Such an idea of CMW-LDW equilibrium can then be generalized. We like to think of an unbalanced phase relation $\phi_E \neq \phi_L$ as corresponding to the CDW being out of thermal equilibrium[1]. Non-equilibrium may come up in CDW transport [2, 12]. As an experimental group, we have indeed utilized x-ray to study CDWs in the mode-locked [13] state. Curiously, our x-ray diffraction measurements failed to observe any structural response of the LDW associated with the dramatic electronic ordering of the CMW. Similarly, we failed to observe any LDW re-ordering at high

[1]CDW's potential of being a non-equilibrium system has not been really addressed in today's discussions. Models based on the mean-field-theory result, such as the FLR theory [9, 10], incorporate a single phase for both the CMW and the LDW.

speeds[2] [17, 18]. One possible explanation is in those situations the CMW and the LDW did not stay in equilibrium and actually exhibit distinct spatial structures. Therefore the phases in Eq (1.1) and (1.2) are considered to be separate functions. To us, then the question is whether the two different phases can be measured separately. While x-ray diffraction is useful to determine ϕ_L [7, 8], the CMW is such a small charge density variation that there is no way we can determine ϕ_E using conventional x-ray diffraction. On the other hand, resonant x-ray scattering has already demonstrate its potential to study the quantum states found in various systems [10, 5, 23]. Quite naturally we would ponder whether we can apply the resonant x-ray diffraction technique to our CDW study.

In this thesis, I investigate resonant x-ray scattering due to the CDW of $1T$-TaS_2. Using the tight-binding description of valence bands, I developed a theory of resonant x-ray scattering. According to the theory, the CMW and the LDW can both create x-ray diffraction. I pointed out that a direct measurement of the spatial structure of the CMW should be performed at the primary CDW diffraction satellites. At those special positions, the cross-section of x-ray scattering is[3]

$$\left(\frac{d\sigma}{d\Omega}\right)_{\text{CDW}}^{\mathbf{Q}\sim\mathbf{G}^{\mp}} = Nr_0^2\Big(|f(\omega)|^2 \cdot |J_1(\mathbf{Q}\cdot\mathbf{u}_0)|^2 \sum_{\mathbf{R}} e^{i\mathbf{Q}^{\pm}\cdot\mathbf{R}} e^{-\frac{1}{2}\mathcal{G}_L(\mathbf{R})} + |\tilde{f}(\omega)|^2 \cdot \frac{|J_0(\mathbf{Q}^{\pm}\cdot\mathbf{u}_0)|^2}{4} \sum_{\mathbf{R}} e^{i\mathbf{Q}^{\pm}\cdot\mathbf{R}} e^{-\frac{1}{2}\mathcal{G}_E(\mathbf{R})} \Big) \qquad (1.3)$$

On the right hand side of this equation, the two separate terms represent the LDW contribution and the CMW contribution to x-ray scattering, respectively. Each contribution corresponds to its own lineshape of diffuse scattering characterized by $\mathcal{G}(\mathbf{R})$ — the spatial correlation functions of the corresponding phases. Based on this result, the study of this thesis has been focused on measuring $\tilde{f}$, which

[2] It needs to be added that a motionally ordered CDW was indeed advocated in a reported x-ray diffraction measurement on $NbSe_3$. Meanwhile, we remain to be cautious about the result as the same effect can be due to sample and contact imperfection. See Ref. [14, 15, 16].

[3] A detailed discussion, including the derivation, is given in Appendix B.

is the CMW modulated component of the atomic form factor, versus f, which is the atomic form factor of the resonating atoms. Using the standard CDW theory (Peierls model), I showed that $\tilde{f}$ can exist only if resonant x-ray scattering occurs via those states around the edge of the CDW gap. Experimentally, I utilized several different methods, including XANES (x-ray absorption near-edge structure), polarization analysis, and temperature study, to test and confirm the effect of $\tilde{f}$. After all, it was found that the core-hole lifetime of the atomic transitions plays an important role in resonant x-ray scattering. In order to make x-ray sensitive to the CMW, the natural width of the atomic transitions must match the size of the CDW energy gap. In the experiments, different phenomena of resonant x-ray scattering, including both x-ray absorption and x-ray diffraction, were carefully studied for $1T$-TaS_2 at the Ta-L_3 edge. Indeed, the experimental results can all be understood using my theory of resonant x-ray scattering.

This dissertation is organized as follows: In the second chapter I will discuss the theory of x-ray scattering. I will describe resonant x-ray scattering using both classical electrodynamics and the quantum mechanical descriptions. Special emphasis will be placed on scattering by solids rather than by individual atoms. In Chapter 3, I will describe the CDW phenomenon. The discussion is based on the Peierls theory of CDWs. The physical properties of the CDW in $1T$-TaS_2 will also be studied in detail. I then incorporate the CDW state into the formalism of x-ray scattering in Chapter 4, where the CDW effect in x-ray diffraction will be addressed. This chapter lays the foundation for our discussions of the experimental findings presented in the rest of the thesis. I use Chapter 5 to discuss my experiments on the x-ray absorption spectra of $1T$-TaS_2. From the results of these crucial measurements, we specify the nature of the scattering problem we are dealing with. In Chapter 6, I present the results of our x-ray diffraction experiments

for both the CDW and the intrinsic crystal structure of $1T$-TaS_2. It is shown that our theory accurately describes the experimental data. In the last chapter of this dissertation, I will compare our experiments with resonant x-ray scattering found in other systems. The discussion addresses the nature of the CDW system as well as resonant x-ray scattering itself. Appendix A is a brief review of x-ray scattering in quantum mechanics. In Appendix B, I describe diffuse resonant x-ray scattering, taking into account the finite spatial correlation of the CDW. Important x-ray properties in our experiments are discussed in Appendix C.

BIBLIOGRAPHY

[1] Michael Tinkham. *Introduction to Superconductivity*. McGraw-Hill Book Co., New York, 1975. Reading.

[2] Klaus von Klitzing. The quantised hall effect. *Rev. Mod. Phys.*, 58:519, 1986.

[3] G. Grüner. *Density Waves in Solids*. Addison-Wesley, MA, 1994. Reading.

[4] S. H. Pan, E. W. Hudson, and J. C. Davis. ^{3}He refrigerator based very low temperature scanning tunneling microscope. *Rev. Sci. Instrum.*, 70:1459–1463, Feb 1999.

[5] Neil W. Ashcroft and N. David Mermin. *Solid State Physics*. Harcourt, Inc., FL, 1976. Discussion of the Lindhard theory.

[6] Jean Rouxe. *Crystal chemistry and properties of materials with quasi-one-dimensional structures*. D Reidel Publishing Company, Dordrecht, Holland, 1986. Chapter 1.

[7] R. E. Thorne. Charge-density-wave conductors. *Physics Today*, 49:42–47, May 1996.

[8] R. E. Peierls. *Quantum Theory of Solids*. Oxford University Press, Oxford, 2001. Reading.

[9] H. Fukuyama and P. A. Lee. Dynamics of the charge-density wave. i. impurity pinning in a single chain. *Phys. Rev. B*, 17(2):535–541, Jan 1978.

[10] P. A. Lee and T. M. Rice. Electric field depinning of charge density waves. *Phys. Rev. B*, 19(8):3970–3980, Apr 1979.

[11] H. Fröhlich. On the theory of superconductivity: the one-dimensional case. *Proceedings of the Royal Society London, Series A*, 223(1154):296–305, May 1954.

[12] P. Monceau, J. Richard, and M. Renard. Interference effects of the charge-density-wave motion in $NbSe_3$. *Phys. Rev. Lett.*, 45(1):43–46, Jul 1980.

[13] G. Grüner. The dynamics of charge-density waves. *Rev. Mod. Phys.*, 60(4):1129–1181, Oct 1988.

[14] R. Danneau, A. Ayari, D. Rideau, H. Requardt, J. E. Lorenzo, L. Ortega, P. Monceau, R. Currat, and G. Grübel. Motional ordering of a charge-density wave in the sliding state. *Phys. Rev. Lett.*, 89(10):106404, Aug 2002.

[15] Robert E. Thorne, Joel D. Brock, and Mark Sutton. Comment on "motional ordering of a charge-density wave in the sliding state". *Phys. Rev. Lett.*, 91(4):049703, Jul 2003.

[16] R. Danneau, A. Ayari, D. Rideau, H. Requardt, J. E. Lorenzo, L. Ortega, P. Monceau, R. Currat, and G. Grübel. Danneau et al. reply:. *Phys. Rev. Lett.*, 91(4):049704, Jul 2003.

[17] K. L. Ringland, A. C. Finnefrock, Y. Li, J. D. Brock, S. G. Lemay, and R. E. Thorne. Sliding charge-density waves as rough growth fronts. *Phys. Rev. B*, 61(7):4405–4408, Feb 2000.

[18] Leon Balents and Matthew P. A. Fisher. Temporal order in dirty driven periodic media. *Phys. Rev. Lett.*, 75(23):4270–4273, Dec 1995.

[19] E. Sweetland, C-Y. Tsai, B. A. Wintner, J. D. Brock, and R. E. Thorne. Measurement of the charge-density-wave correlation length in $NbSe_3$ by high-resolution x-ray scattering. *Phys. Rev. Lett.*, 65(25):3165–3168, Dec 1990.

[20] J. D. Brock, A. C. Finnefrock, K. L. Ringland, and E. Sweetland. Detailed structure of a charge-density wave in a quenched random field. *Phys. Rev. Lett.*, 73(26):3588–3591, Dec 1994.

[21] Doon Gibbs, D. R. Harshman, E. D. Isaacs, D. B. McWhan, D. Mills, and C. Vettier. Polarization and resonance properties of magnetic x-ray scattering in holmium. *Phys. Rev. Lett.*, 61(10):1241–1244, Sep 1988.

[22] P. Abbamonte, A. Rusydi, S. Smadici, G. D. Gu, G. A. Sawatzky, and D. L. Feng. Spatially modulated 'Mottness' in $L_{2-x}B_xCO_4$. *Nature Physics*, 1:155–158, December 2005.

[23] P. Abbamonte, G. Blumberg, A. Rusydi, A. Gozar, P. G. Evans, T. Siegrist, L. Venema, H. Eisaki, E. D. Isaacs, and G. A. Sawatzky. Crystallization of charge holes in the spin ladder of $Sr_{14}Cu_{24}O_{41}$. *Nature*, 431:1078–1081, October 2004.

CHAPTER 2

X-RAY SCATTERING: THEORETICAL BACKGROUND

X-ray refers to an electromagnetic wave of short wavelengths (∼Å) and high energies (∼10 KeV). To establish a rigorous quantum mechanical discussion about the interaction between x-ray and the CDW system, we will first review the theory of x-ray scattering by electrons and atoms in both classical electrodynamics and in quantum mechanics. The theory will then be generalized for scattering by solids based on the tight-binding description of formation of the valence bands. As later in this thesis our problem of the CDWs will also be addressed using different methods such as XANES, a correct description on those valence bands is essential to understand resonant x-ray scattering. Using the generalized theory, we show that atoms' properties of x-ray scattering can be profoundly affected by the quantum states emerging in the valence bands. Ultimately the theory will be applied to the problem of x-ray scattering from CDWs.

2.1 X-ray Scattering in Classical Theory

2.1.1 X-ray scattering by free electrons

The fundamental object which scatters an x-ray is an electron. In the classical description of a scattering process, an electron driven by the electric field of x-ray acts like an oscillating dipole and radiates x-rays. For discussion purposes, let us assume the incident field is a plane wave, whose electric field can be written as $\mathbf{E}(\mathbf{r},t) = \mathbf{E}_0 e^{i(\mathbf{q}\cdot\mathbf{r}-\omega t)}$. At the origin, an electron is driven by this field evaluated at $\mathbf{r} = 0$, which we will denote by $\mathbf{E}_{in}(t)$. The situation is illustrated in Figure 2.1.

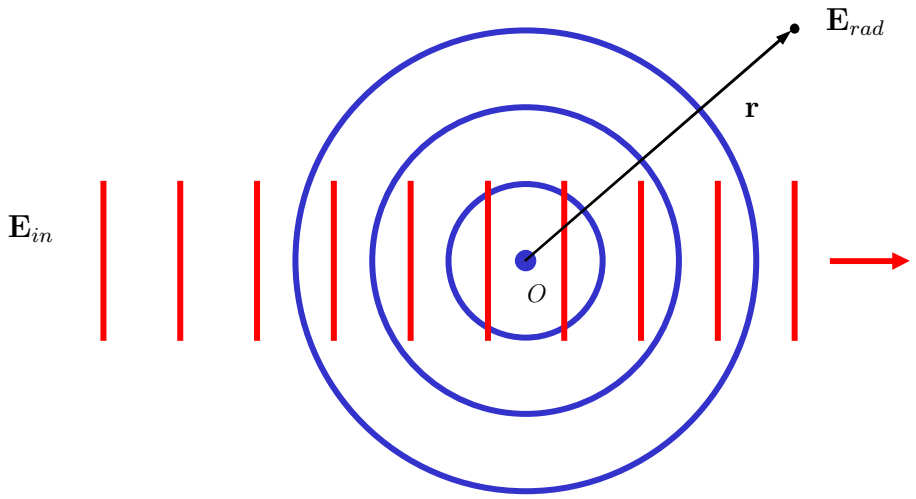

Figure 2.1: X-ray scattering from an electron located at the origin. The incident wave is a plane wave, with the electric field $\mathbf{E}_{in}$ perpendicular to the paper. The scattered field has an electric field $\mathbf{E}_{rad}$, which decays with distance as $|\mathbf{r}|^{-1}$. The red straight lines and the blue circles indicate the wavefronts of the incident wave and of the scattered wave, respectively.

In the radiation field zone [1], the radiated electric field is given by

$$\mathbf{E}_{rad}(\mathbf{r},t) = -\Big(\frac{1}{4\pi\varepsilon_0 c^2}\Big)\frac{1}{r^3}\,\mathbf{r}\times\Big(\mathbf{r}\times\ddot{\mathbf{p}}(t')\Big) \tag{2.1}$$

where $\mathbf{p}(t')$ is the dipole moment evaluated at $t' = t - r/c$. Since the driving force comes from the interaction between the electron and the incident field

$$\ddot{\mathbf{p}}(t') = (-e)\frac{\text{force}}{\text{mass}} = (-e)\frac{-e\mathbf{E}_{in}(t')}{m_e} = \frac{e^2}{m_e}\,\mathbf{E}_0\,e^{-i\omega(t-r/c)}$$

Immediately we find

$$\mathbf{E}_{rad}(\mathbf{r},t) = -\Big(\frac{e^2}{4\pi\varepsilon_0 m_e c^2}\Big)\frac{e^{i\mathbf{q}'\cdot\mathbf{r}}}{r^3}\,\mathbf{r}\times\Big(\mathbf{r}\times\mathbf{E}_{in}(t)\Big) \tag{2.2}$$

where $\mathbf{q}' = (\omega/rc)\mathbf{r}$ is the wavevector of the scattered field pointing toward the observation point $\mathbf{r}$. A vector in the plane of both $\mathbf{r}$ and $\mathbf{E}_{in}$, $\mathbf{E}_{rad}$ is perpendicular to the position vector of the observation point $\mathbf{r}$. By convention the prefactor in Eq (2.2) is often denoted by the symbol r_0. In practical units

$$\boxed{r_0 = \Big(\frac{e^2}{4\pi\varepsilon_0 m_e c^2}\Big) = 2.82\times10^{-5}\text{Å}} \tag{2.3}$$

and is widely known as the classical electron radius.

A useful concept called the *differential cross-section* can then be introduced to help the discussion of the angular dependence of x-ray scattering. Defined as

$$\Big(\frac{d\sigma}{d\Omega}\Big) = \mathbf{r}^2\frac{|\mathbf{E}_{rad}|^2}{|\mathbf{E}_{in}|^2} \tag{2.4}$$

a differential cross-section measures the "transition probability" with which incident x-rays are scattered into a solid angle $d\Omega$. Plugging $\mathbf{E}_{rad}$ and $\mathbf{E}_{in}$ into this definition, we obtain

$$\Big(\frac{d\sigma}{d\Omega}\Big)_e = r_0^2\,(\hat{\mathrm{e}}^{\alpha}\cdot\hat{\mathrm{e}}^{\beta})^2 \tag{2.5}$$

where $\hat{\mathrm{e}}^{\alpha}$ and $\hat{\mathrm{e}}^{\beta}$ are the unit vectors of the polarizations of $\mathbf{E}_{in}$ and of $\mathbf{E}_{rad}$, respectively. Known as the Thomson cross-section of a single electron, Eq (2.5)

corresponds to x-ray scattering that arises as an immediate consequence of electrodynamics. The Thomson cross-section shows an angular dependence which originates in the two independent polarizations. Moreover, x-ray scattering by an electron is independent of frequency.

2.1.2 X-ray scattering by one atom

One can generalize this discussion to x-ray scattering by an atom. We shall do so by adding up the scattering due to individual atomic electrons. Consider an electron with a spatial distribution specified by a number density $\rho_e(\mathbf{r}')$. An incident of x-ray drives the electron, shaking the charges inside a differential volume around the equilibrium position $\mathbf{r}'$. Based on the very same physics that we have discussed for x-ray scattering by free electrons, radiation is created. Looking for an expression which is very similar to Eq (2.2), we write the total radiation as a superposition of the contributions of each volume element in the entire charge distribution

$$\mathbf{E}_{rad}(\mathbf{r},t) = -r_0\Big[\frac{e^{i\mathbf{q}'\cdot\mathbf{r}}}{r^3}\mathbf{r}\times\Big(\mathbf{r}\times\mathbf{E}_{in}(t)\Big)\Big]\int\rho_e(\mathbf{r}')e^{-i\mathbf{Q}\cdot\mathbf{r}'}d\mathbf{r}' \tag{2.6}$$

Inside the integral, $e^{-i\mathbf{Q}\cdot\mathbf{r}'}$ accounts for the relative phase of each differential volume. We have included a discussion of the origin of this factor in Figure 2.2. The newly-defined variable

$$\boxed{\mathbf{Q} = \mathbf{q}' - \mathbf{q}} \tag{2.7}$$

is commonly referred to as the *scattering vector* and is of great importance in discussions of x-ray scattering. We see from Figure 2.2 that $\mathbf{Q}$ defines the geometry in the scattering problem.

As Eq (2.6) suggests, the radiation field is determined by the Fourier transform of the density of the electron cloud. Generalizing this result, let us think of x-

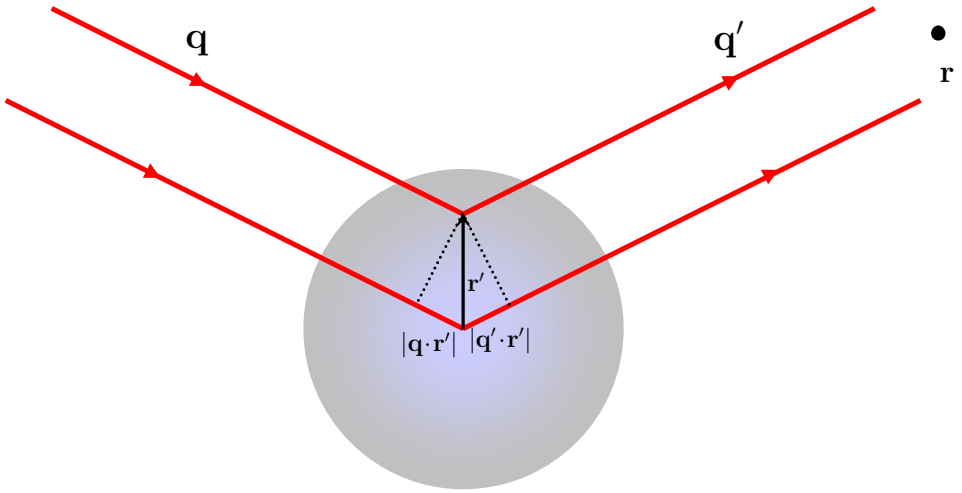

Figure 2.2: Imagine an atom centered at origin. When an incident x-ray (with a wavevector $\mathbf{q}$) hits the atom, the electric field drives the electron cloud, which in turn will radiate. The radiation (scattering) that reaches the observation point at $\mathbf{r}$ is specified by the wavevector $\mathbf{q}' = (\omega/rc)\mathbf{r}$. Corresponding to the different paths, scattering from different positions exhibit a phase difference. Here x-ray traveling in the upper path takes advantage of the shorter path length and hence is *leading* in phase by $-\mathbf{q}\cdot\mathbf{r}' + \mathbf{q}'\cdot\mathbf{r}' = \mathbf{Q}\cdot\mathbf{r}'$. As a differential volume at $\mathbf{r}'$ contains $\rho_e(\mathbf{r}')d\mathbf{r}'$ units of charges, its contribution to the cross-section is $-r_0 \cdot \rho_e(\mathbf{r}')d\mathbf{r}' \cdot e^{-i\mathbf{Q}\cdot\mathbf{r}'}$.

ray scattering by atoms. An atom can be constructed by adding up the density distributions of all its electrons. If $\rho_a(\mathbf{r}')$ stands for the density distribution of all the atomic electrons, we want a Fourier transform

$$f^0(\mathbf{Q}) = \int \rho_a(\mathbf{r}') e^{-i\mathbf{Q}\cdot\mathbf{r}'} d\mathbf{r}' \tag{2.8}$$

The radiation field of x-ray scattering by the atom can then be expressed as

$$\mathbf{E}_{rad}(\mathbf{r}, t) = -r_0 f^0(\mathbf{Q}) \, \frac{e^{i\mathbf{q}'\cdot\mathbf{r}}}{r^3} \, \mathbf{r} \times \Big(\mathbf{r} \times \mathbf{E}_{in}(t) \Big) \tag{2.9}$$

Making use of Eq (2.4) we find the cross-section

$$\Big(\frac{d\sigma}{d\Omega} \Big)_{\text{atom}} = r_0^2 \, |f^0(\mathbf{Q})|^2 \, (\hat{\mathrm{e}}^{\alpha} \cdot \hat{\mathrm{e}}^{\beta})^2 \tag{2.10}$$

Accordingly, the internal structure of an atom is revealed in the cross-section as the square of the Fourier transform of the electronic density. Eq (2.8) is element specific. For this reason $f^0(\mathbf{Q})$ is given a special name called *atomic form factor*. It should be noticed that in the current discussion the atomic form factor is a function of the scattering vector only. It does not depend on x-ray frequency at all.

2.1.3 Dispersion correction to the scattering form factor

The alert reader will immediately notice that Eq (2.9) can not be a complete story of atomic scattering. For example, what about Rayleigh scattering [2]? When passing through the atmosphere, high-frequency electromagnetic waves are subject to more scattering than low-frequency waves. Atomic scattering must depend on frequency. It turns out our assumption that the electron density is static is incorrect. Atoms are excited and relax by absorbing and emitting photons. When

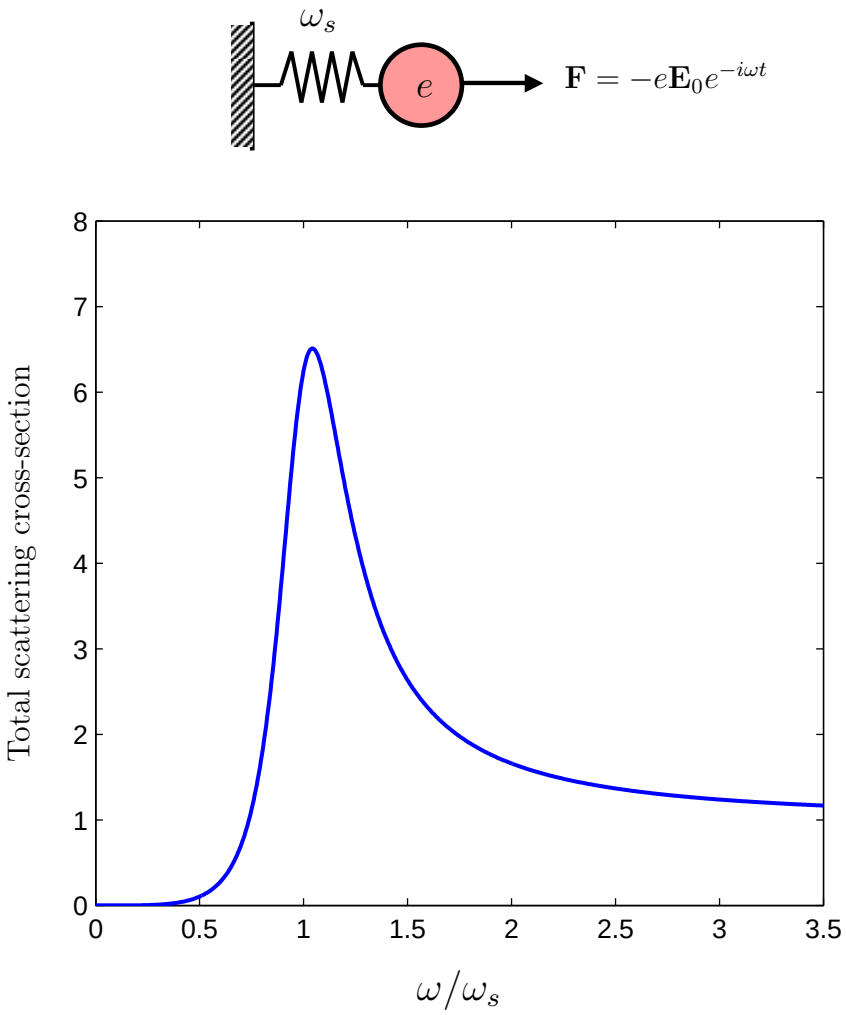

Figure 2.3: In the Lorentz model, an atomic transition is viewed as the oscillation of a charged oscillator with natural frequency ω_s driven by an external field $\mathbf{E}_0 e^{i\omega t}$. For any given polarizations α and β, the cross-section of x-ray scattering is proportional to $r_0^2\omega^4 \cdot [\,(\omega_s^2 - \omega^2)^2 + (\omega\Gamma)^2]^{-1}$. See Eq (2.14). For demonstration purposes, we have made $\Gamma = 0.4\omega_s$.

this happens, the atomic electrons jump between different states, creating an oscillating charge distribution. A classical theory, called Lorentz oscillator mode,l includes such a charge oscillation. This model provides a simple picture of x-ray scattering that is frequency-dependent.

In the Lorentz model [3], an atomic transition is replaced by an oscillating charge as a classical forced oscillator. The electric field of the incoming wave is felt by the electron and acts as the driving force. Radiation is emitted because the charge is accelerated. Such a model is described in Figure 2.3. The equation of motion is

$$\ddot{x} + \Gamma\dot{x} + \omega_s^2 x = -\Big(\frac{e\mathbf{E}_0}{m_e}\Big)e^{-i\omega t} \tag{2.11}$$

We have included the damping term, $\Gamma\dot{x}$, to account for energy dissipation. By substituting a trial solution $x(t) = x_0 e^{-i\omega t}$ into the above, we solve the displacement amplitude

$$x_0 = -\Big(\frac{e\mathbf{E}_0}{m_e}\Big)\frac{1}{(\omega_s^2 - \omega^2 - i\omega\Gamma)}$$

from which the retarded dipole moment can immediately be determined

$$\ddot{\mathbf{p}}(t') = -e\cdot\ddot{x}(t') = \frac{\omega^2}{(\omega_s^2 - \omega^2 - i\omega\Gamma)}\Big(\frac{e^2}{m_e}\Big)\mathbf{E}_0\, e^{-i\omega t'} \tag{2.12}$$

This result then needs to be plugged in Eq (2.1) to evaluate the radiation field

$$\mathbf{E}_{rad}(\mathbf{r},t) = -r_0\Big(\frac{\omega^2}{\omega_s^2 - \omega^2 - i\omega\Gamma}\Big)\ \frac{e^{i\mathbf{q}'\cdot\mathbf{r}}}{r^3}\,\mathbf{r}\times\Big(\mathbf{r}\times\mathbf{E}_{in}(t)\Big) \tag{2.13}$$

Thus the cross-section is

$$\Big(\frac{d\sigma}{d\Omega}\Big)_e = r_0^2\frac{\omega^4}{(\omega_s^2-\omega^2)^2 + (\omega\Gamma)^2}\ (\hat{\mathrm{e}}^\alpha\cdot\hat{\mathrm{e}}^\beta)^2 \tag{2.14}$$

In Figure 2.3 we plot this cross-section as a function of frequency, assuming $\Gamma = 0.4\omega_s$. The Lorentz model gives a cross-section that depends on frequency.

The advantage of using the classical model is we can interpret the frequency

behavior of Eq (2.14) based the motion of the charge. Look at the cross-section in Figure 2.3. In the high frequency region $\omega > \omega_s$, the function is a monotonically decreasing function and will become Eq (2.5) at infinite frequency. In this limit, the oscillation corresponds to finite accelerations and small displacements. The effect is the charge is shaken to produce radiation like a free electron. With regards of x-ray scattering, this high frequency behavior is characterized by Thomson scattering.

At frequencies much less than the natural frequency ($\omega \ll \omega_s$), the cross-section is really small. Nevertheless it grows as ω^4, consistent with the famous Rayleigh scattering one would observe for visible light. Here, in contrast to the high frequency region, scattering is attributed to the bound electrons. The oscillation is characterized by small displacements and small accelerations.

Despite its simpleness, the Lorentz model does succeed in describing what we have known and learned about scattering at high frequencies (Thomson scattering) and at low frequencies (Rayleigh scattering). As we can clearly see in Figure 2.3, there is still more in the Lorentz model. Around the natural frequency ω_s, the cross-section becomes large: The charged oscillator produces more scattering than Thomson scattering. According to Eq (2.14), the peak has a width determined by Γ and a height by $(\Gamma/\omega_s)^{-2}$. Provided Γ is really small compared to ω_s, an immense cross-section is expected at $\omega = \omega_s$. In terms of how radiation is created, the big cross-section corresponds to to the large acceleration of the oscillator in resonance with x-ray. We shall refer to such enhanced scattering at $\omega \approx \omega_s$ as *resonant x-ray scattering.*

Due to this discussion of the Lorentz model, Eq (2.10) needs to be considered as the high frequency limit of the cross-section of x-ray scattering, whereas at lower frequencies scattering can become suppressed as in Rayleigh scattering as well as

become enhanced as in resonant x-ray scattering. To account for the frequency dependence, we generalize the concept of the atomic form factor by adding a *dispersion correction* to the previously-defined $f^0(\mathbf{Q})$. We denote the generalization by $f(\mathbf{Q},\omega)$. We will need to consider the two polarizations:

$$\left(\frac{d\sigma}{d\Omega}\right)_{\text{atom},\alpha\beta} \equiv \mathbf{r}^2 \frac{|\mathbf{E}_{rad}\text{; with polarization } \beta|^2}{|\mathbf{E}_{in}\text{; with polarization } \alpha|^2} = r_0^2 |f_{\alpha\beta}(\mathbf{Q},\omega)|^2 \tag{2.15}$$

The subscripts of $f_{\alpha\beta}(\mathbf{Q},\omega)$ mean the atomic form factor is polarization specific. Collecting these results together we write the atomic form factor as

$$f_{\alpha\beta}(\mathbf{Q},\omega) = f^0_{\alpha\beta}(\mathbf{Q}) + f'_{\alpha\beta}(\omega) + i f''_{\alpha\beta}(\omega) \tag{2.16}$$

In this expression, $f^0_{\alpha\beta}$ is the Thomson scattering component, which is inherited directly from Eq (2.8) as

$$f^0_{\alpha\beta}(\mathbf{Q}) = (\hat{\mathrm{e}}^{\alpha} \cdot \hat{\mathrm{e}}^{\beta}) \int \rho_a(\mathbf{r}') e^{-i\mathbf{Q}\cdot\mathbf{r}'} d\mathbf{r}' \tag{2.17}$$

And $(f'_{\alpha\beta} + i f''_{\alpha\beta})$ is the dispersion correction which we have mentioned earlier[1].

Although one can determine the values of $(f' + if")$ based on classical methods [3], the precise meaning of the dispersion correction can only be seen in quantum mechanics. Quantitatively speaking, f' exists as a negative number such that it will cancel f^0 at low frequencies. The absolute value of f' decreases in steps until it eventually approaches zero at very high frequencies. By analogy with the classical forced oscillator of the Lorentz model, f'' appears as a result of finite energy dissipation. It is worth mentioning that causality is preserved through a special relation between f' and f''.

[1]Rigorously speaking, the dispersion correction is a function of $\mathbf{q}$ and $\mathbf{q}'$ as well as of frequency. As will be shown in the next section, in the dipole approximation, the dispersion correction is a function of frequency only.

2.2 X-ray Scattering in Quantum Mechanics

First let us specify the quantum states. Assuming there is a low lying state $|\,s\rangle$ which is occupied by an electron with energy E_s. By absorbing x-ray, the electron can be excited to *unoccupied* states $|\,n\rangle$ with higher energy E_n. The corresponding transition is characterized by a frequency $(E_n - E_s)/\hbar = \omega_{ns}$. The energy uncertainty gives the transtion a finite energy width, which can be associated with the core-hole lifetime Γ. As for x-ray, we can begin to think of it as photons. The energy of x-ray is therefore equal to $\hbar\omega$.

2.2.1 Cross-section of x-ray scattering by electrons

The quantum theory of x-ray scattering is reviewed in Appendix A. As shown in Eq (A.14), the electron corresponds to a cross-section of x-ray scattering ($\mathbf{p}$ is the momentum operator of the electron, $\hat{\mathrm{e}}^\alpha$ is the polarization of incident x-ray, and $\mathbf{p}^\alpha = \mathbf{p}\cdot\hat{\mathrm{e}}^\alpha$ is the projected momentum operator)

$$\Big(\frac{d\sigma}{d\Omega}\Big)_{e,\alpha\beta} = r_0^2 \Big|(\hat{\mathrm{e}}^\alpha\cdot\hat{\mathrm{e}}^\beta)\langle\, s|\, e^{-i\mathbf{Q}\cdot\mathbf{r}_s}|\, s\rangle + \frac{1}{m_e}\sum_n\Big(\frac{\langle\, s|O^{\beta\dagger}(\mathbf{q}')|\, n\rangle\langle\, n|O^\alpha(\mathbf{q})|\, s\rangle}{\hbar(\omega-\omega_{ns})+i\frac{\Gamma}{2}} - \frac{\langle\, s|O^\alpha(\mathbf{q})|\, n\rangle\langle\, n|O^{\beta\dagger}(\mathbf{q}')|\, s\rangle}{\hbar(\omega+\omega_{ns})}\Big)\Big|^2 \quad (2.18)$$

where $O^\alpha(\mathbf{q}) = \mathbf{p}_s^\alpha\, e^{i\mathbf{q}\cdot\mathbf{r}_s}$. Inside the large parenthesis, we collect the last two terms as they both have ω in the denominators. We expect that together these two terms will determine the frequency behavior of the cross-section. Look at their numerators, which are the products of matrix elements between $|\,s\rangle$ and $|\,n\rangle$. In the language of quantum mechanics, these products represent successive transitions from $|\,s\rangle$ to $|\,n\rangle$ and back to $|\,s\rangle$. See the picture given in Figure 2.4. Accordingly, we will refer to $|\,s\rangle$ as the initial state and $|\,n\rangle$ as the intermediate state. Note that

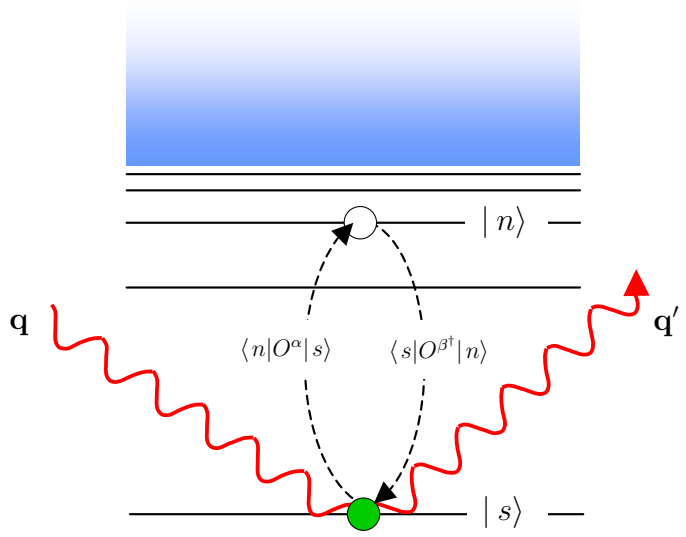

Figure 2.4: With the electron appearing in the state $|\,s\rangle$, resonant x-ray scattering occurs via an intermediate electronic state $|\,n\rangle$. The virtual transition is characterized by the two matrix elements $\langle\, n|O^{\alpha}|\,s\rangle$ (for excitation) and $\langle\, s|O^{\beta\dagger}|\,n\rangle$ (for de-excitation). During this process, an incoming photon (with a wavevector $\mathbf{q}$) is annihilated and an outgoing photon (with a wavevector $\mathbf{q}'$) is created.

the summation runs over all unoccupied $|\,n\rangle$'s.

As a first application of the quantum mechanical theory we shall reconsider the frequency behavior of the cross-section of x-ray scattering predicted by the Lorentz model. Provided that $\mathbf{Q}\cdot\mathbf{r}_s \ll 1$, we can replace the exponent using the *dipole approximation*: $e^{i\mathbf{Q}\cdot\mathbf{r}_s} \approx 1$. Similarly, $O^{\alpha}(\mathbf{q}) \approx \mathbf{p}_s^{\alpha}$ and $O^{\beta\dagger}(\mathbf{q}') \approx \mathbf{p}_s^{\beta\dagger} = \mathbf{p}_s^{\beta}$. The cross-section can then be approximated as

$$\Big(\frac{d\sigma}{d\Omega}\Big)_{e,\alpha\beta}^{d.a.} = r_0^2\,\Big|(\hat{\mathrm{e}}^{\alpha}\cdot\hat{\mathrm{e}}^{\beta}) + \frac{1}{m_e}\sum_n\Big(\frac{\langle\, s|\mathbf{p}_s^{\beta}|\, n\rangle\langle\, n|\mathbf{p}_s^{\alpha}|\, s\rangle}{\hbar(\omega-\omega_{ns})+i\frac{\Gamma}{2}} - \frac{\langle\, s|\mathbf{p}_s^{\alpha}|\, n\rangle\langle\, n|\mathbf{p}_s^{\beta}|\, s\rangle}{\hbar(\omega+\omega_{ns})}\Big)\Big|^2 \tag{2.19}$$

where we have used the fact that $\langle s|\, s\,\rangle = 1$.[2] Immediately we recognize that the $(\hat{\mathrm{e}}^{\alpha}\cdot\hat{\mathrm{e}}^{\beta})$ term represents the contribution of Thomson scattering, as at very high frequencies both the frequency dependent terms are ignorable, and we will recover Eq (2.5). Thomson scattering is indeed the high frequency limit of the Lorentz model.

To see how Rayleigh scattering and resonant x-ray scattering appear at lower frequencies, we want to combine the three different terms in Eq (2.19). One can expand $(\hat{\mathrm{e}}^{\alpha}\cdot\hat{\mathrm{e}}^{\beta})$ as a summation over the intermediate states

$$\begin{aligned}\hat{\mathrm{e}}^{\alpha}\cdot\hat{\mathrm{e}}^{\beta} &= \frac{1}{i\hbar}\sum_n[\langle\, s|\mathbf{x}_s\cdot\hat{\mathrm{e}}^{\alpha}|\, n\rangle\langle\, n|\mathbf{p}_s\cdot\hat{\mathrm{e}}^{\beta}|\, s\rangle - \langle\, s|\mathbf{p}_s\cdot\hat{\mathrm{e}}^{\alpha}|\, n\rangle\langle\, n|\mathbf{x}_s\cdot\hat{\mathrm{e}}^{\beta}|\, s\rangle] \\ &= \frac{1}{m_e\hbar}\sum_n\frac{1}{\omega_{ns}}[\langle\, s|\mathbf{p}_s^{\alpha}|\, n\rangle\langle\, n|\mathbf{p}_s^{\beta}|\, s\rangle + \langle\, s|\mathbf{p}_s^{\beta}|\, n\rangle\langle\, n|\mathbf{p}_s^{\alpha}|\, s\rangle]\end{aligned} \tag{2.20}$$

[2] A formula similar to Eq (2.19) was first obtained by H. A. Kramers and W. Heisenberg using the correspondence principle in 1925; hence it is called the Kramers-Heisenberg formula [1]. Although in the general Kramers-Heisenberg formula the electron can enter a different final state than $|s\rangle$, here our discussion concerns the special case of elastic scattering.

based on the commutator $[\mathbf{x},\mathbf{p}] = i\hbar$ and its direct consequence[3] that $\langle\, s|\mathbf{p}|\, n\rangle = im\omega_{ns}\langle\, s|\mathbf{x}|\, n\rangle$. It follows that

$$(\hat{\mathrm{e}}^{\alpha}\cdot\hat{\mathrm{e}}^{\beta}) + \frac{1}{m_e}\sum_n\Big(\frac{\langle\, s|\mathbf{p}_s^{\beta}|\, n\rangle\langle\, n|\mathbf{p}_s^{\alpha}|\, s\rangle}{\hbar(\omega-\omega_{ns})+i\frac{\Gamma}{2}} - \frac{\langle\, s|\mathbf{p}_s^{\alpha}|\, n\rangle\langle\, n|\mathbf{p}_s^{\beta}|\, s\rangle}{\hbar(\omega+\omega_{ns})}\Big)$$
$$\approx \frac{1}{m_e\hbar}\sum_n\frac{\omega}{\omega_{ns}}\Big(\frac{\langle\, s|\mathbf{p}_s^{\beta}|\, n\rangle\langle\, n|\mathbf{p}_s^{\alpha}|\, s\rangle}{(\omega-\omega_{ns})+i\frac{\Gamma}{2\hbar}} + \frac{\langle\, s|\mathbf{p}_s^{\alpha}|\, n\rangle\langle\, n|\mathbf{p}_s^{\beta}|\, s\rangle}{(\omega+\omega_{ns})}\Big) \qquad (2.21)$$

In order to get the final result, we have assumed that Γ is a very small energy width. Such an expression can then be used in Eq (2.19) to evaluate the cross-section. After some straightforward algebra[4] we find

$$\Big(\frac{d\sigma}{d\Omega}\Big)^{d.a.}_{e,\alpha\beta} = (\frac{r_0}{m_e\hbar})^2\Big|\sum_n\frac{(\,\omega/\omega_{ns})}{\omega^2-\omega_{ns}^2+i\frac{\omega\Gamma}{\hbar}}\,\big[\omega\big(\langle s|\mathbf{p}_s^{\beta}|n\rangle\langle n|\mathbf{p}_s^{\alpha}|s\rangle + \langle s|\mathbf{p}_s^{\alpha}|n\rangle\langle n|\mathbf{p}_s^{\beta}|s\rangle\big)$$
$$+\omega_{ns}\big(\langle s|\mathbf{p}_s^{\beta}|n\rangle\langle n|\mathbf{p}_s^{\alpha}|s\rangle - \langle s|\mathbf{p}_s^{\alpha}|n\rangle\langle n|\mathbf{p}_s^{\beta}|s\rangle\big)\big]\,\Big|^2 \qquad (2.22)$$

with which the overall frequency dependence of the cross-section can be better appreciated. We notice that the denominator is strikingly similar to the Lorentz model, Eq (2.14).

We would like to demonstrate that the cross-section can easily be determined at low frequencies as well as at resonance. When $\omega\to 0$, $(\omega^2-\omega_{ns}^2+i\frac{\omega\Gamma}{\hbar})^{-1}\approx\omega_{ns}^{-2}$. Using the commutation relation $[\mathbf{x}\cdot\hat{\mathrm{e}}^{\alpha},\mathbf{x}\cdot\hat{\mathrm{e}}^{\beta}]=0$ we obtain the following identity[5]

$$\sum_n\frac{1}{\omega_{ns}^2}\big(\langle s|\mathbf{p}_s^{\beta}|n\rangle\langle n|\mathbf{p}_s^{\alpha}|s\rangle - \langle s|\mathbf{p}_s^{\alpha}|n\rangle\langle n|\mathbf{p}_s^{\beta}|s\rangle\big) = 0 \qquad (2.23)$$

and use it to simplify Eq (2.22), The cross-section thus reduces to the simple form

$$\Big(\frac{d\sigma}{d\Omega}\Big)^{d.a.}_{e,\alpha\beta;\,\omega\to 0} = (\frac{r_0}{m_e\hbar})^2\omega^4\Big|\sum_n\frac{1}{\omega_{ns}^3}\big(\langle s|\mathbf{p}_s^{\beta}|n\rangle\langle n|\mathbf{p}_s^{\alpha}|s\rangle + \langle s|\mathbf{p}_s^{\alpha}|n\rangle\langle n|\mathbf{p}_s^{\beta}|s\rangle\big)\Big|^2 \qquad (2.24)$$

which indeed shows the frequency dependence of Rayleigh scattering. By resonance we mean that the frequency of the x-ray equals the frequency of a particular

[3]The relation holds because $\langle\, s|\mathbf{p}|\, n\rangle = \langle\, s|\frac{im_e}{\hbar}[\mathcal{H},\mathbf{x}]|\, n\rangle = -\frac{im_e(E_n-E_s)}{\hbar}\langle\, s|\mathbf{x}|\, n\rangle$.
[4]The calculation is very similar to that between the two equations (A7) and (A8) in Ref. [2].
[5]See (2.166) in Ref. [1] for the proof.

transition ω_{ns}. Assuming that Γ is small compared to the energy difference between the intermediate states, we determine that the transition between $|\, s\rangle$ and $|\, n\rangle$ dominates the summation. The cross-section can then be written as

$$\Big(\frac{d\sigma}{d\Omega}\Big)^{d.d}_{e,\alpha\beta;\,\omega=\omega_{ns}} \approx (\frac{r_0}{m_e\Gamma})^2 |\langle s|\mathbf{p}_s^\beta|n\rangle\langle n|\mathbf{p}_s^\alpha|s\rangle|^2 \tag{2.25}$$

The smallness of Γ suggests that the cross-section becomes significantly enhanced, corresponding to the physical situation of resonant x-ray scattering.

2.2.2 Cross-section of x-ray scattering by atoms

We continue our discussion by considering x-ray scattering from atoms and solids. Assume we have an atom in a well-defined state, with each of the atomic electrons being accommodated in an eigenstate $|s\rangle$. When x-rays are scattered, the cross-section has contributions from all the electrons. Correspondingly we require an additional summation over all the occupied states

$$\begin{aligned}\Big(\frac{d\sigma}{d\Omega}\Big)_{\text{atom},\alpha\beta} = r_0^2 \Big|(\hat{\mathrm{e}}^\alpha\cdot\hat{\mathrm{e}}^\beta)\sum_s \langle\, s|\, e^{-i\mathbf{Q}\cdot\mathbf{r}_s}|\, s\rangle \\ +\frac{1}{m_e}\sum_{s,n}\Big(\frac{\langle\, s|O^{\beta^\dagger}(\mathbf{q}')|\, n\rangle\langle\, n|O^\alpha(\mathbf{q})|\, s\rangle}{\hbar(\omega-\omega_{ns})+i\frac{\Gamma}{2}} - \frac{\langle\, s|O^\alpha(\mathbf{q})|\, n\rangle\langle\, n|O^{\beta^\dagger}(\mathbf{q}')|\, s\rangle}{\hbar(\omega+\omega_{ns})}\Big)\Big|^2\end{aligned} \tag{2.26}$$

From the Lorentz model we have learned that different scattering behaviors take place depending on the x-ray frequency with respect to the transition frequencies. Here we have multiple values of ω_{ns} associated with the different states $|s\rangle$. When x-ray scattering is coming from atoms, it is usually a mixture of Thomson scattering, Rayleigh scattering, and possibly resonant scattering.

In Eq (2.26) we write the cross-section such that the three different terms individually correspond to distinct x-ray scattering processes in the quantum field theory. As we have discussed in the previous section, we want to use the atomic

form factor in describing x-ray scattering by atoms. Since

$$\sum_s \langle s|\, e^{-i\mathbf{Q}\cdot\mathbf{r}_s}\,|s\rangle = \int \sum_s \langle s|s\rangle\, e^{-i\mathbf{Q}\cdot\mathbf{r}'} d\mathbf{r}' = \int \rho_a(\mathbf{r}') e^{-i\mathbf{Q}\cdot\mathbf{r}'} d\mathbf{r}' \tag{2.27}$$

inside the square of Eq (2.26) the corresponding term is just our $f^0_{\alpha\beta}$ defined in Eq (2.17). Meanwhile, the remaining terms are frequency dependent, and we recognize that these terms are the origin of the dispersion correction. If we use the dipole approximation described in the paragraph before Eq (2.19), on only these two terms, the dispersion correction is a complex function of frequency only. By separating the real part and the imaginary part,

$$f'_{\alpha\beta}(\omega) = \frac{1}{m_e}\sum_{s,n} \mathrm{Re}\Big[\frac{\langle s|\mathbf{p}^\beta_s|n\rangle\langle n|\mathbf{p}^\alpha_s|s\rangle}{\hbar(\omega-\omega_{ns})+i\frac{\Gamma}{2}} - \frac{\langle s|\mathbf{p}^\alpha_s|n\rangle\langle n|\mathbf{p}^\beta_s|s\rangle}{\hbar(\omega+\omega_{ns})}\Big] \tag{2.28}$$

$$f''_{\alpha\beta}(\omega) = \frac{1}{m_e}\sum_{s,n} \mathrm{Im}\Big[\frac{\langle s|\mathbf{p}^\beta_s|n\rangle\langle n|\mathbf{p}^\alpha_s|s\rangle}{\hbar(\omega-\omega_{ns})+i\frac{\Gamma}{2}} - \frac{\langle s|\mathbf{p}^\alpha_s|n\rangle\langle n|\mathbf{p}^\beta_s|s\rangle}{\hbar(\omega+\omega_{ns})}\Big] \tag{2.29}$$

Through these definitions we give our interpretation of the three different components in Eq (2.26) for the atomic form factor. It is worth emphasizing that the dipole approximation is the key to get those results in the last two equations. Otherwise the dispersion correction will also shows dependence on the wavevectors $\mathbf{q}$ and $\mathbf{q}'$.[6] Thus, if quadrupole scattering becomes important, the attempt to separate the energy-dependence from the $\mathbf{Q}$-dependence in the atomic form factor shown in Eq (2.16) will fail. In this aspect, we have a general comment on the dipole approximation. See Appendix A.

[6]The fact that we approximate the last two terms in Eq (2.26) using $f'(\omega)$ and $f''(\omega)$ means we would ignore the spatial variation of the dispersion correction. As a consequence, Eq (2.16) is a better approximation of the atomic scattering form factor at small $\mathbf{Q}$ than at big $\mathbf{Q}$. In practice one can ignore the error if the initial states are well-confined states.

2.2.3 On the way to x-ray scattering by solids

When atoms are put into a crystal lattice, the electronic structure changes. Continuous bands are developed to accommodate the valence electrons. Other electrons, being deeply buried inside the atoms, remain unaffected and retain their atomic characteristics. Accordingly there are two types of states; electrons are either in *valence-band* states or in *core-level* states. X-ray scattering occurs via transitions between the various states. Should any change happen inside the sample regarding the characteristics of those electronic states, we would expect there might be corresponding effects in x-ray scattering. For advanced treatments, our references serve as a valuable source of background knowledge in terms of the formalism as well as various issues addressed in related problems [2, 7, 8].

It is not a difficult task to extend our theory to solids. Given the expression of the cross-section as Eq (2.26), we now understand the states as states of the entire solid. As $|s\rangle$ denote the occupied states, they are associated with the localized core-level states. The intermediate states $|n\rangle$ appearing in the dispersive terms are the unoccupied states. In the solid these will be the states with energies higher than the Fermi energy existing in the valence bands and in the continuum. As for the operators such as $O^{\alpha}(\mathbf{q})$, they come with the momentum $\mathbf{p}_s$ of the electron found it $|s\rangle$. Yet $O^{\alpha}(\mathbf{q})$ contains a factor $e^{i\mathbf{q}\cdot\mathbf{r}_s}$, which results in a phase difference between the operators. When it comes to determine the properties of scattered x-ray, one should make sure that such a phase shift is properly included.

More can be said about the intermediate states. Showing up in the valence bands, $|n\rangle$ correspond to extended (or localized) states characterized by the continuous momentum $\mathbf{k}$. To emphasize this nature, we will denote the states as $|\,n_{\mathbf{k}}\rangle$.

Finally the following expression

$$\Big(\frac{d\sigma}{d\Omega}\Big)_{\alpha\beta} = r_0^2 \Big| (\hat{\mathrm{e}}^{\alpha}\cdot\hat{\mathrm{e}}^{\beta}) \sum_s \langle s|\, e^{-i\mathbf{Q}\cdot\mathbf{r}_s}\,|s\rangle + \frac{1}{m_e}\sum_{s,\mathbf{k}} \Big(\frac{\langle s|O^{\beta\dagger}(\mathbf{q}')|n_{\mathbf{k}}\rangle\langle n_{\mathbf{k}}|O^{\alpha}(\mathbf{q})|s\rangle}{\hbar(\omega-\omega_{\mathbf{k}s})+i\frac{\Gamma}{2}} - \frac{\langle s|O^{\alpha}(\mathbf{q})|n_{\mathbf{k}}\rangle\langle n_{\mathbf{k}}|O^{\beta\dagger}(\mathbf{q}')|s\rangle}{\hbar(\omega+\omega_{\mathbf{k}s})} \Big) \Big|^2 \quad (2.30)$$

emerges. Note for the dispersive correction the summation of the intermediate states is now performed with respect to $\mathbf{k}$. Eq (2.30) summarizes our remarks about x-ray scattering by solids.

Until one can further specify the quantum states of $|\,n_{\mathbf{k}}\rangle$, Eq (2.30) stands as a general formula of the cross-section. Yet we feel this is a perfect timing to advertise our strategy in carrying out the summation over the initial states $|s\rangle$. By taking advantage of the solid's lattice structure[7], we write the position (with $\mathbf{R}$ standing for the lattice points)

$$\mathbf{r}_s = \mathbf{R} + \mathbf{r}'_s \quad (2.31)$$

which in turn also suggests that we consider the summation according to the lattice index

$$\sum_s = \sum_{\mathbf{R}} \sum_{s(\mathbf{R})} \quad (2.32)$$

Here $s(\mathbf{R})$ means the the core-level states of the atom located at $\mathbf{R}$. In this manner we determine Thomson scattering as follows

$$\sum_s \langle s|\, e^{-i\mathbf{Q}\cdot\mathbf{r}_s}|s\rangle = \sum_{\mathbf{R}} e^{-i\mathbf{Q}\cdot\mathbf{R}} \sum_{s(\mathbf{R})} \langle s|\, e^{-i\mathbf{Q}\cdot\mathbf{r}'_s}|s\rangle = f^0(\mathbf{Q}) \sum_{\mathbf{R}} e^{-i\mathbf{Q}\cdot\mathbf{R}} \quad (2.33)$$

where we have made use of both Eq (2.8) and (2.27). In the final expression of Eq (2.33), we have naturally move $f^0(\mathbf{Q})$ out of the summation for it represents the universal atomic from factor. Written in this particular format, Eq (2.33) is known as the *lattice sum*. For the dispersive terms we first notice that

$$\langle s|O^{\alpha}(\mathbf{q})|n_{\mathbf{k}}\rangle = \langle s|\mathbf{p}_s^{\alpha}\, e^{i\mathbf{q}\cdot(\mathbf{R}+\mathbf{r}'_s)}|n_{\mathbf{k}}\rangle \approx e^{i\mathbf{q}\cdot\mathbf{R}}\langle s|\mathbf{p}_s^{\alpha}|n_{\mathbf{k}}\rangle \quad (2.34)$$

[7]We assume that the lattice contains one and only one atom of the same kind in each unit cell.

Once again we have assumed the dipole approximation $e^{i\mathbf{q}\cdot\mathbf{r}'_s} \approx 1$ in order to get the final expression. It follows immediately that

$$\frac{1}{m_e}\sum_{s,\mathbf{k}}\Big(\frac{\langle s|O^{\beta\dagger}(\mathbf{q}')|n_\mathbf{k}\rangle\langle n_\mathbf{k}|O^{\alpha}(\mathbf{q})|s\rangle}{\hbar(\omega-\omega_{ns})+i\frac{\Gamma}{2}}-\frac{\langle s|O^{\alpha}(\mathbf{q})|n_\mathbf{k}\rangle\langle n_\mathbf{k}|O^{\beta\dagger}(\mathbf{q}')|s\rangle}{\hbar(\omega+\omega_{ns})}\Big)$$
$$=\sum_{\mathbf{R}}e^{-i\mathbf{Q}\cdot\mathbf{R}}\sum_{s(\mathbf{R}),\mathbf{k}}\frac{1}{m_e}\Big[\frac{\langle s|\mathbf{p}_s^{\beta}|n_\mathbf{k}\rangle\langle n_\mathbf{k}|\mathbf{p}_s^{\alpha}|s\rangle}{\hbar(\omega-\omega_{\mathbf{k}s})+i\frac{\Gamma}{2}}-\frac{\langle s|\mathbf{p}_s^{\alpha}|n_\mathbf{k}\rangle\langle n_\mathbf{k}|\mathbf{p}_s^{\beta}|s\rangle}{\hbar(\omega+\omega_{\mathbf{k}s})}\Big] \quad (2.35)$$

In contrast to the case of Thomson scattering, this result does not necessarily correspond to a simple lattice sum. Nevertheless it takes the familiar form as a sum of some *localized* functions with their phases properly determined in accordance with the lattice positions. With this aspect we have demonstrated that x-ray scattering happens on an atomic basis, regardless of the condition that it is now all in the solid.

2.3 Band States in Tight-Binding Description

As described in Eq (2.35) we need to know the band states in order to determine x-ray scattering. Here we provide a brief introduction to band construction based on the description of the tight-binding theory.

In the tight-binding theory band formation is attributed to the overlap of atomic wave functions. For this reason the theory is most useful for describing the energy band that arise from the partially filled *d*-shells of transition metal atoms and for describing the electronic structure of insulators [9]. Let $\psi_\mathbf{k}(\mathbf{r})$ be the wave function of $|n_\mathbf{k}\rangle$ with momentum $\mathbf{k}$. The Bloch theorem requires the state take the following form

$$\psi_\mathbf{k}(\mathbf{r})=\frac{1}{\sqrt{N}}\sum_{\mathbf{R}}e^{i\mathbf{k}\cdot\mathbf{R}}\varphi_\mathbf{k}(\mathbf{r}-\mathbf{R}) \quad (2.36)$$

assuming a monoatomic lattice with N sites. In this expression, $\mathbf{k}$ ranges through the N values in the first Brillouin zone consistent with the Born-von Karman periodic boundary condition, and $\varphi_{\mathbf{k}}(\mathbf{r})$ is a localized function. For each $\mathbf{k}$, the tight-binding method solves the crystal Schrödinger equation using the atomic orbitals as the basis functions:

$$\varphi_{\mathbf{k}}(\mathbf{r}) = \sum_t b_{\mathbf{k},t}\, \phi_t(\mathbf{r}) \tag{2.37}$$

In the associated eigenvalue problem, simultaneously, the energy will be specified. Being momentum-dependent, the energy becomes a dispersive quantity, which is commonly referred to as the band structure $E(\mathbf{k})$.

In most cases, the summation in Eq (2.37) involves a relatively small number of atomic orbitals. Very often we find that each band is associated with a specific atomic orbital. In these situations, we can approximate the wave function by

$$\psi_{\mathbf{k}}(\mathbf{r}) = \frac{1}{\sqrt{N}} \sum_{\mathbf{R}} e^{i\mathbf{k}\cdot\mathbf{R}} \phi^*(\mathbf{r} - \mathbf{R}) \tag{2.38}$$

with $\phi^*(\mathbf{r})$ being the dominating component. In the level of this approximation, the momentum matters because of the phase $e^{i\mathbf{k}\cdot\mathbf{R}}$. Indeed, a wave function like this corresponds to a relatively simple state, in which the electron can be found with equal probability in any lattice site.

In the following chapters we will construct the wave function for the CDW state based on the result of Eq (2.38). It will be shown that the CDW state gives more structure in the dispersive terms than the usual valence-band state does.

BIBLIOGRAPHY

[1] J. R. Reitz, F. J. Milford, and R. E. Christy. *Foundations of Electromagnetic Theory*. Addison-Wesley Publishing Company, MA, 1992. Reading.

[2] Alan Giambattista, Betty McCarthy Richardson, and Robert C. Richardson. *Foundations of Electromagnetic Theory*. McGraw-Hill Higher Education, Boston,MA, 2004. Reading.

[3] Peter W. Milloni and Joseph H. Eberly. *Lasers*. John Wiley and Sons Ltd, New York, 1988. pages 27–33.

[4] Jens Als-Nielsen and Des McMorrow. *Elements of modern X-ray physics*. John Wiley and Sons Ltd, New York, 2001. Chapter 7.

[5] J. J. Sakurai. *Advanced quantum mechanics*. Addison-Wesley Publishing Company, MA, 1967. Chapter 2.

[6] M. Blume. *Resonant Anomalous X-ray Scattering: Theory and Applications*, pages 495–512. North-Holland, 1994.

[7] J. P. Hannon, G. T. Trammell, M. Blume, and Doon Gibbs. X-ray resonance exchange scattering. *Phys. Rev. Lett.*, 61(10):1245–1248, Sep 1988.

[8] I. S. Elfimov, N. A. Skorikov, V. I. Anisimov, and G. A. Sawatzky. Band structure approach to resonant x-ray scattering. *Phys. Rev. Lett.*, 88(1):015504, Dec 2001.

[9] Neil W. Ashcroft and N. David Mermin. *Solid State Physics*. Harcourt, Inc., FL, 1976. Chapter 10.

CHAPTER 3

CHARGE DENSITY WAVE OF TANTALUM DISULFIDE

In this chapter we will discuss the Peierls theory of CDWs. Instead of the phenomenological model, we will look deep into the formal theory itself. Canonical treatments such as quasiparticle formation and Bogoliubov transformation will be invoked so the physics of CDWs can be best appreciated. Significantly, the theory enables us to determine important properties such as the size of the energy gap and the amplitude of the CMW. Most importantly, we will write down the general wave functions for the electronic states of CDWs. We will see that the precise meaning of the phenomenological descriptions can all be found in this theoretical study. The CDW of $1T$-TaS_2 will then be introduced using these concepts, in line with some research perspectives on this specific CDW as an interesting correlated-electron system. Combining with the next chapter, this discussion illustrates the importance of the band structure for understanding resonant x-ray scattering.

3.1 CDW Phenomenology

As we have described in the introductory chapter, the LDW is essentially a lattice displacement

$$\Delta u_{\mathbf{R}} = u_0 \sin(\, \mathbf{k}_{\mathrm{CDW}} \cdot \mathbf{R} \,) \tag{3.1}$$

which is superimposed on the original lattice to create an extra periodicity. The superstructure creates strong back scattering at $\mathbf{k}_{\mathrm{CDW}}$ inside the Brillouin zone. And just like what happens at the zone boundary, the conduction-band state becomes a superposition of the direct wave function and the back scattering

$$\mid n_{\mathbf{k}}^{\mathrm{CDW}} \rangle = U_{\mathbf{k}} \mid n_{\mathbf{k}} \rangle + V_{\mathbf{k}} \mid n_{\mathbf{k}'} \rangle \tag{3.2}$$

where $\mathbf{k}'$ is used to denote the momentum of the back scattering, namely

$$\mathbf{k}' = \mathbf{k} + \mathbf{k}_{\text{CDW}} \tag{3.3}$$

Scattering like this is possible only if the electron is scattered into an unoccupied state. Therefore $\mathbf{k}$ and $\mathbf{k}'$ are wavevectors near the Fermi surface. The geometry of these vectors are shown in Figure 3.1. Additionally, we must have

$$U_{\mathbf{k}}^2 + V_{\mathbf{k}}^2 = 1 \tag{3.4}$$

as required by the normalization condition.

We will demonstrate that Eq (3.2) is the quantum state that describing the CMW. Let us first look at the charge distribution. Using the tight-binding wave function found in Eq (2.38) we can calculate

$$\langle n_{\mathbf{k}}^{\text{CDW}}|\, n_{\mathbf{k}}^{\text{CDW}}\rangle = \frac{1}{N}\sum_{\mathbf{R}} |\, \phi^*(\mathbf{r}-\mathbf{R})|^2\big(1 + 2U_{\mathbf{k}}V_{\mathbf{k}}\cos(\mathbf{k}_{\text{CDW}}\cdot\mathbf{R})\big) \tag{3.5}$$

which by quantum mechanics is the probability of finding a charge at position $\mathbf{r}$. One will compare this result with the probability due to the un-reconstructed state

$$\langle n_{\mathbf{k}}|\, n_{\mathbf{k}}\rangle = \frac{1}{N}\sum_{\mathbf{R}} |\, \phi^*(\mathbf{r}-\mathbf{R})|^2 \tag{3.6}$$

which maintains that a single charge can be found with equal probability in any lattice site. We then conclude that $|\, n_{\mathbf{k}}^{\text{CDW}}\rangle$ corresponds to a nonuniform charge occupancy in the lattice. The modulation is a simple sinusoidal wave, with the amplitude determined by the product $2U_{\mathbf{k}}V_{\mathbf{k}}$, which we shall correspondingly refer to as the *modulation parameter* henceforward.

Imagine an electron in the quantum state $|\, n_{\mathbf{k}}^{\text{CDW}}\rangle$. According to our result in Eq (3.5), the electron will appear in the troughs (peaks) of the potential of the distorted lattice if the modulation parameter takes positive (negative) values. Apparently the energy will be different between the two situations. The difference is

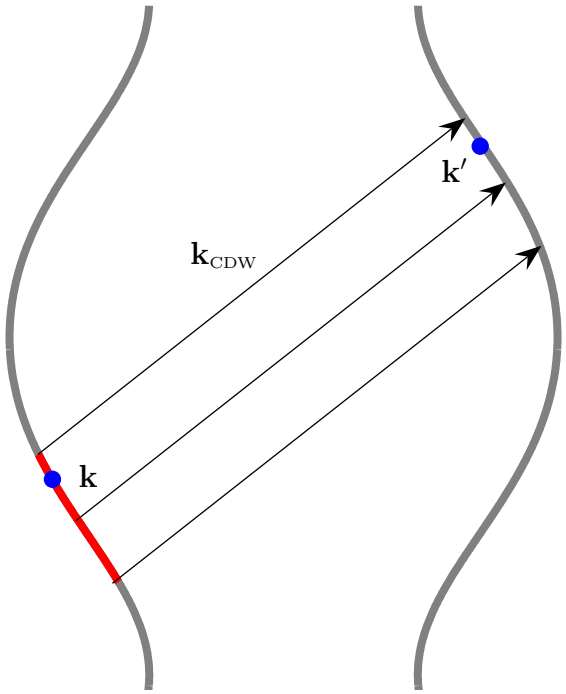

Figure 3.1: Back scattering on a two-dimensional Fermi surface. When traveling in the distorted lattice, the state $\mathbf{k}$ is subject to an extra momentum $\mathbf{k}_{\mathrm{CDW}}$ and will appear as $\mathbf{k}'$ on the opposite side of the Fermi surface. Accordingly, the quantum state is described as a superposition of $\mathbf{k}$ and $\mathbf{k}'$. For lower-dimensional conductors, there may be parallel portions of the Fermi surface. States on these portions are connected by a single momentum.

called the CDW energy gap. By construction, the Fermi level will appear at the center of the energy gap. This means $|n_{\mathbf{k}}^{\mathrm{CDW}}\rangle$ with a positive modulation parameter will be a filled quantum state of electrons. Otherwise it is a unoccupied state.

So far we have only talked about individual states. Another important parameter which we do care about is the amplitude of the CMW. To create the full CMW, we need to add up all the reconstructed states. To do so, we will specify the region in the momentum space in which the electronic states are subject to re-construction with non-zero modulation parameters. Let us denote such a region as $\{\mathbf{k}\}$. We determine the modulation of the electron density

$$\rho_{\mathrm{CDW}}(\mathbf{r}) = \frac{2}{N} \sum_{\{\mathbf{k}\}} U_{\mathbf{k}} V_{\mathbf{k}} \sum_{\mathbf{R}} |\, \phi^*(\mathbf{r} - \mathbf{R})|^2 \cos(\mathbf{k}_{\mathrm{CDW}} \cdot \mathbf{R}) \tag{3.7}$$

If we compare this result with Eq (1.1), we find the amplitude of the CMW

$$\rho_1 = 2 \sum_{\{\mathbf{k}\}} U_{\mathbf{k}} V_{\mathbf{k}} \tag{3.8}$$

We can therefore re-write Eq (3.7) as

$$\rho_{\mathrm{CDW}}(\mathbf{r}) = \frac{1}{N}\, \rho_1 \sum_{\mathbf{R}} |\, \phi^*(\mathbf{r} - \mathbf{R})|^2 \cos(\mathbf{k}_{\mathrm{CDW}} \cdot \mathbf{R}) \tag{3.9}$$

3.2 Peierls Model of CDW

Let us then steer our focus toward the origin of the CDW state. The mechanism by which CDWs develop is first described in mid 1950's by Peierls, and independently by Fröhlich [1, 2]. According to the theory, CDWs arise due to the spontaneous symmetry breaking which happens only in conductors with reduced dimensionality. In this section we highlight the theory by giving its most important results. Interested readers are recommended to read the references for further details [3].

We will assume the solid is a one-dimensional metal. Before CDW formation,

conduction-band electrons are considered to be an free electron gas. The Fermi vector and the Fermi energy will be denoted as $\mathbf{k}_F$ and ϵ_F, respectively. For convenience we will assume the lattice is a monoatomic lattice.

3.2.1 CDW in Mean-Field Theory

In 1954, Frohlich wrote down the equation that defines a CDW Hamiltonian as follows

$$\mathcal{H}_0 = \sum_{\mathbf{k}} \epsilon_{\mathbf{k}} a^\dagger_{\mathbf{k}} a_{\mathbf{k}} + \sum_{\mathbf{q}} \hbar\omega_{\mathbf{q}} b^\dagger_{\mathbf{q}} b_{\mathbf{q}} + \sum_{\mathbf{k},\mathbf{q}} \widetilde{g}_{\mathbf{q}} a^\dagger_{\mathbf{k}+\mathbf{q}} a_{\mathbf{k}} (b^\dagger_{-\mathbf{q}} + b_{\mathbf{q}}) \tag{3.10}$$

In this equation, $a^\dagger_{\mathbf{k}}$ and $a_{\mathbf{k}}$ are the creation and annihilation operators for the electron states with energy $\epsilon_{\mathbf{k}}$, whereas $b^\dagger_{\mathbf{q}}$ and $b_{\mathbf{q}}$ are the creation and annihilation operators for the phonons with energy $\hbar\omega_{\mathbf{q}}$. Interaction takes place via the last term, which arises because of scattering between the electrons and the phonons. The coupling constant

$$\widetilde{g}_{\mathbf{q}} = i(\frac{\hbar}{2M\omega_{\mathbf{q}}})^{\frac{1}{2}} |\mathbf{q}| \, \widetilde{V}_{\mathbf{q}} \tag{3.11}$$

is proportional to the Fourier transformation $\widetilde{V}_{\mathbf{q}}$ of the ionic potential due to the underling lattice. M is the ion mass.

Ground state: the CDW condensate

Given Eq (3.10) as the Hamiltonian, we ask in what physical state the solid will be found at different temperatures. With suitable assumptions, the problem can easily be solved by standard methods. For example, one can assume that every electron feels an "averaged" potential caused by the lattice and by all other electrons — a crucial assumption called the mean-field approximation. When determining the electron-phonon scattering around the Fermi level, one can use the result of the

well-known Lindhard theory [4]. It turns out the solid will retain its metallic characteristics until the temperature reaches T^{MF}, where a phase transition will occur. Known as a CDW condensate, the low-temperature phase consists of a distorted lattice and a periodic modulation of the conduction charge density. Around the Fermi level, quasiparticle excitations exhibit a BCS-type energy gap. Instead of a metal, the solid becomes a semiconductor.

CDW dispersion and density of states

In Figure 3.2 we show the electrons' dispersion relation around the Fermi level. Before CDW formation, the dispersion relation is a continuous function, which can be approximated as

$$\epsilon(\mathbf{k}) = \epsilon_F + \hbar \mathbf{v}_F \cdot (\mathbf{k} - \mathbf{k}_F) \tag{3.12}$$

where $\mathbf{v}_F = \partial\epsilon/\partial\mathbf{k}$ is the Fermi velocity and ϵ_F is the Fermi energy. After the solid develops the CDW, the dispersion relation becomes

$$E(\mathbf{k}) = \epsilon_F + \text{sign}\Big(\mathbf{v}_F \cdot (\mathbf{k} - \mathbf{k}_F)\Big)\Big([\hbar \mathbf{v}_F \cdot (\mathbf{k} - \mathbf{k}_F)]^2 + \Delta^2\Big)^{\frac{1}{2}} \tag{3.13}$$

which, at $\mathbf{k} = \mathbf{k}_F$, produces an energy gap whose size is [3]

$$2\Delta \;=\; 3.52\, k_B T^{\text{MF}} \tag{3.14}$$

The ground state can be obtained by filling the lower branch with electrons. At zero temperature, the upper branch is completely empty. Thermally excited electrons, however, will cross the energy gap when the temperature is different from absolute zero.

From the dispersion relation one can calculate the density of states (DOS) in the solid. Let $N_e(\epsilon)$ and $\varrho(E)$ be the functions of the DOS before and after formation of the CDW state, respectively. As the original dispersion relation is linear, N_e is a constant. By construction, the statement $\varrho(E)\; dE = N_e\; d\epsilon$ must

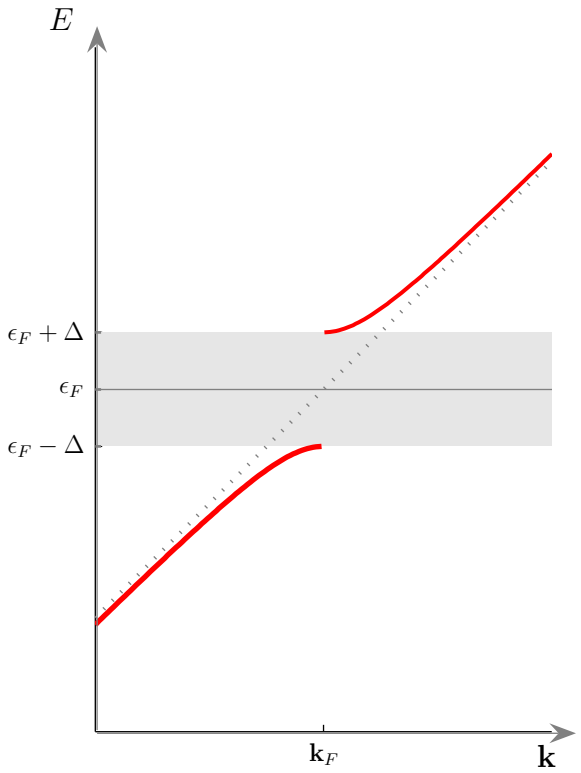

Figure 3.2: An energy gap is opened at the Fermi level due to CDW formation. Notice that deviations occur only around the Fermi level. In this region, we can replace the original dispersion relation by a linear function.

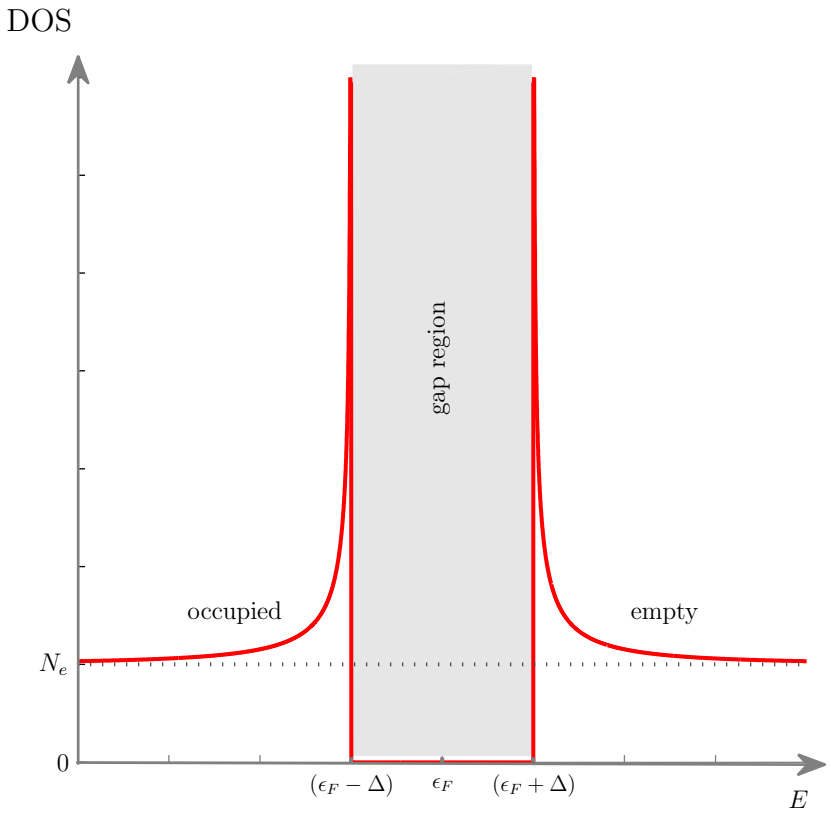

Figure 3.3: The DOS of the CDW state. Due to CDW formation, states are removed from the energy gap and become densely populated around the edges of the gap.

hold. It follows the DOS of the CDW can be written as

$$\varrho(E) = N_e \frac{d\epsilon}{dE} = \begin{cases} \dfrac{E-\epsilon_F}{\sqrt{(E-\epsilon_F)^2-\Delta^2}} \cdot N_e & |E-\epsilon_F| > \Delta \\ 0 & |E-\epsilon_F| < \Delta \end{cases} \tag{3.15}$$

remembering our definition of E in Eq (3.13). We plot this density of state in Figure 3.3. Note the DOS shows substantial deviations from N_e in the vicinities of $\epsilon_F \pm \Delta$. By integrating the difference between $\varrho(E)$ and N_e, we verify that the excess comes from the gap region

$$\int_{\epsilon_F+\Delta}^{\infty} \Big(\varrho(E) - N_e \Big)\, dE = N_e \cdot \Delta \tag{3.16}$$

The size of the gap is directly proportional to the number of the states that participate in CDW formation.

The modulation parameter

We have been using the phrase "reconstruction" when two Bloch states are mixed and their energy re-calculated in the CDW condensate. As we described in the last section, $U_{\mathbf{k}}$ and $V_{\mathbf{k}}$ correspond to the amplitudes of the two Bloch waves. This construction turns out to be a simple illustration of the Bogliubov transformation, provided one recognizes that Bloch waves are the correct basis states to use. Our notation $U_{\mathbf{k}}$ and $V_{\mathbf{k}}$ is borrowed directly from the standard Bogoliubov context. With the definition of $\theta_{\mathbf{k}}$ as

$$\tan\theta_{\mathbf{k}} = -\frac{\Delta}{\epsilon(\mathbf{k}) - \epsilon_F} \tag{3.17}$$

the mean-field theory determines the coefficients

$$U_{\mathbf{k}} = \sin(\frac{\theta_{\mathbf{k}}}{2}) \tag{3.18}$$

$$V_{\mathbf{k}} = \cos(\frac{\theta_{\mathbf{k}}}{2}) \tag{3.19}$$

Note that the normalization condition Eq (3.4) is automatically satisfied. The modulation parameter in turn can be written as

$$2\,U_{\mathbf{k}}V_{\mathbf{k}} = -\,\frac{\Delta}{\sqrt{(\epsilon(\mathrm{k}) - \epsilon_F)^2 + \,\Delta^2}} \tag{3.20}$$

Using the one-to-one correspondence between Eq (3.12) and (3.13), we can express the modulation parameter as a function of $E(\mathbf{k})$. We plot the function in Figure 3.4. The absolute value of $2U_{\mathbf{k}}V_{\mathbf{k}}$ is decreasing rather slowly moving away from the energy gap, with the maximum equal to unity at $\epsilon_F \pm \Delta$. Above the gap, $2\,U_{\mathbf{k}}V_{\mathbf{k}}$ takes negative values. We associate this behavior with the unoccupied states of the CMW. The fact the $\mid 2U_{\mathbf{k}}V_{\mathbf{k}} \mid \leq 1$ means that most of the time the reconstructed states are only partially modulated. The situation is then very similar to the two-fluid model used to describe superfluid ^{4}He.

3.2.2 Beyond the One-Dimensional Model

Because there are indeed three dimensions in nature, it is very important that we understand our theory of the one-dimensional CDW is only a model. Although we determined T^{MF} for the CDW phase transition, the mean-field approximation neglects the important role played by fluctuations. In three-dimensions CDW formation concerns ordering not only along the $\mathbf{k}_{\mathrm{CDW}}$ direction but also in the directions perpendicular to $\mathbf{k}_{\mathrm{CDW}}$. Fluctuations actually prevent the CDW state from forming until the system is cooled to a still lower temperature T^{3D}. It has been determined that [5]

$$T^{\mathrm{3D}} \cong 0.25\,T^{\mathrm{MF}} \tag{3.21}$$

See the discussion in Figure 3.5. Below T^{3D}, CDWs are developed with three-dimensional long-range correlations. Properties of the corresponding phase transi-

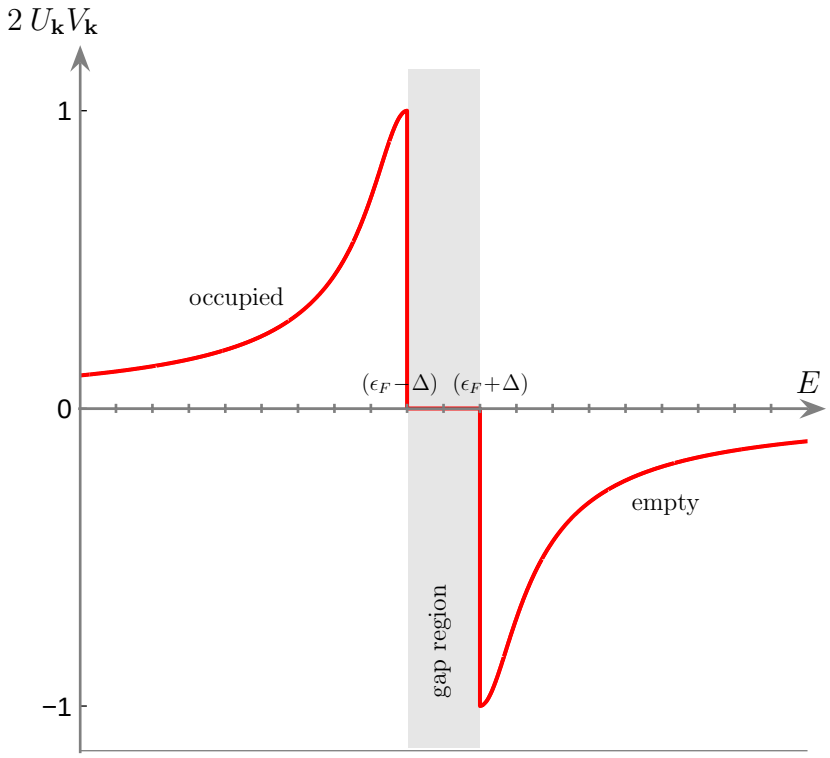

Figure 3.4: The modulation parameter as a function of reconstructed energy E. The function takes negative (positive) values above (below) the energy gap, corresponding to modulation of the unoccupied (occupied) states in this region.

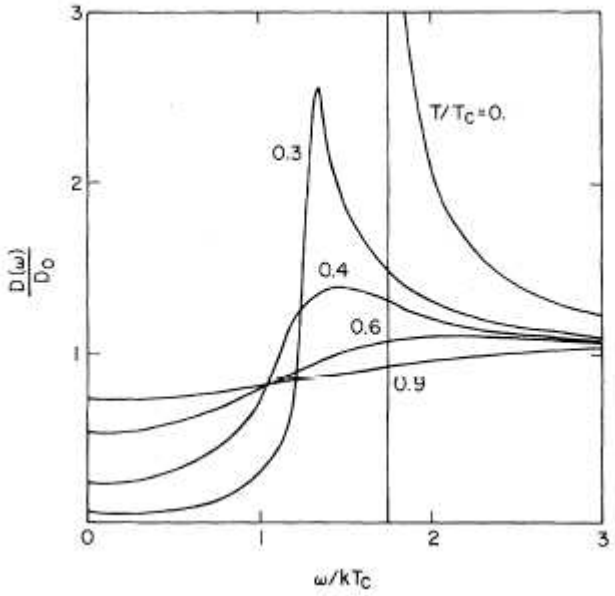

Figure 3.5: In three dimensions, fluctuations become such an important effect that CDW can only develop good spatial order within a finite range. The diminished correlations lift the state's restriction on appearing inside the mean-field-theory gap. The quasi-particle excitation is then characterized by a dispersion relation with a so-called pseudogap, whose size and shape will change considerably with the temperature. In this figure, the reconstructed DOS is plotted against $(E - \epsilon_F)/(k_B T^{\text{MF}})$ at various temperatures (with T_C equivalent to our T^{MF}). The DOS is normalized according to the metallic DOS. A gap-like feature begins to emerge around $T^{\text{3D}} = 0.2 \sim 0.3\, T^{\text{MF}}$. Reproduced from Ref. [5].

tions have been studied in various systems [6].

In real materials, Fermi surfaces may correspond to a very complicated geometry. Strong back scattering can happen whenever two areas on the Fermi surface are connected by a single wavevector. Symmetry often allows this to occur in several directions. As a result, the CDW state must be characterized by multiple wavevectors. However, the different components can actually be considered as coexisting one-dimensional CDWs. It will be discussed in the next section that the CDW state of $1T$-TaS_2 consists of three one-dimensional CDWs. [2]

We use Figure 3.6 to illustrate how states can get reconstructed in a two-dimensional system. In this example, we find large segments of the Fermi surface connected to one another by either $\mathbf{k}_{\mathrm{CDW1}}$ or $\mathbf{k}_{\mathrm{CDW2}}$. Energy gaps will be opened at these segments. There will be two independent CDWs. Around the energy gaps the modulation parameter takes nonzero values. As far as the unoccupied CMW states are concerned, we look at states staying outside the Fermi surface. Accordingly we obtain the wavevector set $\{\mathbf{k}\}$. Outside $\{\mathbf{k}\}$, states do not participate in forming the CDWs. The DOS remains finite at the Fermi level. The system is characterized as a metal.

3.3 CDW of $1T$-TaS_2

We may begin our discussion of real CDWs. Provided the temperature is not too high (< 543 K), there will be a distorted lattice plus a conduction-electron density modulation in a $1T$-TaS_2 crystal [8]. The CDW state of $1T$-TaS_2 corresponds to three different phases, depending on how the LDW is registered to the lattice. They are the incommensurate (IC) phase existing at high temperatures (> 350 K), the nearly-commensurate (NC) phase existing at medium temperatures

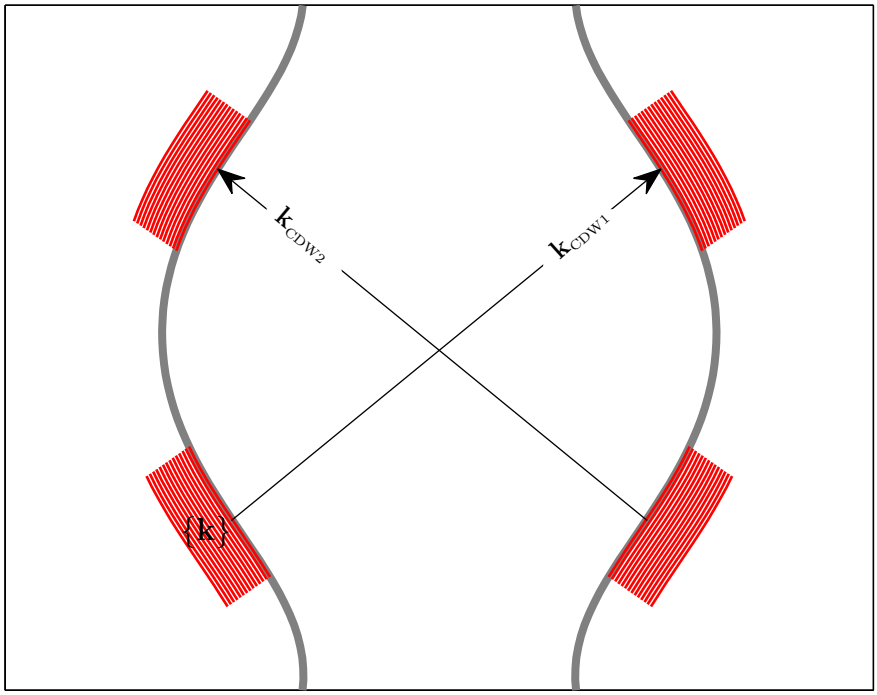

Figure 3.6: Independent wavevectors $\mathbf{k}_{\mathrm{CDW1}}$ and $\mathbf{k}_{\mathrm{CDW2}}$ connect the four groups of states appearing on the opposite sides of the Fermi surface, which, in two-dimension, consists of separate curves. Two CDWs will form. The colored area indicates the wavevector set $\{\mathbf{k}\}$. Due to CDW formation, states in $\{\mathbf{k}\}$ are reconstructed, resulting in a modulated distribution for the unoccupied states. Note the DOS remains finite at the Fermi level. The rectangle represents the zone boundary.

(350 K $\sim$ 180 K), and the commensurate (C) phase existing at low temperatures ($<$ 180 K). Neither of the phase transitions is characterized by any sharp transition. The IC-to-NC-to-C evolution corresponds to a gradual development of long-range correlations.

As we have described in the last section, the CDW of $1T$-TaS_2 can be decomposed into three one-dimensional CDWs. To discuss the properties of the component CDWs, we need to explain the crystalline structure and the reciprocal lattice. The crystal of $1T$-TaS_2 shows a layered structure [9]. As depicted in Figure 3.7(a), the layers are essentially an Ta sheet sandwiched between two S sheets. Depending on the relative atomic coordinates inside unit cells, there are two types of layers, resulting in a variety of polymorths with different stacking orders of the basic layers. The $1\,T$ polytype consists of the so-called octahedral layers, in which Ta atoms appear at the trigonal-antiprismatic coordinations by S. The crystalline structure corresponds to the trigonal space group $P\bar{3}m1$. One readily notices the large inter-layer distance as the origin of the highly anisotropic electronic characteristic favorable in CDW formation.

The three component CDWs are characterized by their wavevectors as

$$\begin{cases} \mathbf{k}_{\mathrm{CDW1}} = \mathbf{q}_1 + \mathbf{q}_3 \\ \mathbf{k}_{\mathrm{CDW2}} = -\mathbf{q}_2 + \mathbf{q}_3 \\ \mathbf{k}_{\mathrm{CDW3}} = -\mathbf{q}_1 + \mathbf{q}_2 + \mathbf{q}_3 \end{cases} \tag{3.22}$$

where $\mathbf{q}_3 = \mathbf{c}_0^*/3$. Sitting in the $\mathbf{a}_0$-$\mathbf{b}_0$ plane, $\mathbf{q}_1$ and $\mathbf{q}_2$ are 60° apart from each other, and each corresponds to the same length of approximately one quarter of $\mathbf{a}_0^*$. See Figure 3.7(b). The lengths and the orientations of these in-plane components are indeed temperature dependent. At room temperature (298 K), $\mathbf{q}_1 = 0.245\mathbf{a}_0^* + 0.068\mathbf{b}_0^*$ and $\mathbf{q}_2 = -0.068\mathbf{a}_0^* + 0.313\mathbf{b}_0^*$ [3]. As temperature decrease these two vectors will rotate. Eventually they become locked at $\mathbf{q}_1 = \mathbf{q}_{1c} \equiv (3\mathbf{a}_0^* + \mathbf{b}_0^*)/13$ and $\mathbf{q}_2 = \mathbf{q}_{2c} \equiv (-\mathbf{a}_0^* + 4\mathbf{b}_0^*)/13$ in the C phase.

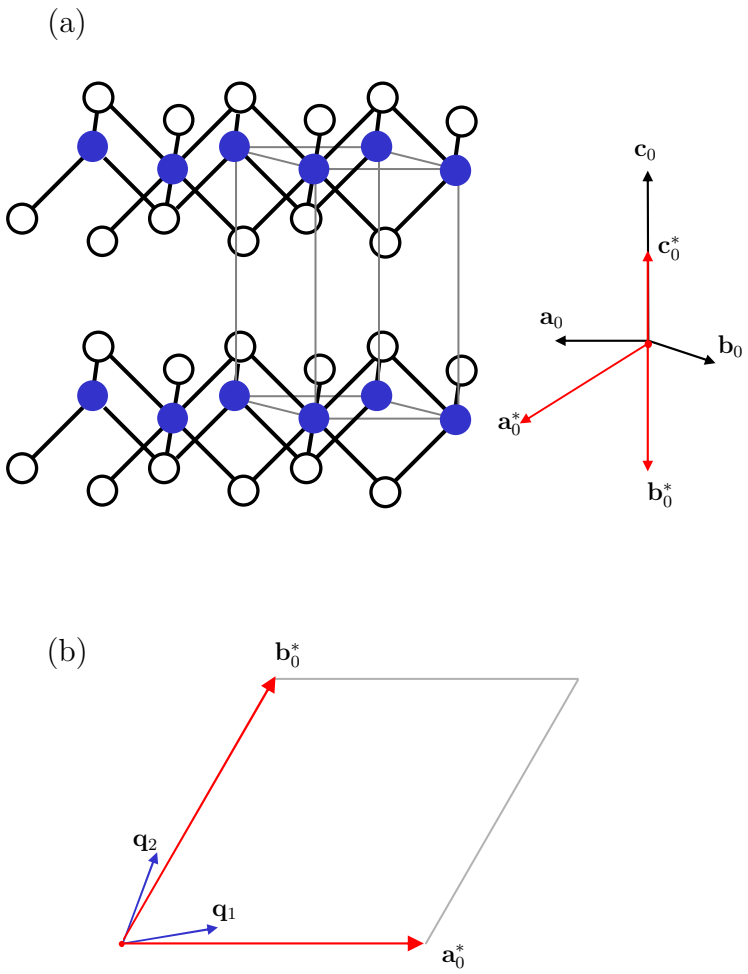

Figure 3.7: (a) $1T$-TaS_2 corresponds to a hexagonal lattice structure, with $\mathbf{a}_0 = \mathbf{b}_0 = 3.365$Å and $\mathbf{c}_0 = 5.897$Å. Each unit cell contains one Ta at $(0, 0, 0)$ and two S at $\pm(\frac{1}{3}, \frac{2}{3}, z)$, where $z \approx 0.25$. The Ta atoms are represented by filled circles. The lattice basis are specified for both the direct lattice and the reciprocal lattice. (b) The unit cell spanned by $\mathbf{a}_0^*$ and $\mathbf{b}_0^*$. $\mathbf{q}_1$ $(-\mathbf{q}_2)$ represents the in-plane component when $\mathbf{k}_{\text{CDW1}}$ $(\mathbf{k}_{\text{CDW2}})$ is projected onto the $\mathbf{a}_0$-$\mathbf{b}_0$ plane.

3.3.1 Constructing the LDW

Clearly $\mathbf{k}_{\mathrm{CDW1}}$, $\mathbf{k}_{\mathrm{CDW2}}$, and $\mathbf{k}_{\mathrm{CDW3}}$ are linearly independent. As we will show, this gives the LDW its nature of being a three-dimensional displacement vector. For an atom located at $\bar{\mathbf{r}}$, the displacement can be described as a function $\Delta\mathbf{u}(\bar{x}_1, \bar{x}_2)$, with the variables $\bar{x}_1$ and $\bar{x}_2$ being defined as

$$\begin{aligned} \bar{x}_1 &= \mathbf{q}_1 \cdot \bar{\mathbf{r}} \ + \ t_1 \\ \bar{x}_2 &= \mathbf{q}_2 \cdot \bar{\mathbf{r}} \ + \ t_2 \end{aligned} \tag{3.23}$$

As $\bar{x}_1$ and $\bar{x}_2$ will eventually appear in sinusoidal functions, t_1 and t_2 parameterize the phases of each variable, respectively. Their values are specified by the layer in which the atom dwells.[1]. Since the LDW is periodic, one can write the displacement as a Fourier expansion

$$\Delta\mathbf{u}_j^{\alpha}(\bar{x}_1,\bar{x}_2) = \sum_{n_1=0}^{\infty}\sum_{n_2=0}^{\infty}\{A^{\alpha}_{j\,n_1 n_2}\sin(2\pi n_1\bar{x}_1 + 2\pi n_2\bar{x}_2) + B^{\alpha}_{j\,n_1 n_2}\cos(2\pi n_1\bar{x}_1 + 2\pi n_2\bar{x}_2)\} \tag{3.24}$$

where α stands for the Cartesian coordinates x,y,z, j indicates the atom, and n_1, n_2 defines the orders of the harmonics. Note the term $(n_1, n_2) = (0, 0)$ must be excluded from the summation. The properties of the LDW such as its amplitude, direction and symmetry are all contained in the coefficients $A^{\alpha}_{j\,n_1 n_2}$ and $B^{\alpha}_{j\,n_1 n_2}$. Thanks to the careful work done by crystallographers using conventional x-ray diffraction, these coefficients have been determined for the NC phase and are tabulated in the literature [3]. Taking advantage of these known values[2] we evaluate $\Delta\mathbf{u}_j^{\alpha}$ for both Ta and S. The displacement is then combined with the original lattice to create the distorted lattice. In Figure 3.8 we show the LDW in

[1]It is the relative values of t_1 (and t_2) between different layers that matter in using this parameter in $\Delta\mathbf{u}(\bar{x}_1, \bar{x}_2)$. They need to be correctly chosen so the LDW obey the known symmetry. See section V, part B in Ref. [3]

[2]For notation consistency we change the notation $A^{\mu}_{n_1 n_2 \alpha}$ used in the reference to our own notation $A^{\alpha}_{j\,n_1 n_2}$. Same is for $B^{\mu}_{n_1 n_2 \alpha}$.

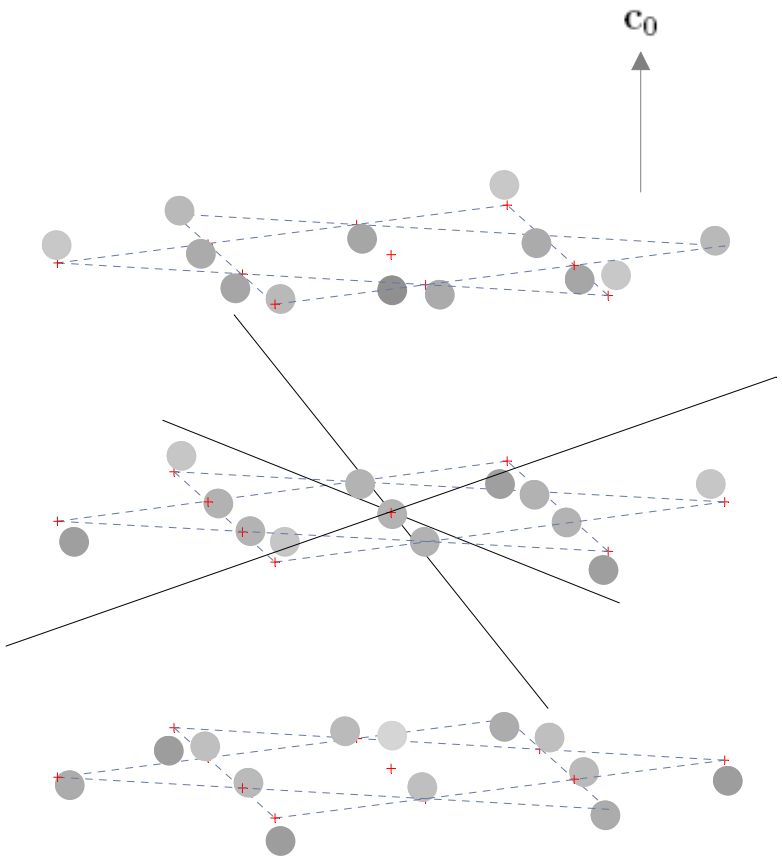

Figure 3.8: The supercell of the LDW in the NC phase, corresponding to a volume equal to a CDW period. For clarity reason, only the Ta positions are shown. The red crosses indicate the original lattice sites. The displacement has been exaggerated in the $\mathbf{c}_0$-direction so it becomes visible for most atoms. The actual displacement is only about 2% of $|\mathbf{c}_0|$ in the $\mathbf{c}_0$-direction and about 5% of $|\mathbf{a}_0|$ in the $\mathbf{a}_0$-$\mathbf{b}_0$ plane. The black straight lines are plotted to show the directions of the three component CDWs.

the NC phase inside a volume of $\sqrt{13}\,\mathbf{a}_0 \times \sqrt{13}\,\mathbf{b}_0 \times 3\mathbf{c}_0$. The entire LDW can be obtained by repeating this very same structure with suitable phases in a spatial period equal to this volume, which hence will be referred to as the supercell of the CDW hereafter.

Looking at the internal structure of the supercell, we realize the LDW corresponds to atomic displacement showing both the in-plane component (parallel to the $\mathbf{a}_0$-$\mathbf{b}_0$ plane) and the out-of-plane component (along the $\mathbf{c}_0$-direction). Within each layer, the outer atoms all move inward, resulting in an atomic cluster consisting of thirteen unit cells known as "the stars of David". Meanwhile, the distances between the atoms at the centers of the clusters are decreased due to the out-of-plane motion of these atoms. There is therefore a direct coupling between the adjacent layers. Although we do not have S shown in the figure, they basically follow the movement of the Ta atoms. The Ta-S bonds essentially maintain the same lengths, regardless of the fact that the lattice is now distorted by the CDW.

3.3.2 Characterizing the CMW

For the CMW we are concerned with its size and the corresponding quantum states. This perspective is shared in other studies including CDW transport [11], Hall effect [12] and photoelectron spectroscopy [13]. It should not be surprising that we will begin to talk about the band structure of the valence bands. The CMW is indeed an effect of valence band reconstruction.

To best appreciate the effect, let us describe the CMW in accordance with formation of the LDW. If there is no distortion in the underlying lattice, one will determine the band structure based on the basic structure of the unit cell. In the tight-binding band structure calculation [14], it is shown that in $1T$-TaS_2 the most

important valence bands are derived from the Ta-5d orbitals and the S-3p orbitals. Moreover, the Ta-5d bands are spontaneously split into non-overlapping subbands, with the lower triply degenerate subband being referred to as the t_{2g} subband and the upper double degenerate subband as the e_g subband. t_{2g} and e_g correspond to bandwidths of 4 eV and of 2.5 eV, respectively. The Fermi level lies in the lower portion of the t_{2g} subband. See[3] Figure 3.9.

As soon as the material enters the CDW state, the lattice becomes distorted. Correspondingly the band structure will be modified. Technically speaking, we would then determine the band structure for the supercell (Figure 3.8). We obtain the *reconstructed* bands. The fact the supercell contains thirteen times more atoms than the basic unit cell means each band must split into thirteen reconstructed bands. As we are mostly interested in states that stay close to the Fermi level, we show in Figure 3.10 the lowest-lying Ta-5d band and the corresponding reconstructed bands [5].

The CMW takes place in this reconstructed band structure as follows. Consider a cluster of thirteen unit cells. While every Ta owns three 5d electrons, formation of the Ta-S covalent bonds uses two electrons, leaving the last electron to create the valence bands. In turn there are total of thirteen band electrons in each cluster. The electrons should then be placed in the reconstructed bands. As Figure 3.10 suggests, we end up with six fully occupied bands, all of which appear at least 0.4 eV below the Fermi energy. In other words, the Fermi surface is conceivably gapped. Meanwhile, the seventh band, now home of the thirteenth electron, shows very little dispersion in all directions except Γ-A. In real space, this means the thirteenth electron is localized in the $\mathbf{a}_0$-$\mathbf{b}_0$ plane but delocalized in the $\mathbf{c}_0$ direction. In fact, the electron will be found at the cluster center. Hence we

[3]We notice the DOS shown in the Figure 3.9 is actually obtained by assuming a distorted lattice. However, due to the large core-hole lifetime used in the calculation, the DOS will not be sensitive to the change of the lattice.

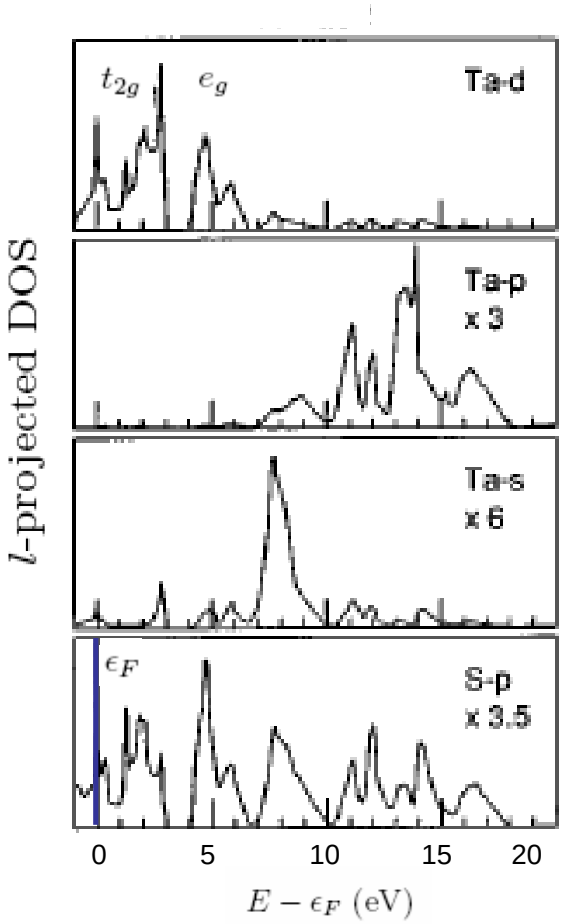

Figure 3.9: Rather than studying the band structure in the momentum space, one can project the valence bands onto the different atomic orbitals and determine the angular-momentum-projected components of the DOS. It can be clearly seen that formation of the bands is due to the overlaps between the $5d$ orbital of Ta and the $2p$ orbital of S. Within the energy range of the Ta-$5d$ bands, two subbands t_{2g} and e_g, each of which corresponds to a bandwidth of 4 eV and of 2.5 eV, respectively, are separated by a 1-eV-wide band gap. Reproduced from [4]

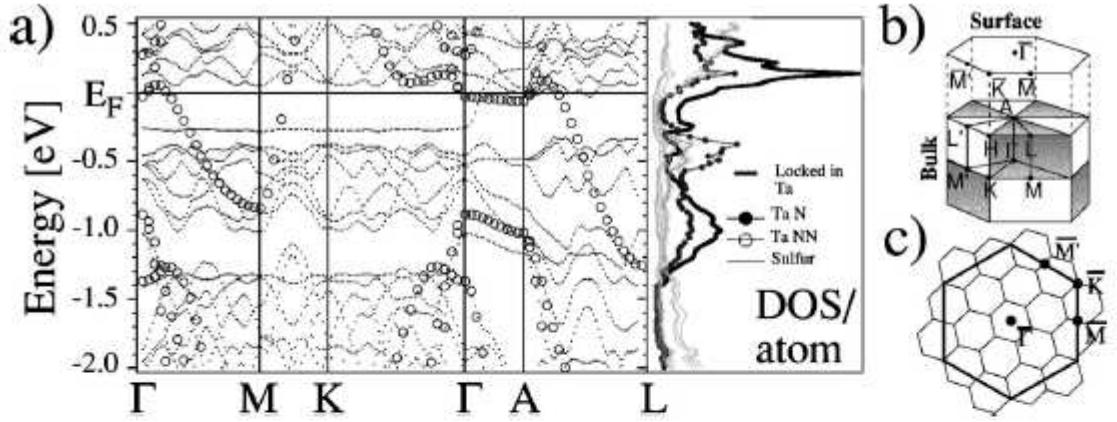

Figure 3.10: Band structure calculations for wavevectors along high symmetry directions within the unreconstructed Brillouin zone (BZ). (a) Superposition of both, the *unreconstructed* (open circles) and the CDW reconstructed (dots) cases. The fact that there are those six reconstructed bands staying completely below the Fermi level means the Fermi surface is largely gapped. Being partially occupied, the seventh reconstructed band is the only place at the Fermi level where the energy still grows continuously with increasing momentum. (b) Surface and bulk BZ's. (c) *Reconstructed* (thin lines)-*unreconstructed* (think lines) surface BZ's correspondence. Reproduced from [5].

determine the charge modulation of the CMW is equal to *one* electron per cluster[4]. A band character analysis indicates that the electron has mostly d_{z^2} character.

Yet the CMW is a still more interesting phenomena than the reconstructed band structure. In the C phase, CMW transport is characterized by a surprisingly large resistivity, which can not be understood in the context of the conventional CDW theory [17]. Additional mechanisms, acting with or besides the Peierls mechanism, have therefore been invoked to account for the development of the CMW in $1T$-TaS_2. Emphasizing the importance of the CMW correlation, Fazekas and Tosatti proposed a theory in which the NC-C phase transition is accompanied by Mott localization of the mentioned thirteenth electron [18, 19]. Indeed, the theory is corroborated by the observation that in the C phase the CMW exhibits a pseudogap of $150 \sim 200$ meV at the Fermi level [20].

The fact that the CMW demands a different mechanism to account for its development indicates the CMW does not necessarily share the same spatial structure with the LDW. It is therefore of great importance to ask whether one can directly measure the spatial structure of the CMW, for example, by using resonant x-ray diffraction.

3.4 Summary

In this chapter we performed a theoretical study the CDW of $1T$-TaS_2. It is found there are three coexisting one-dimensional components in this CDW. The LDW is characterized by the $\sqrt{13}\times\sqrt{13}\times 3$ supercell, in which all the atomic displacements are known. Meanwhile, the CMW is a rather small charge density modulation in

[4]For simplicity we assume that one can ignore the temperature dependence of the CDW amplitude.

the conduction bands, with the corresponding wave function being made of the Ta $5d_{z^2}$ orbital. When the CDW is cooled from the N-C phase into the C phase, the CMW is subject to some fundamental changes in its energy and spatial structures. In the next chapter, we shall then study how these properties determine x-ray diffraction from this interesting CDW.

BIBLIOGRAPHY

[1] R. E. Peierls. *Quantum Theory of Solids*. Oxford University Press, Oxford, 2001. Reading.

[2] H. Fröhlich. On the theory of superconductivity: the one-dimensional case. *Proceedings of the Royal Society London, Series A*, 223(1154):296–305, May 1954.

[3] G. Grüner. *Density Waves in Solids*. Addison-Wesley, MA, 1994. Reading.

[4] Neil W. Ashcroft and N. David Mermin. *Solid State Physics*. Harcourt, Inc., FL, 1976. Discussion of the Lindhard theory.

[5] P. A. Lee, T. M. Rice, and P. W. Anderson. Fluctuation effects at a peierls transition. *Phys. Rev. Lett.*, 31(7):462–465, Aug 1973.

[6] R. Moret and J. P. Pouget. *Crystal Chemistry and Properties of Materials with Quasi-one-dimensional Structures*, chapter Structural Studies of Phase Transitions in One-Dimensional Conductors.

[7] J. A. Wilson, F.J. Di Salvo, and S. Mahajan. Charge-density waves and superlattices in the metallic layered transition metal dichalcogenides. *Advances in Physics*, 24(2):117–201, 1975. Relating CDW formation to the band structure.

[8] Xian Liang Wu and Charles M. Lieber. Direct observation of growth and melting of the hexagonal-domain charge-density-wave phase in $1T$-TaS_2 by scanning tunneling microscopy. *Phys. Rev. Lett.*, 64(10):1150–1153, Mar 1990.

[9] F. Jellinek. The system tantalum-sulfur. *Journal of the Less Common Metals*, 4(1):9–15, February 1962.

[10] Albert Spijkerman, Jan L. de Boer, Auke Meetsma, Gerrit A. Wiegers, and Sander van Smaalen. X-ray crystal-structure refinement of the nearly commensurate phase of $1T$-TaS_2 in $(3 + 2)$-dimensional superspace. *Phys. Rev. B*, 56(21):13757–13767, Dec 1997.

[11] A. H. Thompson, R. F. Gamble, and J. F. Revelli. Transitions between semiconducting and metallic phases in $1T$-TaS_2. *Solid State Communications*, 9(13):981–985, 1971.

[12] R. Inada, Y. Onuki, and S. Tanuma. Hall effect of $1T$-TaS_2 and $1T$-$TaSe_2$. *Physica B*, 99(1-4):188–192, 1980.

[13] B. Dardel, M. Grioni, D. Malterre, P. Weibel, Y. Baer, and F. Lévy. Spectroscopic signatures of phase transitions in a charge-density-wave system: $1T$-TaS_2. *Phys. Rev. B*, 46(12):7407–7412, Sep 1992.

[14] L. F. Mattheiss. Band structures of transition-metal-dichalcogenide layer compounds. *Phys. Rev. B*, 8(8):3719–3740, Oct 1973.

[15] Z. Y. Wu, G. Ouvrard, P. Moreau, and C. R. Natoli. Interpretation of preedge features in the Ti and S K-edge x-ray-absorption near-edge spectrain the layered disulfides TiS_2 and TaS_2. *Phys. Rev. B*, 55(15):9508–9513, Apr 1997.

[16] M. Bovet, S. van Smaalen, H. Berger, R. Gaal, L. Forró, L. Schlapbach, and P. Aebi. Interplane coupling in the quasi-two-dimensional $1T$-TaS_2. *Phys. Rev. B*, 67(12):125105, Mar 2003.

[17] P. D. Hambourger and F. J. Di Salvo. Electronic conduction process in $1T$-TaS_2. *Physica B*, 99(1-4):173–176, 1980.

[18] P. Fazekas and E. Tosatti. Electrical, structural and magnetic properties of pure and doped $1T$-TaS_2. *Philosophical Magazine Part B*, 39(3):229–244, 1979.

[19] P. Fazekas and E. Tosatti. Charge carrier localization in pure and doped $1T$-TaS_2. *Physica B*, 99(1-4):183–187, January 1980.

[20] B. Dardel, M. Grioni, D. Malterre, P. Weibel, Y. Baer, and F. Lévy. Temperature-dependent pseudogap and electron localization in $1T$-TaS_2. *Phys. Rev. B*, 45(3):1462–1465, Jan 1992.

CHAPTER 4

X-RAY DIFFRACTION FROM CDWS

When x-ray scattering was discussed in Chapter 2, our results were given based on the physical concept of the cross-section. Here however, for x-ray diffraction, we must take into account the important relative phases of scattering created by individual scatterers, together with the general (and profound) effects such as absorption and extinction. For the CDW, as far as the phenomenology is concerned, the LDW and the CMW can be viewed as two independent superstructures in $1T$-TaS_2. In this chapter, we will explain how x-ray diffraction is created by each kind of the two superstructures. The discussion will be given in the framework of the kinematic theory of x-ray diffraction. As we will point out, x-ray absorption plays an important role in resonant x-ray diffraction. In the kinematic theory, the corresponding effect is described by the absorption correction μ^{-1}, where μ is the absorption coefficient. For comparison, we will also study x-ray diffraction by the lattice structure of $1T$-TaS_2 at the Bragg peaks, taking into account the effect of resonant x-ray scattering. As we found resonant x-ray diffraction indeed results from an intriguing interplay between x-ray scattering and x-ray absorption, this careful study of the diffraction theory proves to be the key to understanding the energy dependence of the intensities of the CDW satellites.

4.1 CMW Effect in X-ray Scattering

We have shown that the CMW is a phenomenon in the valance bands. In x-ray scattering, this means its effect is considered in the dispersion correction, suggesting we look carefully into the results given in Section 2.2.3. As required by

Eq (2.35), we must know the matrix elements. In order to do so, we recall the reconstructed state of the CDW in Eq (3.2). Let us create a shorthand

$$\mathrm{M}_s^{\beta\alpha} \equiv \frac{1}{N}\langle s|\mathbf{p}_s^{\beta}|\phi^*\rangle\langle\phi^*|\mathbf{p}_s^{\alpha}|s\rangle \tag{4.1}$$

which enables us to write down the following expression for the the product of the matrix elements[1]

$$\begin{aligned}\langle s|\mathbf{p}_s^{\beta}|n_{\mathbf{k}}^{\mathrm{CDW}}\rangle\langle n_{\mathbf{k}}^{\mathrm{CDW}}|\mathbf{p}_s^{\alpha}|s\rangle &= (1 + U_{\mathbf{k}}V_{\mathbf{k}}\, e^{i\mathbf{k}_{\mathrm{CDW}}\cdot\mathbf{R}} + U_{\mathbf{k}}V_{\mathbf{k}}\, e^{-i\mathbf{k}_{\mathrm{CDW}}\cdot\mathbf{R}})\mathrm{M}_s^{\beta\alpha} \\ &= \Big(1 + 2U_{\mathbf{k}}V_{\mathbf{k}}\cos(\mathbf{k}_{\mathrm{CDW}}\cdot\mathbf{R})\Big)\mathrm{M}_s^{\beta\alpha}\end{aligned} \tag{4.2}$$

A similar result can be found for $\langle s|\mathbf{p}_s^{\alpha}|n_{\mathbf{k}}^{\mathrm{CDW}}\rangle\langle n_{\mathbf{k}}^{\mathrm{CDW}}|\mathbf{p}_s^{\beta}|s\rangle$. We notice this is the same sinusoidal function describing the charge distribution in Eq (3.5). Indeed, there exists a close relation between the charge distribution and the atomic scattering. We give our discussion as follows.

4.1.1 CMW-modulated atomic form factor

As we wrote down Eq (2.35) for x-ray scattering from a solid, we noted that the equation becomes a simple lattice sum if one can actually show that the nested summation does not depend on $\mathbf{R}$. Eq (4.2), however, maintains that there are additional structures caused by the CMW in the dispersive terms. Once the CDW is formed in the solid, we have this special region $\{\mathbf{k}\}$ in momentum space, in which we have only states with non-vanishing $U_{\mathbf{k}}V_{\mathbf{k}}$'s. If we define

$$\tilde{f}'_{\alpha\beta}(\omega) \equiv \frac{2}{m_e}\sum_{s,\mathbf{k}\in\{\mathbf{k}\}} \mathrm{Re}\Big[\,\frac{\mathrm{M}_s^{\beta\alpha}\,U_{\mathbf{k}}V_{\mathbf{k}}}{\hbar(\omega-\omega_{\mathbf{k}s})+i\frac{\Gamma}{2}} - \frac{\mathrm{M}_s^{\alpha\beta}\,U_{\mathbf{k}}V_{\mathbf{k}}}{\hbar(\omega+\omega_{\mathbf{k}s})}\,\Big] \tag{4.3}$$

$$\tilde{f}''_{\alpha\beta}(\omega) \equiv \frac{2}{m_e}\sum_{s,\mathbf{k}\in\{\mathbf{k}\}} \mathrm{Im}\Big[\,\frac{\mathrm{M}_s^{\beta\alpha}\,U_{\mathbf{k}}V_{\mathbf{k}}}{\hbar(\omega-\omega_{\mathbf{k}s})+i\frac{\Gamma}{2}} - \frac{\mathrm{M}_s^{\alpha\beta}\,U_{\mathbf{k}}V_{\mathbf{k}}}{\hbar(\omega+\omega_{\mathbf{k}s})}\,\Big] \tag{4.4}$$

[1]To get this result, one will need Eq (2.38) for the the tight-binding state $|n_{\mathbf{k}}\rangle$. Also recall that $|s\rangle$ represents the core-level state and therefore is localized at $\mathbf{R}$.

we can rewrite Eq (2.35) for x-ray scattering by the solid as

$$\sum_{\mathbf{R}} e^{-i\mathbf{Q}\cdot\mathbf{R}} \sum_{s(\mathbf{R}),\mathbf{k}} \frac{1}{m_e}\Big[\frac{\langle s|\mathbf{p}_s^{\beta}|n_{\mathbf{k}}\rangle\langle n_{\mathbf{k}}|\mathbf{p}_s^{\alpha}|s\rangle}{\hbar(\omega-\omega_{\mathbf{k}s})+i\frac{\Gamma}{2}} - \frac{\langle s|\mathbf{p}_s^{\alpha}|n_{\mathbf{k}}\rangle\langle n_{\mathbf{k}}|\mathbf{p}_s^{\beta}|s\rangle}{\hbar(\omega+\omega_{\mathbf{k}s})}\Big]$$
$$= \sum_{\mathbf{R}} e^{-i\mathbf{Q}\cdot\mathbf{R}}(f'_{\alpha\beta}+if''_{\alpha\beta}) + \sum_{\mathbf{R}} e^{-i\mathbf{Q}\cdot\mathbf{R}}(\tilde{f}'_{\alpha\beta}+i\tilde{f}''_{\alpha\beta})\cos(\mathbf{k}_{\mathrm{CDW}}\cdot\mathbf{R}) \qquad (4.5)$$

where we have used both Eq (2.28) and (2.29) for $f'_{\alpha\beta}$ and $f''_{\alpha\beta}$. This result should then be combined with Thomson scattering to get the cross-section. Let $\tilde{f}_{\alpha\beta} = \tilde{f}'_{\alpha\beta} + i\tilde{f}''_{\alpha\beta}$. We find scattering occurs with

$$\Big(\frac{d\sigma}{d\Omega}\Big)_{\mathrm{CMW},\alpha\beta} = r_0^2\Big|\sum_{\mathbf{R}} e^{-i\mathbf{Q}\cdot\mathbf{R}}\Big(f_{\alpha\beta}(\mathbf{Q},\omega)+\tilde{f}_{\alpha\beta}(\omega)\cos(\mathbf{k}_{\mathrm{CDW}}\cdot\mathbf{R})\Big)\Big|^2 \qquad (4.6)$$

One can give this result a simple interpretation. In the presence of the CMW, atoms continue to scatter x-rays. In addition, $\tilde{f}_{\alpha\beta}$ represents scattering by the unoccupied CMW states($U_{\mathbf{k}}V_{\mathbf{k}} < 0$). As the sinusoidal function suggests, the atomic form factor is modulated by the CMW. One can therefore regard the CMW as a superstructure. We note that in his recent work, Abbamonte adopted the same physical picture for a similar problem [6].

4.1.2 Estimating $\tilde{f}_{\alpha\beta}$

As $\tilde{f}_{\alpha\beta}$ appears as a modulation of the atomic form factor, we want to determine its relative size with respect to the dispersion correction ($f'_{\alpha\beta}+if''_{\alpha\beta}$). Since these functions are both constructed by summing over some certain intermediate states, the number of the states which are involved in each summation can serve as a simple estimate of the size of these functions. Accordingly, we create a model of the valence-band states of $1T$-TaS_2. See the discussion in Figure 4.1. Around the Fermi level, we identify the low-lying Ta-$5d_{z^2}$ band, within which the CMW is constructed in the fashion of the Peierls theory. The degree of the CMW modulation can then

be plotted as a function of energy, leading to this narrow peaked feature in the Figure at the edge of the energy gap. The conclusion is that most of the bands remain unaffected by the CMW reconstruction. As a result, the CMW has only a limited effect on the valence-band states. In terms of the atomic form factor, this means

$$\boxed{|\tilde{f}_{\alpha\beta}| \ll |f'_{\alpha\beta} + if''_{\alpha\beta}|} \tag{4.7}$$

Using this model we attempt to determine whether the CMW is a measurable effect in x-ray scattering experiments. It is evident that $\tilde{f}_{\alpha\beta}$ corresponds to a very specific range of x-ray frequency. In addition, the smallness of $\tilde{f}_{\alpha\beta}$ actually makes it still more challenging to see the CMW modulation of the atomic scattering form factor.

4.1.3 CDW satellites

Having Eq (4.6) in hand, one will still need to carry out the summation to see the **Q**-dependence of the cross-section. From the derivation given in Appendix B, we rewrite the cross-section as

$$\left(\frac{d\sigma}{d\Omega}\right)_{\mathrm{CMW},\alpha\beta} = Nr_0^2 \left\langle |f_{\alpha\beta}|^2 \sum_{\mathbf{R}} e^{i\mathbf{Q}\cdot(\mathbf{R}-\mathbf{R}_0)} + \frac{1}{4}\,|\tilde{f}_{\alpha\beta}|^2 \Big(\sum_{\mathbf{R}} e^{i\mathbf{Q}^+\cdot(\mathbf{R}-\mathbf{R}_0)} + \sum_{\mathbf{R}} e^{i\mathbf{Q}^-\cdot(\mathbf{R}-\mathbf{R}_0)} \Big) \right\rangle \tag{4.8}$$

where $\mathbf{Q}^{\pm} = \mathbf{Q} \pm \mathbf{k}_{\mathrm{CDW}}$, $\mathbf{R}_0$ stands for any arbitrary point chosen to be the origin of the lattice, and $\langle \quad \rangle$ means an average over all $\mathbf{R}_0$ [9]. Since we have not included any fluctuation in the problem, we can safely drop the average in the present calculation. We note that Eq (4.6) contains separate lattice sums. We should then recall for a sufficiently large lattice, the lattice sums take finite values only around discrete points in the **Q**-space. Given **R**, those points form the so-called reciprocal

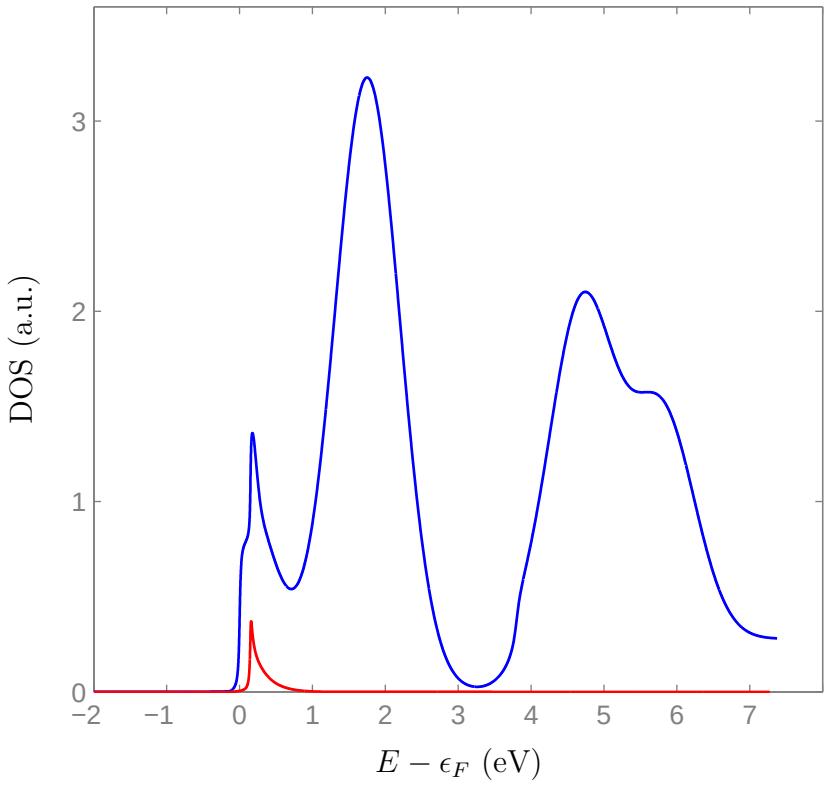

Figure 4.1: Based on the discussion in Section 3.3.2, we construct the valence bands of $1T$-TaS_2. The blue curve mimics the joint DOS of the calculated Ta-$5d$ bands (see Figure 3.9) and the continuum beginning at 3.8 eV above the Fermi energy [4]. According to the band structure, the low-lying $5d_{z^2}$ band is partially filled by one electron. The underlying area of the DOS therefore corresponds to a total of 4.5 empty (unoccupied) states per Ta atom. The red curve represents the degree of the CMW modulation. It is obtained by multiplying the DOS of the $5d_{z^2}$ band with the modulation parameter Eq (3.20). The result is then scaled to make sure that the underlying area is equal to 1/13 empty states per Ta atom.

lattice. Hence only if any of the three vectors $\mathbf{Q}$, $\mathbf{Q}^+$ and $\mathbf{Q}^-$ coincides with a reciprocal lattice vector $\mathbf{G}$ will the cross-section given in Eq (4.8) be non-vanishing. In other words, scattering takes place around

$$\boxed{\mathbf{Q} = \mathbf{G}} \quad \text{and} \quad \boxed{\mathbf{Q} = \mathbf{G} \mp \mathbf{k}_{\text{CDW}}} \tag{4.9}$$

For x-ray diffraction, these are the so-called Laue conditions for the observation of the Bragg peaks and of the CDW satellite peaks, respectively. We will then refer to the corresponding lattice sums as the Bragg reflections and the CDW satellite reflections.

Adding the LDW

Still more interesting is the situation when we have both the CMW and the LDW into the lattice. For the lattice sums appearing in Eq (4.8), we then substitute $\mathbf{R}$ with a distorted lattice position $\mathbf{R} + \mathbf{u}_0 \sin(\mathbf{k}_{\text{CDW}} \cdot \mathbf{R})$ and re-calculate the cross-section. Using the approximation[2]

$$\begin{aligned}
&\sum_{\mathbf{R}} e^{i\mathbf{X}\cdot\left(\,\mathbf{R}+\mathbf{u}_0\sin(\mathbf{k}_{\text{CDW}}\cdot\mathbf{R})-\mathbf{R}_0-\mathbf{u}_0\sin(\mathbf{k}_{\text{CDW}}\cdot\mathbf{R}_0)\,\right)} \\
&\quad\approx |J_0|^2 \sum_{\mathbf{R}} e^{i\mathbf{X}\cdot(\mathbf{R}-\mathbf{R}_0)} + |J_1|^2 \sum_{\mathbf{R}} e^{i\mathbf{X}^+\cdot(\mathbf{R}-\mathbf{R}_0)} + |J_1|^2 \sum_{\mathbf{R}} e^{i\mathbf{X}^-\cdot(\mathbf{R}-\mathbf{R}_0)}
\end{aligned} \tag{4.10}$$

we find the LDW effectively causes the lattice sums to split into higher-order structures. This is true for both the Bragg reflection and the CDW satellite reflections. In Eq (4.10), $\mathbf{X}^\pm = \mathbf{X} \pm \mathbf{k}_{\text{CDW}}$, where $\mathbf{X} = \mathbf{Q}, \mathbf{Q}^\pm$; J_i is the ith-order Bessel function evaluated at $\mathbf{X}\cdot\mathbf{u}_0$. In short, the cross-section now corresponds to non-vanishing reflections at $\mathbf{Q} = \mathbf{G}$, $\mathbf{G} \mp \mathbf{k}_{\text{CDW}}$, and $\mathbf{G} \mp 2\mathbf{k}_{\text{CDW}}$. Consult the illustration[3] given

[2]This result is easily be verified using the Jacobi-Anger generating function for Bessel function $J_n(z)$:

$$e^{iz\sin\theta} = \sum_{n=-\infty}^{\infty} e^{i\cdot n\theta} J_n(z)$$

[3]Compared to Eq (4.8), it is evident that the "secondary" CDW satellites at $\mathbf{G} \mp 2\mathbf{k}_{\text{CDW}}$

in Figure 4.2.

With regards to the structural study of the CMW, the "primary" satellite-reflections $\mathbf{G} \mp \mathbf{k}_{\mathrm{CDW}}$ readily distinguish themselves from the others. For the cross-section of these reflections, we find

$$\Big(\frac{d\sigma}{d\Omega}\Big)^{\mathbf{Q}\sim\mathbf{G}^{\mp}}_{\mathrm{CDW},\alpha\beta} = Nr_0^2\Big(|f_{\alpha\beta}|^2|J_1(\mathbf{Q}\cdot\mathbf{u}_0)|^2 + \frac{|\tilde{f}_{\alpha\beta}|^2}{4}|J_0(\mathbf{Q}^{\pm}\cdot\mathbf{u}_0)|^2\Big)\sum_{\mathbf{R}} e^{i\mathbf{Q}^{\pm}\cdot\mathbf{R}} \quad (4.11)$$

In the parenthesis, the $|J_1|^2$ term corresponds to the satellite structure derived from the Bragg reflection $\mathbf{G}$. One can therefore attribute this contribution to the superstructure of the LDW. Representing the LDW amplitude, $\mathbf{u}_0$ is small by nature. Numerically, $|J_1|^2 \ll |J_0|^2$. Hence the LDW contribution is subject to a more serious reduction than the CMW contribution. Apart from the Bessel functions, the cross-section is basically a sum of scattering from the LDW and from the CMW. On this account, scattering turns out to be additive for these satellites[4].

4.2 Kinematic Theory of X-ray Diffraction

Although we have used a monoatomic lattice to derive the cross-section, the result can easily be generalized for $1T$-TaS_2. As suggested in Eq (4.11), scattering due to the LDW (CMW) is a product of the $|f_{\alpha\beta}|^2$ ($|\tilde{f}_{\alpha\beta}|^2$), $|J_1|^2$ ($|J_0|^2$) and the lattice sum. If there is more than one atom in each unit cell, we would rather use the

arise as a combined effect of the co-existing superstructures of the CMW and of the LDW. Furthermore, we note that the satellite series ends at $\mathbf{G} \mp 2\mathbf{k}_{\mathrm{CDW}}$ is due to our assumption of the sinusoidal CMW and LDW. In fact, one may tend to guess that certain satellites have their intensities depend solely on the CMW effect (for example, Ref. [6]). This is again an artifact for the same reason. In experiments, one can easily observe high order satellites caused by the LDW[3]. As the CMW and the LDW correspond to similar structures, it is unlikely that the CMW effect can exclusively stand out in the reciprocal space.

[4]This statement holds true even when the CMW and the LDW show different spatial structures. See Appendix B.

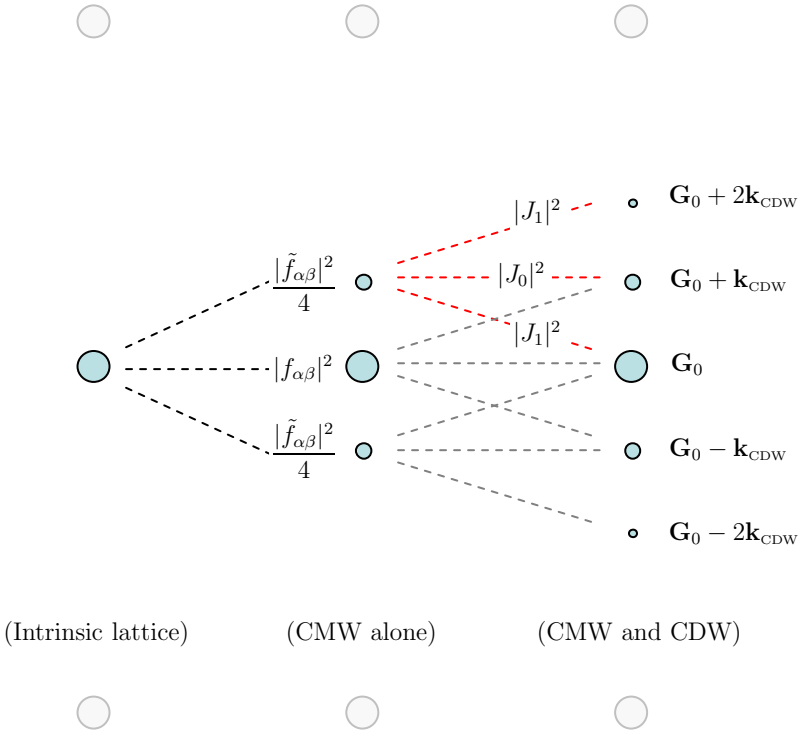

Figure 4.2: Schematic of the creation of the CDW satellites. Reflections split in accordance with the CDW wavevector $\mathbf{k}_{\mathrm{CDW}}$. As neither the CMW nor the LDW is assumed to contain any high-order harmonics, two satellites will appear around every reflection each time a superstructure is introduced. Because the CMW is a modulation of the atomic scattering form factor, satellites are characterized by the functions $\tilde{f}_{\alpha\beta}$ v.s. $f_{\alpha\beta}$. In contrast, the LDW is a real structural change. This is manifested by the satellites' dependence on the displacement $\mathbf{u}_0$ via the two Bessel functions J_1 and J_0.

structure factor

$$F_{\alpha\beta}(\mathbf{Q},\omega) = \sum_j f_{j,\alpha\beta}(\mathbf{Q},\omega)\cdot e^{i\mathbf{Q}\cdot\mathbf{d}_j} \tag{4.12}$$

in the place of the atomic form factor[5]. In this definition, the summation runs over all the atoms in the unit cell, and $\mathbf{d}_j$ is the position of the jth atom inside the unit cell. It follows that the LDW component of the cross-section

$$\Big(\frac{d\sigma}{d\Omega}\Big)^{\mathbf{Q}\sim\mathbf{G}^{\mp}}_{\mathrm{LDW},\alpha\beta} = N r_0^2\,|F_{\alpha\beta}|^2 |J_1(\mathbf{Q}\cdot\mathbf{u}_0)|^2 \sum_{\mathbf{R}} e^{i\mathbf{Q}^{\pm}\cdot\mathbf{R}} \tag{4.13}$$

Similarly, we define a *modulated* structure factor made of $\tilde{f}_{\alpha\beta}$

$$\tilde{F}_{\alpha\beta}(\mathbf{Q},\omega) = \sum_j \tilde{f}_{j,\alpha\beta}(\mathbf{Q},\omega)\cdot e^{i\mathbf{Q}\cdot\mathbf{d}_j} \tag{4.14}$$

and write the CMW component of the cross-section

$$\Big(\frac{d\sigma}{d\Omega}\Big)^{\mathbf{Q}\sim\mathbf{G}^{\mp}}_{\mathrm{CMW},\alpha\beta} = \frac{1}{4}\, N r_0^2\,|\tilde{F}_{\alpha\beta}|^2 |J_0(\mathbf{Q}^{\pm}\cdot\mathbf{u}_0)|^2 \sum_{\mathbf{R}} e^{i\mathbf{Q}^{\pm}\cdot\mathbf{R}} \tag{4.15}$$

Measured intensity of the satellite peaks

The theory of kinematic diffraction can then be used to describe the intensity of x-ray scattering associated with the cross-sections [3]. Given Eq (4.13), we find the LDW component of the intensity

$$I^{\mathbf{G}^{\mp}}_{\mathrm{LDW},\alpha\beta} = \Big(\frac{1}{2\mu}\Big)|J_1(\mathbf{G}^{\mp}\cdot\mathbf{u}_0)|^2 \frac{r_0^2\lambda^3|F_{\alpha\beta}|^2}{v_c^2\sin 2\theta}\, I_0 \tag{4.16}$$

where I_0 is the intensity of the incident beam, v_c is the volume of the unit cell, and θ is the diffraction angle. Similarly we determine the CMW component

$$I^{\mathbf{G}^{\mp}}_{\mathrm{CMW},\alpha\beta} = \Big(\frac{1}{8\mu}\Big)|J_0(\mathbf{G}\cdot\mathbf{u}_0)|^2 \frac{r_0^2\lambda^3|\tilde{F}_{\alpha\beta}|^2}{v_c^2\sin 2\theta}\, I_0 \tag{4.17}$$

[5]One can assume that the internal structure of the unit cells does not change when the lattice is distorted. In the LDW, unit cells are displaced as rigid objects.

When these two components are added together, the result describes the measured intensity of the CDW satellite peaks at $\mathbf{G} \mp \mathbf{k}_{\mathrm{CDW}}$. In these expressions, μ is the absorption coefficient, which can be related to the structure factor via

$$\boxed{\mu(\omega) = -4\pi\Big(\frac{r_0 c}{v_c \omega}\Big)\,\mathrm{Im}\big[F_{\alpha\alpha}(\mathbf{Q},\omega)\big]_{\mathbf{Q}=0}} \tag{4.18}$$

Through μ, kinematic diffraction actually places more emphasis on the imaginary part of the structure factor than the real part. Correspondingly, the intensities will show different frequency behavior from the cross-sections.

Intensity of the CDW satellite peaks of $1T$-TaS_2

As an immediate application of the theory, let us determine the intensity of the primary CDW satellite peaks when x-ray is scattered off by $1T$-TaS_2. Recall the construction of the LDW in Section 3.3.1. The distorted lattice has actually been determined for the CDW. The corresponding supercell can then be used in Eq (4.12) to calculate $F_{\alpha\beta}$. For the CMW, whose structure has only been described by theorists[6], let us assume a charge density distribution in accordance with the model given in Section 3.3.2 and create a hypothetical $\tilde{F}_{\alpha\beta}$. Since we now calculate the intensity with the supercell, we no long need those Bessel functions[7]. Collecting these results together means the intensity of the satellites is

$$\boxed{I^{\mathbf{G}^{\mp}}_{\mathrm{TaS_2},\alpha\beta} = \Big(\frac{1}{2\mu}\Big)\frac{r_0^2\lambda^3 I_0}{v_c^2 \sin 2\theta}\Big(|F_{\alpha\beta}|^2 + \frac{1}{4}|\tilde{F}_{\alpha\beta}|^2\Big)} \tag{4.19}$$

Again the contributions from the LDW and from the CMW are explicitly separated. Whenever this equation is evaluated, it is important to remember that $F_{\alpha\beta}$, $\tilde{F}_{\alpha\beta}$ and v_c are defined for the CDW supercell.

[6]For example, from the band structure calculations by Wilson [2] and by Bovet [5].

[7]Another way to see this is from the understanding that the Bessel function appearing in Eq (4.16) is the lowest order approximation of the LDW. Since we have used the true coordinates and get the superstructure, we can safely drop the Bessel function. For the CMW, because $\mathbf{u}_0$ is very small, $J_0 \approx 1$ anyway.

We remark that kinematic diffraction can be used to describe the CDW satellite peaks because the satellites are intrinsically weak peaks. Moreover, the finite CDW correlation implies that the CDW has enough disorder to prevent secondary scattering from occurring. However, neither of these conditions will hold for the Bragg peaks. As we will describe in the next section, we must take a very different approach to determining the intensities of Bragg peaks.

4.3 Dynamical Theory of X-ray Diffraction

Indeed, the CDW affects the Bragg peaks. The question is how much. As far as the cross-section is concerned, the Bragg reflection is a sum of two separate contributions, namely from the LDW

$$\Big(\frac{d\sigma}{d\Omega}\Big)^{\mathbf{Q}\sim\mathbf{G}}_{\mathrm{LDW},\alpha\beta} = Nr_0^2\,|F_{\alpha\beta}|^2|J_0(\mathbf{Q}\cdot\mathbf{u}_0)|^2\sum_{\mathbf{R}} e^{i\mathbf{Q}\cdot\mathbf{R}} \tag{4.20}$$

as well as from the CMW

$$\Big(\frac{d\sigma}{d\Omega}\Big)^{\mathbf{Q}\sim\mathbf{G}}_{\mathrm{CMW},\alpha\beta} = Nr_0^2\,|\tilde{F}_{\alpha\beta}|^2\Big(\frac{|J_1(\mathbf{Q}^+\cdot\mathbf{u}_0)|^2}{4}+\frac{|J_1(\mathbf{Q}^-\cdot\mathbf{u}_0)|^2}{4}\Big)\sum_{\mathbf{R}} e^{i\mathbf{Q}\cdot\mathbf{R}} \tag{4.21}$$

Taking advantage of the smallness of $\mathbf{u}_0$, we make use of the two approximations $J_0 \approx 1$ and $J_1 \approx (\mathbf{Q}^{\pm}\cdot\mathbf{u}_0)/2 \ll 1$. Hence it is legitimate to neglect the CDW effect at Bragg peaks.

Compared with CDW satellite peaks, Bragg peaks are really strong. In experiments, one readily looks for Bragg peaks with big structure factors. Whenever there is a strong reflection, certain amount of x-ray must be removed from the forward direction. In turn the intensity of the incident field decreases. In Figure 4.3, we illustrate the situation corresponding to reflection from the jth atomic layer. Given T_j as the amplitude of the incident field, we are concerned with the amplitudes of the reflection S_j and of the transmission T_{j+1}. From Fresnel diffraction [8],

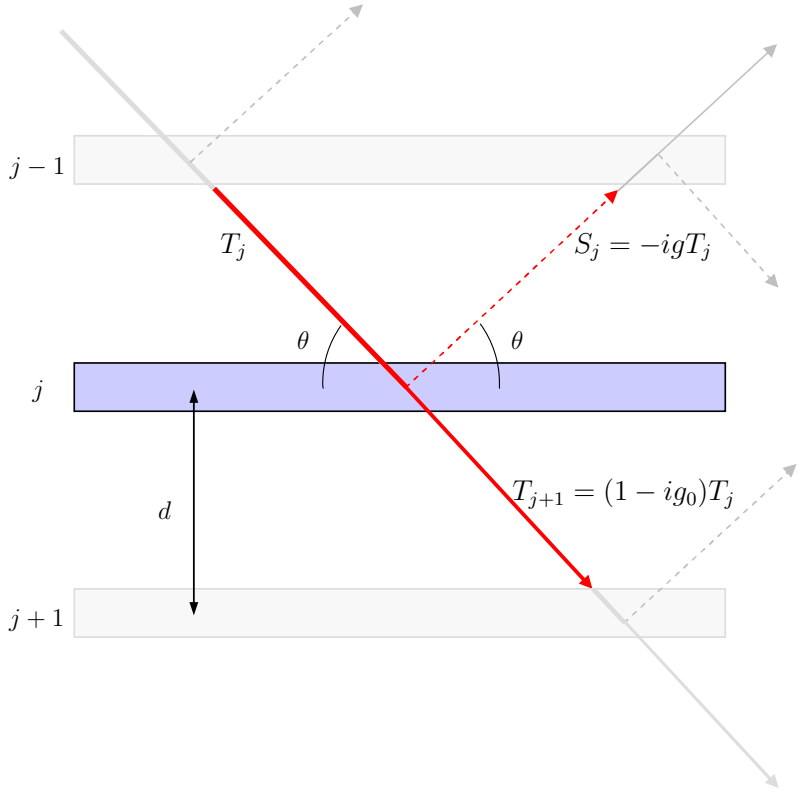

Figure 4.3: Schematic of partial transmission (solid line) and partial reflection (broken line) due to a single atomic layer j inside a cyrstal. T_j: the inident field; T_{j+1}: the transmission field; S_j: the reflection field. The propagation of each field can be understood according to the theory of Fresnel diffraction. On the upper right corner, we indicate the occrance of secondary scattering.

one can easily derive

$$S_j = -igT_j \tag{4.22}$$

$$T_{j+1} = (1 - ig_0)T_j \tag{4.23}$$

In these expressions, g is directly related to the structure factor via

$$g = \frac{\lambda r_0 d}{v_c \sin\theta} F_{\alpha\beta} \tag{4.24}$$

and is therefore a function of $\mathbf{Q}$ as well as of ω. Accordingly we shall introduce a useful constant g_0, which is defined to be g's value in the forward direction. Also shown in the Figure is the secondary reflection taking place at where S_j hits layer $j-1$. This "down-going" reflection will naturally become part of T_j, and the same story will be repeated for indefinite times. Nevertheless, there will be some transmission of S_j that succeeds in going all the way to the top layer. Collecting all such transmissions emerging from the surface, we find the amplitude of the diffracted field S_0. This amplitude should then be squared, and we obtain the intensity of the diffraction peak which one will hopefully measure in experiments.

Because of secondary scattering, there is strong interference between the transmission fields and the reflection fields. To determine these fields, one needs to establish a set of coupled equations and solve T_j and S_j. Instead of treating the problem like a math quiz, however, let us describe the fields using what we have learned in physics. For simplicity, we will assume there is no x-ray absorption in the crystal. Suppose we sit at a Bragg peak position. The strong reflection means the incident field experiences a substantial reduction along the traveling direction. In other words, there is a strong extinction of the incident field. The fact that x-ray can not reach the deep portion of the crystal implies a total reflection at the surface. $S_0 = T_0$: we have a 100% reflectivity. In fact, $S_j = T_j$ for all j, which can mostly easily be seen by the reversibility of light. Hence we conclude that at

Bragg peaks the transmission fields and reflection fields must combine with equal amplitudes and will create standing waves in the crystal. The amplitude of the standing waves decreases exponentially with increasing depth. Let us denote the corresponding characteristic length of the decay as η — the so-called extinction depth.

We can then move off the perfect Bragg condition. As soon as this happen, the phase difference between T_j and T_{J+1} deviates from 180°. Extinction weakens. This effect will be compensated, however, as more layers become involved and maintain the total reflection S_0 equal to T_0. Hence there is a finite range of the incident angle, in which we can have perfect reflectivity. Eventually η hits the infinity. At this point, there is no appreciable decay in the incident field. We recover the situation of kinematic diffraction. Going any further will simply cause the reflectivity to drop like falling off from a peak in kinematic diffraction, as the entire crystal has been used to create the reflection.

Let us look at how secondary scattering is considered in the standard treatment of x-ray diffraction by a perfect crystal. In the Darwin-Prins theory of dynamical x-ray diffraction [3], angular deviation from the center of a Bragg peak is measured by

$$x_c = m\pi\frac{\zeta}{g} - \frac{g_0}{g} \tag{4.25}$$

where m is the order of the Bragg peak, and $\zeta \equiv \mathbf{\Delta G}/\mathbf{G}$ is the relative deviation from the reciprocal point $\mathbf{G}$. It is noticed that the Bragg peak has its center appear at $\zeta_0 \equiv g_0/m\pi$. This results from the fact that inside the crystal the effective wavelength of x-ray has been changed. Using this parameter one can

write the *amplitude* reflectivity

$$r(x_c) = \frac{S_0}{T_0} = \begin{cases} \left(x_c + \sqrt{x_c^2 - 1}\right)^{-1} & \text{for } \mathrm{Re}[x_c] \geq 1 \\ \left(x_c + i\sqrt{1 - x_c^2}\right)^{-1} & \text{for } |\mathrm{Re}[x_c]| \leq 1 \\ \left(x_c - \sqrt{x_c^2 - 1}\right)^{-1} & \text{for } \mathrm{Re}[x_c] \leq -1 \end{cases} \tag{4.26}$$

By calculating the squared norm of this function, one will obtain the intensity reflectivity. Once plotted, the function $|r(x_c)|^2$ vs $\mathrm{Re}[x_c]$ is known as the Darwin reflectivity curve. From Eq (4.26), it is noticed that if x_c is a real number, the Darwin reflectivity curve corresponds to a symmetric function about $x_c = 0$. To the extend that one can completely ignore x-ray absorption, the Darwin reflectivity curve represents a universal characteristic for all Bragg peaks. As Figure 4.4 shows, there is this region $-1 \leq \mathrm{Re}[x_c] \leq 1$ in which we have a 100% reflectivity. In units of x_c, this reflectivity "plateau" corresponds to a constant width equal to 2. Beyond this region, reflectivity decreases rather quickly. Far away from the plateau, the Darwin reflectivity curve looks like $x_c^{-2} \sim |F_{\alpha\beta}|^2$. Diffraction is then characterized by kinematic diffraction.

The interesting characteristic of the Darwin reflectivity curve should be considered along with other two very important physical quantities. For the reflectivity plateau shown in Figure 4.4, the Darwin-Prins theory gives[8]

$$\omega_{\mathrm{D}}^{\mathrm{total}} = \frac{2}{m\pi} \frac{\tan\theta}{\mathrm{Re}[g^{-1}]} \tag{4.27}$$

as the corresponding angular width. Known as the *angular* Darwin width, this quantity defines the angular acceptance associated with a Bragg peak for a given energy. For the extinction depth, we find

$$\eta = \frac{d}{2\mathrm{Re}[g\sqrt{1 - x_c^2}]} \tag{4.28}$$

[8]Note we have carefully formulated the expression so it can handle complex x_c. This is crucial for structure factors that contain large imaginary components.

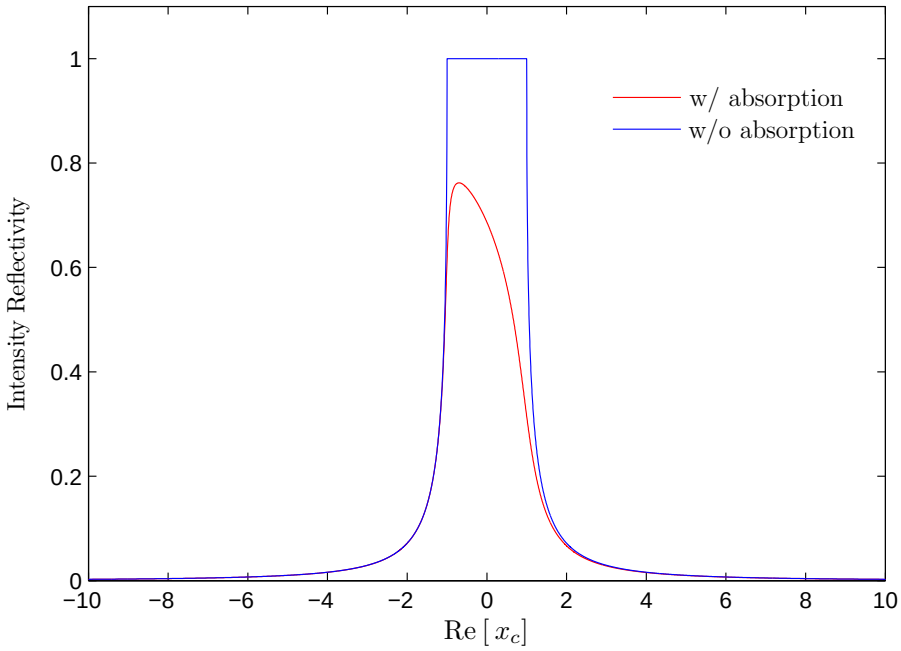

Figure 4.4: The Darwin reflectivity curve of the (002) Bragg diffraction peak of $1\,T$-TaS_2 under two very different situations. At very high energies, it is legitimate to ignore x-ray absorption. The curve will then show a flat top of 100%-reflectivity in $-1 \leq \mathrm{Re}[x_c] \leq 1$. (Indeed, x_c is a real number if there is no absorption.) Outside this region, the reflectivity falls like $x_c^{-2} \sim |F_{\alpha\beta}|^2$, which can be related to the result of kinematic diffraction mentioned in Eq (4.16). At 9.841 KeV (close to the Ta-L_3 edge), there exists considerable x-ray absorption. As expected the reflectivity will be reduced. The curve becomes asymmetric.

In our description of dynamical diffraction, we argued that the extinction depth must diverge at the edges of the plateau of the Darwin reflectivity curve. Such a behavior can clearly be checked if we make $x_c \rightarrow \pm 1$ in Eq (4.28), assuming no x-ray absorption.

If absorption is not negligible, both g and g_0 (and hence x_c) become complex numbers. The Darwin reflectivity curve is no longer symmetric about $x_c = 0$. The intensity of a Bragg peak varies as a function of the diffraction angle. In experiments, it is therefore very important to specify how the intensity is measured.

Without worrying about the issue of a uniform cross-section for the incident x-ray beam, we will call the integration

$$I^{\mathbf{G}}_{\mathrm{TaS_2}} = \omega^{\mathrm{total}}_{\mathrm{D}} \int |r(x_c)|^2 \, d(\mathrm{Re}[x_c]) \tag{4.29}$$

the *integrated* intensity[9] of Bragg peaks. As it will be shown in Chapter 6, in our diffraction experiment we succeeded in measuring the integrated intensities for several Bragg peaks. As far as the measured intensity is concerned, the dynamic theory is very different from the kinematic theory in how the structure factor $F_{\alpha\beta}$ is incorporated in each theory. In contrast to the kinematic theory, the measured intensity in the dynamic theory is not proportional to $|F_{\alpha\beta}|^2$. Knowing that the CDW has only a very limited effect on the Bragg peaks, we once attempted to approximate the $|F_{\alpha\beta}|^2$ term of the CDW intensity (see Eq (4.19)) by the intensity of the nearby Bragg peaks. Due to the dynamic theory, it is now clear why that idea did not work. Experimentally we have demonstrated that the CDW satellites and the Bragg peaks require the different theories to account for their distinct energy behaviors in x-ray diffraction. We will return to this discussion in Chapter 6 when we discuss the experimental findings.

[9]Rigorously speaking, the integrated intensity is the convolution between the Darwin reflectivity curve and the spatial profile of the cross-section of the incident x-ray beam. Here we assume that the Darwin width is small compare to the angular divergence of the incident x-ray beam.

BIBLIOGRAPHY

[1] Jens Als-Nielsen and Des McMorrow. *Elements of modern X-ray physics*. John Wiley and Sons Ltd, New York, 2001.

[2] J. A. Wilson, F.J. Di Salvo, and S. Mahajan. Charge-density waves and superlattices in the metallic layered transition metal dichalcogenides. *Advances in Physics*, 24(2):117–201, 1975. Relating CDW formation to the band structure.

[3] Albert Spijkerman, Jan L. de Boer, Auke Meetsma, Gerrit A. Wiegers, and Sander van Smaalen. X-ray crystal-structure refinement of the nearly commensurate phase of $1T$-TaS_2 in $(3+2)$-dimensional superspace. *Phys. Rev. B*, 56(21):13757–13767, Dec 1997.

[4] Z. Y. Wu, G. Ouvrard, P. Moreau, and C. R. Natoli. Interpretation of preedge features in the Ti and S K-edge x-ray-absorption near-edge spectrain the layered disulfides TiS_2 and TaS_2. *Phys. Rev. B*, 55(15):9508–9513, Apr 1997.

[5] M. Bovet, S. van Smaalen, H. Berger, R. Gaal, L. Forró, L. Schlapbach, and P. Aebi. Interplane coupling in the quasi-two-dimensional $1T$-TaS_2. *Phys. Rev. B*, 67(12):125105, Mar 2003.

[6] P. Abbamonte. Charge modulations versus strain waves in resonant x-ray scattering. *Phys. Rev. B*, 74:195113–195118, Apr 2006.

[7] Kristin Lee Ringland. *The Structure and Kinetics of Charge Density Waves*. PhD thesis, Cornell University, January 2000. Section 4.3.

[8] B. E. Warren. *X-ray Diffraction*. Dover Publication, Inc., New York, 1990. Section 14.2.

CHAPTER 5

X-RAY ABSORPTION NEAR-EDGE STRUCTURE

Motivated by the close connection between resonant x-ray scattering and x-ray absorption, we carefully measured the x-ray absorption near-edge structure (XANES) of $1T$-TaS_2 at the Ta-L_3 absorption edge. This chapter is dedicated to giving a thorough discussion about the experiment and the findings. In contrast to the published results [3, 4], our experiment shows that absorption spectra is independent of the x-ray polarization. Moreover, we determine the large core-hole lifetime (4.88eV) is responsible for the loss of the detailed structure in the absorption spectra. From the absorption spectra we derive the dispersion correction of Ta. A model of the atomic form factor tensor is then created based on the total symmetry of the Ta $5d$ states. In Eq (4.19) this means we have all the energy dependence specified for the intensity of the CDW satellites. The prediction of our kinematic theory should then be compared with results of the experimental data presented in Chapter 6.

5.1 Background

X-ray absorption edge spectroscopy concerns electronic transitions from a core atomic state to the unoccupied valence-band states above the Fermi level. In the transition process, the photons are completely destroyed, thereby increasing the x-ray absorbance. An absorption spectrum contains information on the transitions of the core electrons to the unoccupied states. This can most easily be appreciated

by directly looking at the corresponding cross-section

$$\sigma^{ab}(\omega) = \frac{e^2\pi}{\varepsilon_0 m_e^2 \omega c} \sum_{\mathbf{k}} |\langle n_{\mathbf{k}}|\mathbf{p}_s^{\alpha}|s\rangle|^2 \delta(\hbar\omega - \hbar\omega_{\mathbf{k}s}) \tag{5.1}$$

where α is the polarization of x-ray, and the summation runs over all the unoccupied states [1]. Given $|s\rangle$, the symmetry of $|n_{\mathbf{k}}\rangle$ and the relative energy $\hbar\omega_{\mathbf{k}s} = E_{\mathbf{k}} - E_s$ can both be determined from a measured spectrum [2]. Hence x-ray absorption provides a method for studying the electronic structure by probing many aspects of the valence-band states. For the connection with x-ray scattering, one readily notices that the very same matrix element also appears in the dispersion correction of the atomic scattering form factor in Eq (2.28) and (2.29).

Seeing the potential of x-ray absorption spectroscopy, indeed, several groups have previously applied the method to study the valence-band states of CDW materials[3, 4]. For $1T$-TaS_2, such experiments have been realized especially with the Ta-L_3 absorption edge. At this specific edge, transitions initiate from the Ta-$2p_{3/2}$ core state, and, by dipole selection rule, can couple to final s- and d-symmetric states in the valence bands. Furthermore, the continuum of the unbound states for this material lies only about 4 eV above the Fermi level. Hence there will be considerable transitions coupling to the unbound states as well. Given the Ta-$5d$ bands being the most important component in the band structure (See Section 3.3.2), we expect the transitions to be dominated by the dipole transitions between the $2p_{3/2}$ core state and the $5d$ states of Ta. As we will describe in this chapter, these dipole transitions lead to a conspicuous feature called the "white-line" in the x-ray absorption spectra. Using the current model of x-ray absorption spectroscopy, one can understand the white-line arises as a consequence of the high DOS of the Ta-$5d$ bands. Corresponding to the high DOS, excited electrons entering the $5d$ bands experience strong multiple scattering with the local lattice structure. This creates a favorable situation in which the electrons can easily jump back and forth between

the core state and the $5d$ states. Yet the white-line can provide a wealth of information about the local electronic structure of the Ta atoms. Interested readers are referred to Ref. [1] for the theoretical description about the x-ray absorption near-edge structure.

There are two things we would like to learn about $1T$-TaS_2 from the absorption spectrum. As we already mentioned in Section 4.2, the absorption coefficient μ is directly related to the imaginary part of the structure factor of $1T$-TaS_2. Given that there are total three atoms in volume v_c,

$$\mu = \frac{1}{v_c}(\sigma^{ab}_{\mathrm{Ta}} + 2\sigma^{ab}_{\mathrm{S}}) \tag{5.2}$$

as we simply add together the absorption cross-sections of the Ta atom and of the two S atoms appearing in the unit cell. One can then determine the imaginary part of the Ta dispersion correction from the absorption cross-section by[1]

$$f''_{\mathrm{Ta}}(\omega) = -\Big(\frac{\omega}{4\pi r_0 c}\Big)\sigma^{ab}_{\mathrm{Ta}}(\omega) \tag{5.3}$$

provided we can separate the Ta absorbance from the S absorbance in the total absorbance. For the real part of the Ta dispersion correction, we exploit the general relationship

$$f'_{\mathrm{Ta}}(\omega) = -\frac{1}{\pi}\mathcal{P}\int_{-\infty}^{+\infty}\frac{f''_{\mathrm{Ta}}(\omega')}{(\omega'-\omega)}\,d\omega' \tag{5.4}$$

based on the Kramers-Kronig reciprocal transformation between f' and f''. In this respect, we rely on measuring the absorption spectrum to determine the dispersion correction of the atomic form factor.

Yet x-ray absorption has other import as regards its connection with x-ray scattering. We maintain this point by pointing out that both absorption and resonant scattering originate in the same electronic transitions. Given the fact that

[1]According to Eq (4.18), μ reflects only the diagonal components of the tensor of the structure factor. When x-ray absorption is used to determine the dispersion correction, we can therefore drop the polarization indices.

the CDW forms in the Ta-5d_{z^2} band, we are concerned with whether scattering due to this specific band can be distinguished from scattering due to other bands. Same is true for absorption. As clearly shown in Eq (5.1), the absorption spectrum reflects the symmetry as well as the energy of the transitions. By studying x-ray absorption at the Ta-L_3 edge, we gather important knowledge about the transitions to the Ta-5d bands.

5.2 Experiments

Whenever x-ray photon energy is swept across and beyond the absorption edge, the absorbance of the sample varies as a function of x-ray frequency. Besides the absorber, an typical absorption experiment in transmission mode consists of a monochromator, beam slits, and a detector. See Figure 5.1. For a constant-flux incidence on the sample, the detector records the intensities with (I) and without (I_0) the absorber in the x-ray beam. The transmittance T, defined to be the ratio between I and I_0, is related to the absorption coefficient via

$$T \equiv \frac{I}{I_0} = e^{-\mu z} \tag{5.5}$$

assuming a sample of thickness z. When we wrote Eq (5.5), it is assumed that the incident beam consists of a single frequency. In this situation[2], one can exclusively attribute the energy dependence to μ for the transmission.

It must be noticed that the transmittance is a function of both μ and z. Unless we employ other methods to determine the thickness, we do *not* measure μ but the product μz in an absorption experiment. To get around this problem, we introduce

[2]As we will discuss in the following, there will be a finite "thickness" effect if the incidence is not perfectly monochromatic.

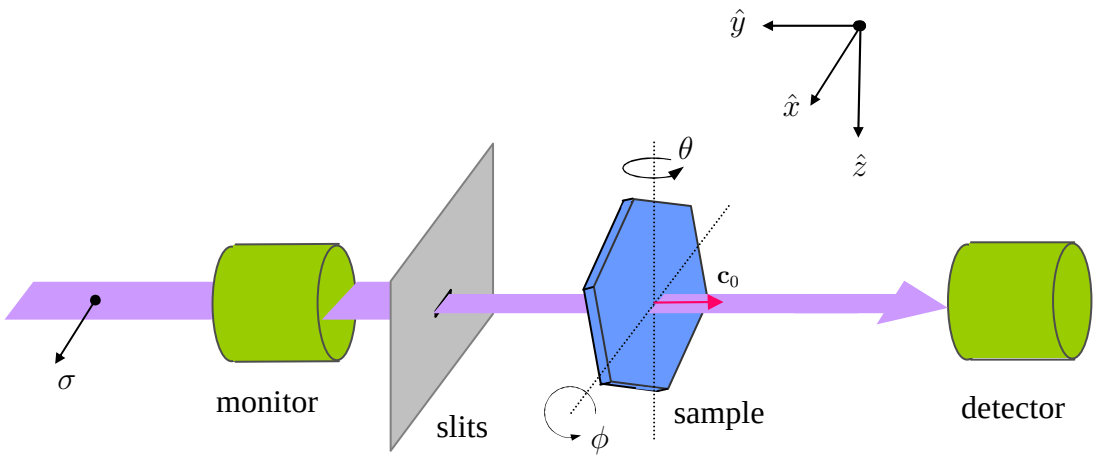

Figure 5.1: A schematic layout of the x-ray absorption experiment. After the monochromator, the horizontally polarized x-ray beam is slitted down so its cross-section becomes smaller than the $1T$-TaS_2 crystal. The sample is mounted on a *horizontal* four-circle diffractometer, whose coordinate system is defined in accordance with the standard definition [3]. With diffractometer angles $\theta = 0°$ and $\chi = 90°$, we can easily change the orientation of the sample with respect to the x-ray polarization. The θ rotation corresponds to a rotation about the vertical axis, while the ϕ rotation gives us a rotation about the x-ray polarization vector.

the relative absorption coefficient

$$\mu_r = \frac{\ln[T(\omega)]}{\ln[T(\omega_r)]} = \frac{\mu(\omega)}{\mu(\omega_r)} \tag{5.6}$$

with ω_r being a chosen reference point. By definition μ_r is not affected by the sample's thickness. This relative absorption coefficient proves to be a very useful concept in describing x-ray absorption.

In Eq (5.1) the matrix element is evaluated for the α-component of the electronic momentum $\mathbf{p}_s$. We expect the cross-section of x-ray absorption to be polarization dependent. We investigated the corresponding symmetry property of μ at the Ta-L_3 edge by measuring the transmission of polarized x-ray through a $1T$-TaS_2 single crystal. The experiment is discussed in the following.

5.2.1 Experimental Details

Sample

Rather than using a powder sample, we used a macroscopic $1T$-TaS_2 single crystal for our x-ray absorption spectrum measurements. We succeeded in making a crystalline sample[3] of $1T$-TaS_2 with a proper thickness of the order of μ^{-1}. The preparation involved gently attaching $1T$-TaS_2 crystals to Kapton tape. By peeling off the bulk crystals, we obtained thin $1T$-TaS_2 layers on the tape. Since samples prepared in this method had very different thicknesses, they must be screened in preliminary x-ray absorption measurements done at the energy 40 eV below the Ta-L_3 edge. Only those with $50\% \sim 70\%$ transmittance were kept. These selected crystals were then carefully examined under an optical microscope to check their crystal quality. We found a uniform single-crystal sample $\sim$ 3 mm in diameter.

[3]The crystal was grown by former group members in 1999 for other experiments. It was $1T$-TaS_2 doped with 4% Nb.

The thickness was estimated to be ~ 25 μm.

Setup

The use of a synchrotron radiation source enabled us to exploit the highly polarized x-ray beam. After the double-bounce Si(111) monochromator, the incident x-ray beam was determined[4] to have a degree of linear polarization $\sim 96\%$ in the horizontal plane. As the schematic layout shows in Figure 5.1, we could easily change the orientation of the $1T$-TaS_2 crystal with respect to the polarization. This maneuverability facilitated the study of the different symmetry of the electronic transitions. We used two independent rotations. In the θ-rotation, we effectively changed the projection of the polarization in the crystal surface. In contrast, in the ϕ-rotation we kept the polarization in the crystal surface and changed only the effective thickness. We used two pairs of slits to define the incident beam. The size was approximately 0.5 mm $\times$ 0.5 mm at the sample position. This cross-section was so small that even at incident angles as high as 60° the incident beam was completely intercepted by the sample. The small cross-section also helped to eliminate the effect of thickness variation that could possibly remain in the $1T$-TaS_2 crystal. The energy resolution of the incident x-ray is ~ 4 eV. For how we estimated/measured the energy resolution and the degree of linear polarization of the incident x-ray, see Appendix .

Measurements

We performed two types of measurements. In an energy scan, we kept the crystal

[4]With the help of a polarimeter, we measured the intensities of the linear components polarized parallel and perpendicular to the horizontal plane in the x-ray beam. The degree of linear polarization is defined to be the ratio between the difference and the sum of the two intensities. The use of the polarimeter will be described in detail in Chapter 6.

in a fixed orientation and changed x-ray energy. The transmission was recorded as a function of energy, from which we determined $\mu_r(\omega)$. We could change the incident angle by varying either θ or ϕ. These scans were used to demonstrate the symmetry property of x-ray absorption.

We could also do angular scans at fixed energy. In such scans, we rotated the crystal and recorded the transmission intensity. We performed several angular scans at different x-ray energies. Serving as confirmation of the results of the energy scans, these angular scans demonstrated some very interesting effects.

5.2.2 Energy scans with different incident angle

Let us start with the results of our energy scans. In the first part of this experiment, we have seven energy scans taken at different θ. Using Eq (5.6) we calculate the relative absorption coefficient μ_r, with the lowest energy point 9.841 KeV being the reference energy.

In Figure 5.2. we plot μ_r as a function of x-ray frequency. As we can clearly see in the Figure, the energy scans correspond to a sudden rise of x-ray absorbance at the Ta-L_3 edge at 9.881 KeV. At the energy 9.921 KeV, μ_r is roughly doubled compared to the reference point below the edge. There is also this conspicuous white-line feature right at the edge between 9.885 KeV and 9.905 KeV. At the peak of the white-line, x-ray absorbance is increased by a amount that is almost two and half times greater than the jump of the absorption edge. While the incident angle has been varied over a rather large range, we do not observe significant changes in the size of the white-line.

We recall our motivation of measuring x-ray absorption at different incident angles is to determine whether the size of the white-line is angle dependent. As a

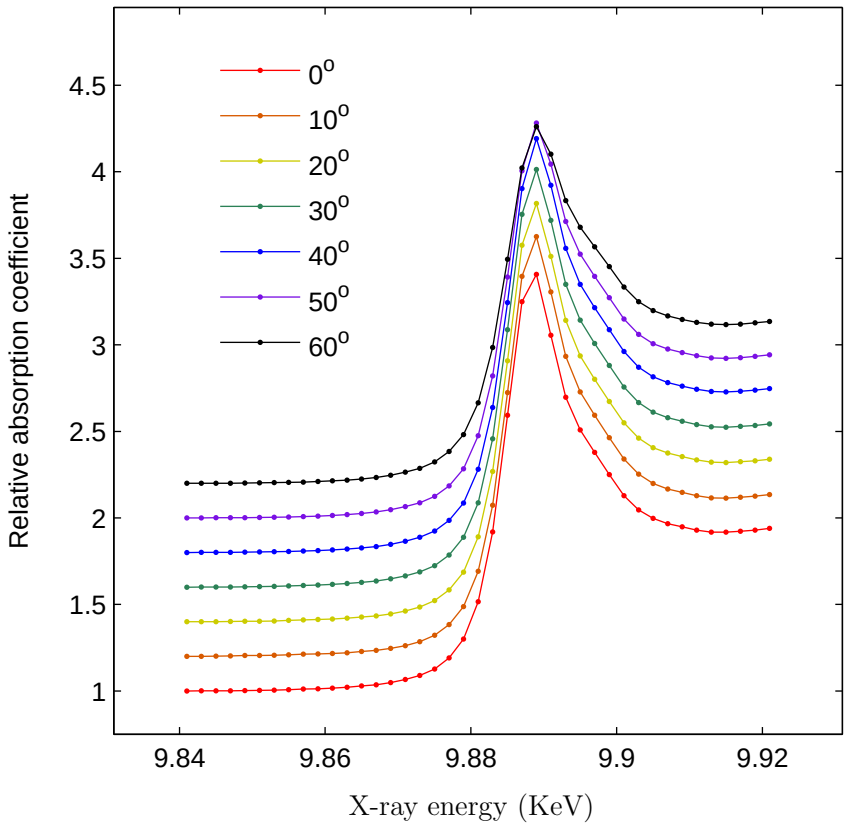

Figure 5.2: The relative absorption coefficient of $1T$-TaS_2, measured at different incident angle θ (with $\theta = 0°$ corresponding to the situation of normal incidence). By varying θ, we change the in-plane component of the x-ray polarization in the crystal surface. Curves are offset for clarity. Lines are drawn to guide the eye.

Table 5.1: The angular dependence of the dipole transition probability P between the initial $2p_{3/2}$ state and the final $5d$ states at the Ta-L_3 edge. Here ϑ is defined to be the angle in the $x-z$ plane between the x-ray polarization and the sample surface. In our θ-rotation, $\vartheta = \theta$ is the incident angle (from the surface normal). The function of the ϑ-dependence is reproduced from Ref. [3]. There are five Ta $5d$ orbitals. After they form the valence bands, $5d_{z^2}$, $5d_{x^2-y^2}$, $5d_{xy}$ will be found in the t_{2g} subband, while $5d_{xz}$ and $5d_{yz}$ will belong to the e_g subband. When it comes to determine the angular dependence of $5d$ bands, the number of the unoccupeid (empty) state serves as a necessary weight for each individual orbital.

Final state	ϑ-dependence	# of empty states	$\frac{P(\vartheta=50^\circ)}{P(\vartheta=0^\circ)}$
$5d_{z^2}$	$\sin^2\vartheta + \frac{1}{3}$	1	278%
$5d_{x^2-y^2}$	$\cos^2\vartheta$	2	41%
$5d_{xy}$	$\cos^2\vartheta$	2	41%
$5d_{xz}$	1	2	1
$5d_{yz}$	$\sin^2\vartheta$	2	∞
All 9 orbitals	$5\frac{1}{3} + \cos^2\vartheta$	9	91%

matter of fact, it was reported in Ref. [3] that at $\theta = 45^\circ$, the size of the white-line would be reduced by about 40% compared with the situation at normal incidence. Our measurements, however, disagree with that result. If we plot the seven curves of μ_r on the top of each other, we see at most a 10% decrease of the size of the white-line at the highest incident angle. There is a fundamental difference between our result and the reported result.

In Table 5.1 we list all five Ta atomic orbitals used in constructing the $5d$ valence bands of $1T$-TaS_2. In x-ray absorption, these orbitals become the final states of the dipole transitions. As the transition rate W_n is given by Fermi's Golden Rule

$$W_n \propto |\langle 5d_n|\mathbf{p}_s^\alpha|2p_{3/2}\rangle|^2 \tag{5.7}$$

Hence the squared norm of the matrix elements gives the transition probability associated with the specific $5d$ orbital $|n\rangle$. Because $\mathbf{p}_s^\alpha$ is the α-component of the electronic momentum, the transition probability is a function of x-ray polarization. In the table this is described by the ϑ-dependence of the transition probability. On account of such polarization dependence, it is argued in Ref. [3] that x-ray absorption *only* sees the $5d_{x^2-y^2}$ and the $5d_{xy}$ orbitals, given that their measured white-line would become greatly suppressed at some large incident angles. We recognize, however, there are the partially-filled $5d_{z^2}$ orbital and the empty $5d_{xz}$ and $5d_{yz}$ orbitals, and all these orbitals will also contribute to x-ray absorption. Indeed, if we take into account the total nine unoccupied states associated with the five $5d$ orbitals, the angular dependence of x-ray absorption become rather marginal ($< 10\%$), consistent with our experimental findings. Hence it makes more physical sense to believe that the transitions from the Ta-$2p_{3/2}$ state to the various Ta-$5d$ states actually overlap and cannot be distinguished in x-ray absorption spectra. X-ray absorption measured at the Ta-L_3 edge is not sensitive to the symmetry of the individual bands. Due to this understanding, we think the effect reported in Ref. [3] is in fact an artifact of thick samples. We shall return to this experimental issue later with more detailed discussions.

Ordinarily we do not think that the ϕ-rotation can have any effect on x-ray absorption. The symmetry of the $1T$-TaS_2 crystal limits the variation of the x-ray absorption coefficient to orientation changes in the θ-rotation[5]. It was, however, reported in a rather recent paper [4] that the size of white-line varied in a ϕ-rotation, which by definition rotated the crystal about the x-ray polarization. In Figure 5.3 we show the results of our measurements. We do *not* observe the angular effect regarding the substantial drop of the size of the white-line at $\phi = 30^\circ$ as reported

[5]This can be seen by observing that $1T$-TaS_2 has threefold symmetry about the $\mathbf{c}_0$ axis. As a consequence, the second-order tensor of x-ray absorption can have no variation about this axis.

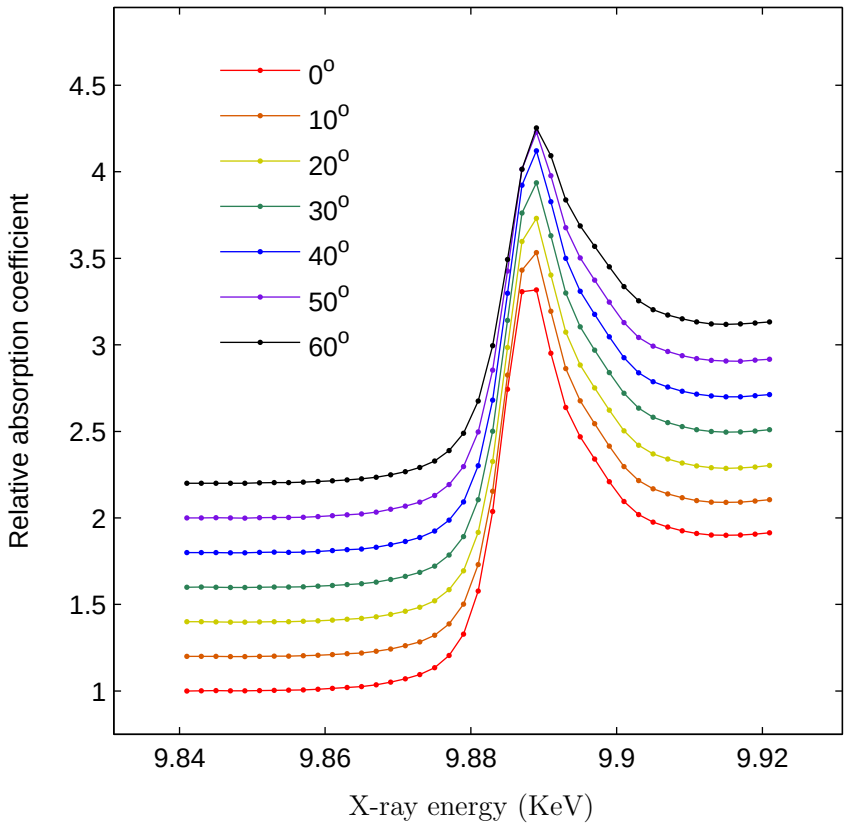

Figure 5.3: The relative absorption coefficient of $1T$-TaS_2, measured at different incident angle ϕ (with $\phi = 0°$ representing the situation of normal incident). Since the ϕ-rotation rotates the crystal about the x-ray polarization, nothing really happens at different ϕ except the effective thickness of the sample is varied as $\cos^{-1}\phi$. Curves are offset for clarity. Lines are drawn to guide the eye.

in the reference.

Important role played by the core-hole lifetime

The fact that the white-line does not show symmetry corresponding to any specific Ta-5d orbital suggests that the white-line is a combined effect of all the orbitals. As a theoretical remark, the transitions from the Ta-$2p_{3/2}$ state to the 5d states are quite broad. The core-hole lifetime [1]

$$\boxed{\Gamma_{\mathrm{Ta}}^{\mathrm{L3}} = 4.88 \text{ eV}} \tag{5.8}$$

which sets the width of the corresponding transitions, is indeed comparable to the full width of the 5d valence bands of 1T-TaS_2. Consequently, all five of the 5d bands are contained in the white-line, and detailed structure of the individual bands is lost. In Figure 5.4, we show that one can model the white-line by convolving the DOS of the 5d valence bands with a 5-eV-wide Lorentzian lineshape.

5.2.3 Angular scans at different x-ray energies

In Figure 5.5 we show the results of our angular scans. In this experiment, transmission was measured as a function of ϕ. Since the pathlength of x-ray changes, the transmission varies as

$$I = I_0 \, e^{-\mu z_0 / \cos\phi} \tag{5.9}$$

assuming the sample of thickness z_0. We measured the transmission at three different energies. It is found the Eq (5.9) rather nicely describes the results of the measurements performed at 9.841 KeV and 9.921 KeV. However, the transmission is generally underestimated in Eq (5.9) in the case of the measurement done at the white-line energy 9.889 KeV. This effect, as it was first discussed in Ref. [7], is

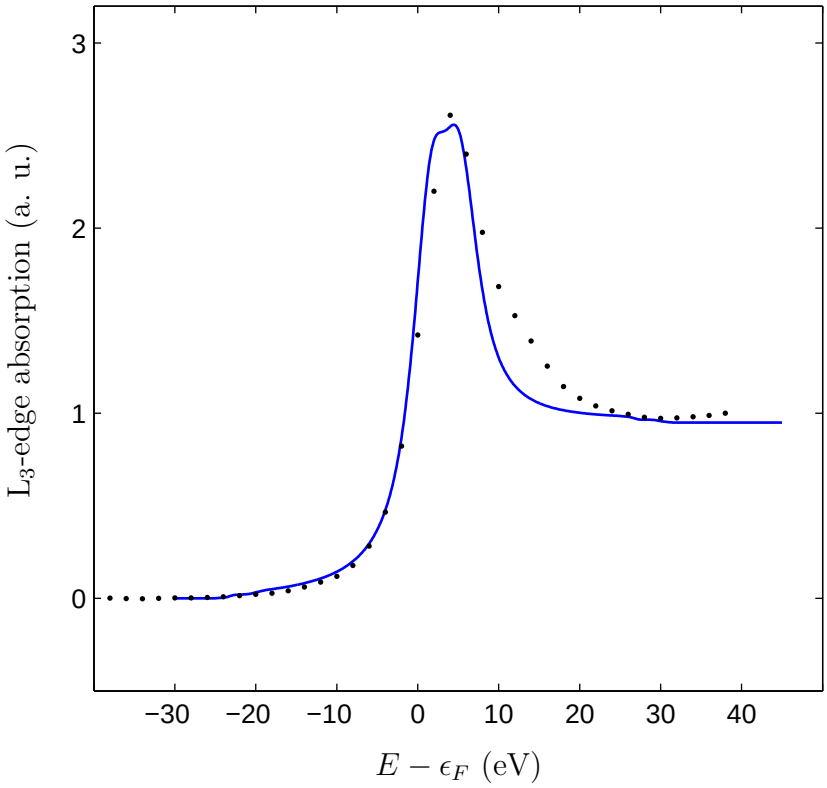

Figure 5.4: By convoluting the DOS of the $5d$ valence bands of $1T$-TaS_2 (see Figure 3.9) with a 5-eV-wide Lorentzian Lineshape we succeed in reproducing the white-line in x-ray absorption. The blue curve is the simulation, whereas the dots are the absorption spectra at the Ta-L_3 edge measured in our energy scans. In the "pre-edge" region, the smooth rise simply reflects the tail of Lorentzian lineshape. It is also found that our simulation fails to capture the second peak centered around 12 eV above the Fermi energy. We attribute this failure to the oversimplified DOS used in the calculation. One may easily improve the simulation by including more DOS such as that of the Ta-$6s$ orbital.

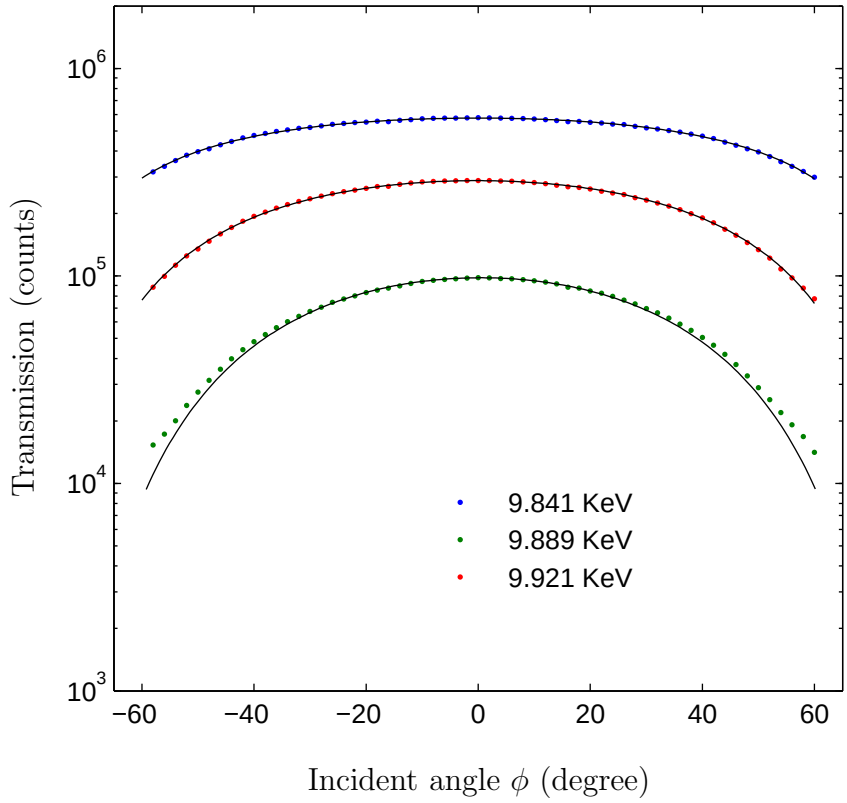

Figure 5.5: X-ray transmission is measured as a function of incident angle from a thin $1T$-TaS_2 crystal of uniform thickness. The solid lines are the best fit curves due to Eq (5.9) for the scans taken at 9.841 KeV and 9.921 KeV. At the white-line energy (9.889 KeV), the same equation fails to describe the measured angular dependence. The so-called x-ray self-absorption occurs as an immediate consequence of our finite energy resolution of the incident x-ray. Imagine a situation where the center of the energy resolution function coincides with the white-line. Given that the white-line has asymmetric shoulders, the low-energy side of the energy resolution function experiences relatively little absorption, resulting in higher transmission than the prediction. Note that the effect becomes more visible with the increasing pathlength at high angles.

a known effect called x-ray *self-absorption*. A brief discussion about the origin of the effect is provided in Figure 5.5.

Look at our angular scan taken at the white-line energy. Because we actually recorded more transmission than what is allowed in Eq (5.9), we underestimate x-ray absorption when we use Eq (5.5) to determine μ. The error grows with increasing ϕ, or equivalently, with increasing sample thickness. We believe when in Ref. [3] it was said they observed a substantial reduction of the white-line, they actually measured the self-absorption effect of x-ray. This illustrates why it was so crucial for us to get a very thin sample when we measured the x-ray absorption spectra in the transmission mode.

5.3 Atomic Form Factor

From the absorption spectra we can determine the Ta dispersion correction near the L_3 edge. As we have shown in Eq (5.2), μ is the sum of the absorption cross-sections of the three atoms in the unit cell. Since f'' is directly connected to σ^{ab} via Eq (5.3), the absorption coefficient is proportional to $(f''_{\mathrm{Ta}} + 2f''_{\mathrm{S}})$. At our reference point 9.841 KeV, it is known that $f''_{\mathrm{Ta}} = 3.99$ and $2f''_{\mathrm{S}} = 0.74$ [2]. Using the sum of these two numbers we scale our relative absorption coefficient μ_r. The result corresponds to the values of $(f''_{\mathrm{Ta}} + 2f''_{\mathrm{S}})$ at the 41 energy points around the Ta-L_3 edge. Once the constant 0.74 (the S contribution) is removed, we obtain f''_{Ta} for Ta in $1T$-TaS_2. Given that this f''_{Ta} is derived from x-ray absorption, one should keep in mind that it corresponds to a physics situation when scattering has the same polarization as the incident wave. As the atomic form factor depend on both the incident polarization and the scattering polarization, we have found the imaginary part of the atomic form factor when the two polarizations are the same. We can

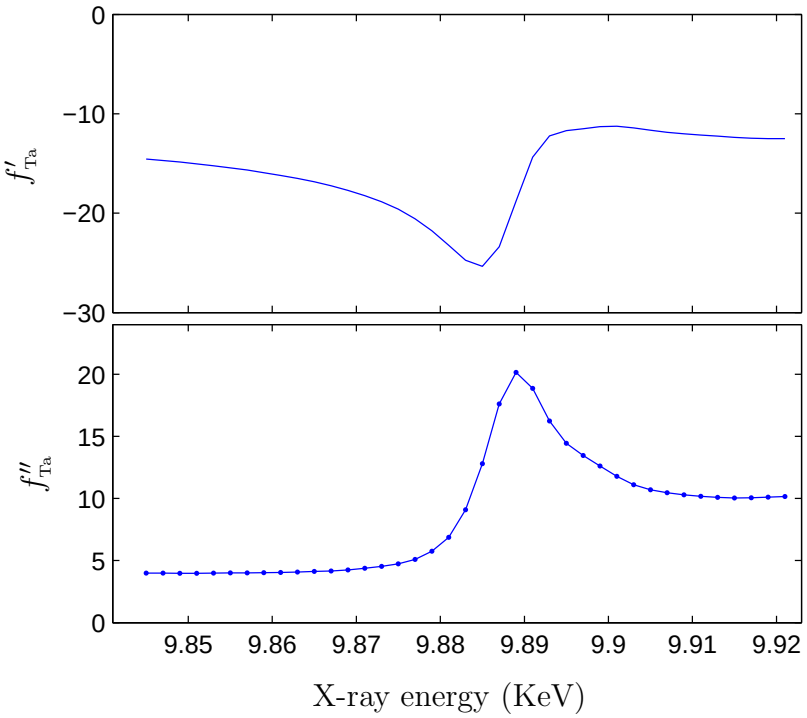

Figure 5.6: The dispersion correction of Ta in $1T$-TaS_2. From the x-ray absorption spectra we first determined the imaginary part f''_{Ta}. We could then calculate the real part f'_{Ta} using the Kramers-Kronig transformation. Because of the large core-hole lifetime, these functions lose detailed information about the band structure. It is also interesting to compare this result with the published data of metallic Ta [8]. There is no visible difference regarding the size and the shape of the white-line.

ignore the 4% doping of Nb in the sample[6].

In order to apply the Kramers-Kronig transformation to calculate f'_{Ta} (Eq (5.4)), we need to know f''_{Ta} as a function of x-ray energy rather than just a few dozens of known points. On the lower-energy side of the L_3 edge, we can model the function using the Ta-M edge absorption. On the higher-energy side, we will extrapolate our measured f''_{Ta} based on the Ta-L edge absorption [10]. As for the computational method, we adopt the technique developed in Ref. [8] to evaluate to the principle value in Eq (5.4). For the Kramers-Kronig transformation to converge to f'_{Ta}, one must integrate over an energy range that is sufficiently large. In our calculation, the integration is performed from 2.7 KeV to 30 KeV. Indirectly, the real part of the dispersion correction of Ta can be determined, assuming the scattered x-ray has the same polarization as the incident x-ray.

In Figure 5.6, we plot the Ta dispersion correction as a function of x-ray energy near the Ta-L_3 edge. As one can clearly see in the Figure, the absorption edge corresponds to an increase of 6 in f''_{Ta}. At the center of the white-line, f''_{Ta} reaches a peak value as large as 20. Meanwhile, f'_{Ta} is negative. At 9.885 KeV, f'_{Ta} corresponds to a minimum of -25. As our discussion on the core-hole lifetime suggests, these extremum features of f''_{Ta} and of f'_{Ta} come from the unoccupied $5d$ bands of the material. It follows that we can scale f''_{Ta} and f'_{Ta} to get the dispersion corrections for the off-diagonal components of the atomic form factor tensor. See the discussion in the following.

Unlike absorption, x-ray scattering involves both photons of the incoming wave and photons of the outgoing wave. In x-ray scattering, the polarization of the scattered (outgoing) wave is independent of the polarization of the incident (incoming) wave. Given that we are dealing with x-ray scattering by crystals, it is

[6]By repeating this calculation with the 4% doping in our sample, we determine that neglecting the Nb leads to an error $\Delta f''_{\mathrm{Ta}} = -0.37$ at the white-line, which is certainly negligible.

rather convenient to specify the polarizations (β and α) with respect to the lattice structure. Let us consider a coordinate system consisting of three mutually perpendicular unit vectors $\hat{x}$, $\hat{y}$ and $\hat{z}$. Knowing that $\mathbf{c}_0$ is the symmetry axis of the crystal structure of $1\,T$-TaS_2, we will make $\hat{z}$ parallel with the $\mathbf{c}_0$-axis and $\hat{x}$ with the $\mathbf{a}_0$-axis. Accordingly, β and α become linear combinations of $\hat{x}$, $\hat{y}$ and $\hat{z}$. The atomic form factor reads

$$f_{\alpha\beta} = \hat{\mathrm{e}}^{\alpha *} \cdot \mathbf{T} \cdot \hat{\mathrm{e}}^{\beta} \tag{5.10}$$

where $\mathbf{T}$ is the atomic form factor tensor, and $\hat{\mathrm{e}}^{\alpha *}$ ($\hat{\mathrm{e}}^{\beta}$) is the unit vector of α (β) written as a row (column) vector. Clearly, different polarizations of the incoming photons and of the outgoing photons in x-ray scattering can be connected by the off-diagonal components of $\mathbf{T}$. Non-vanishing off-diagonal components are seen in various circumstances [2, 12].

From Section 5.2.2 we learned that dipole transitions show different angular dependence when we rotated the sample. The strong dipole transitions at the Ta-L_3 edge correspond to the matrix elements with distinct symmetry with respect to the x-ray polarization (Table 5.1). As we write Eq (5.10) using $\mathbf{T}$, the tensor can then be determined based on the symmetry of the atomic form factor. Returning to the definition of $f_{\alpha\beta}$, the dispersion correction is due to Eq (2.28) and (2.29) and hence is characterized by the matrix elements written in various products. Correspondingly, each tensor component describes x-ray scattering with different polarization dependence. For the off-diagonal elements of the atomic form factor tensor, the matrix elements are evaluated in perpendicular directions. Particularly, given that the system is symmetric about the $\hat{z}$ axis under the dipole approximation, we are most interested in $\mathbf{T}$ about its xz- and its yz- components. We will determine the relative sizes of these components with respect to the diagonal elements such as xx and zz.

Our method is described as follows. The angular dependence of x-ray absorption is determined based on Fermi's Golden Rule (Eq (5.7)). By taking the square root of the angular functions, we get the matrix elements. One should then recall the definition of the incident angle: when $\vartheta = 0°$, the x-ray polarization is in the basal plane. The matrix element is therefore evaluated as if the dipole is in the direction of $\hat{x}$ or $\hat{y}$. When $\vartheta = 90°$, on the other hand, the dipole is pointed along $\hat{z}$. Using this idea, the products of the matrix elements can be determined for every $5d$ orbital. The results must then be summed over all the unoccupied states to get the dispersion correction for Ta. We will, however, take a slightly different route when doing the summation. Instead of adding together the nine unoccupied states, we take away one occupied d_{z^2} orbital from the otherwise empty $5d$ shell of Ta. We find the empty shell corresponds to a tensor equal to $(\frac{20}{3}) \cdot \delta_{ij}$, where $\delta_{ij} = 1$ only if the indices match with each other. On the top of this tensor, the occupied state corresponds to a reduction of 1/3 for the xx- and the yy-components, 4/3 for the zz-components, and 2/3 for the xz- (zx-) and the yz- (zy-) components. Collecting what we have been saying,

$$\mathbf{T}_{\mathrm{Ta}} = f^0_{\mathrm{Ta}}(\mathbf{Q}) \begin{bmatrix} 1 & 0 & 0 \\ 0 & 1 & 0 \\ 0 & 0 & 1 \end{bmatrix} + \frac{f'_{\mathrm{Ta}}(\omega) + i f''_{\mathrm{Ta}}(\omega)}{19} \begin{bmatrix} 19 & 0 & -2 \\ 0 & 19 & -2 \\ -2 & -2 & 16 \end{bmatrix} \tag{5.11}$$

where the tensor of the dispersion correction has been properly scaled so $(f'_{\mathrm{Ta}} + i f''_{\mathrm{Ta}})$ describes the situation of normal incidence. Resulting from the anisotropic nature of the Ta $5d$ states of $1T$-TaS_2, the off-diagonal components of the tensor of the dispersion correction are determined to be approximately ten times smaller than the diagonal components.

X-ray diffraction can measure the atomic form factor at a handful of positions in reciprocal space. When we studied the CDW satellites of $1T$-TaS_2, $\mathbf{Q}$ was found within a region where $f^0_{\mathrm{Ta}} = 53 \sim 65$. Hence in our diffraction experiment, the

measured intensities was dominated by f^0_{Ta} rather than the dispersion correction. Physically, this happens because the Ta-L_3 edge is at such a high energy that 80% of the Ta electrons create only Thomson scattering. Unless one can include polarization analysis in the diffraction experiment, we should not expect scattering will be very sensitive to the off-diagonal elements of the atomic form factor tensor. Meanwhile, since the atomic form factor is a complex function, it is worth emphasizing that its real part is greater than its imaginary part at the energies of our interest, assuming no polarization analysis is used.

As soon as the geometry of the diffraction experiment is decided, one can specify the polarization vectors $\hat{e}^{\alpha}$ and $\hat{e}^{\beta}$. The atomic form factor can then be calculated for the Ta atoms (Eq (5.10)). Finally, we want to ask how much the CDW should change the structure factor at the CDW satellites, given that dispersion correction of Ta, which varies strongly with x-ray energy near the absorption edge.

Implication for x-ray scattering by the CMW

The large core-hole lifetime of the transitions at the Ta-L_3 edge has an important consequence. In the previous chapter, we demonstrated that x-ray scattering by the CMW is characterized by $\tilde{f}_{\alpha\beta}$ — the CMW modulation of the atomic form factor. Although the CMW appears within a few hundred meV above the Fermi level, $\tilde{f}_{\alpha\beta}$ corresponds to transitions that are subject to the large core-hole lifetime broadening. It follows that in x-ray scattering, the CMW can only be found as a rather broad energy feature, regardless of the associated high DOS of the CDW energy gap. Not only $\tilde{f}_{\alpha\beta}$ is inferior in its size (Section 4.1.2), but it can not be resolved at the edge of the energy gap. This suggests that the CMW has only very little effect in x-ray scattering at the Ta-L_3 edge.

BIBLIOGRAPHY

[1] Jan C. J. Bart. *Advances in Catalysis*, volume 34, chapter Near-Edge X-ray Absorption Spectroscopy in Catalysis, pages 203–296. Academic Press, Inc., 1986.

[2] Christian Brouder. Angular dependence of x-ray absorption spectra. *Journal of Physics: Condensed Matter*, 2(3):701–738, 1990.

[3] E. A. Stern, D. E. Sayers, and F. W. Lytle. Orientational dependence of the Ta-L_3 edge absorption in $1T$-TaS_2 as measured by polarized x rays. *Phys. Rev. Lett.*, 37(5):298–301, Aug 1976.

[4] T. K. Kim, V. P. Babenko, and D. I. Kochubey. Study of polarized xanes ta-L_3 spectra of $1T$-TaS_2 monocrystals. *Nuclear Instruments and Methods in Physics Research Section A*, 448(1-2):327–331, June 2000.

[5] Certified Scientific Software. `spec`™: X-ray diffraction software. Internet resource at http://www.certif.com/spec_manual/fourc_4_1.html. Four-Circle Reference.

[6] J. C. Fuggle and J. E. Inglesfield. *Unoccupied electronic states : fundamentals for XANES, EELS, IPS and BIS*, volume 69, chapter Appendix B: Core-Hole Lifetime Broadening, pages 347–351. Springer, Berlin, 1992.

[7] L. G. Parratt, C. F. Hempstead, and E. L. Jossem. "thickness effect" in absorption spectra near absorption edges. *Phys. Rev.*, 105(4):1228–1232, Feb 1957.

[8] P. Dreier, P. Rabe, W. Malzfeldt, and W. Niemann. Anomalous x-ray scattering factors calculated from experimental absorption spectra. *Journal of Physics C: Solid State Physics*, 17:3123–3136, 1984.

[9] Lawrence Berkeley National Laboratory Center for X-Ray Optics. X-ray interactions with matter. Internet resource at http://henke.lbl.gov/optical_constants/asf.html. The Atomic Scattering Factor Files.

[10] W. H. McMaster, N. K. Del Grande, J.H. Mallett, and J.H. Hubbell. Technical Report UCRL-50174-SEC2-R1, Lawrence Livermore Laboratory Report No, 1969.

[11] M. Blume. *Resonant Anomalous X-ray Scattering: Theory and Applications*, pages 495–512. North-Holland, 1994.

[12] M. Blume and Doon Gibbs. Polarization dependence of magnetic x-ray scattering. *Phys. Rev. B*, 37(4):1779–1789, Feb 1988.

CHAPTER 6

RESONANT X-RAY DIFFRACTION

In our resonant x-ray diffraction experiments we measured the intensities of the CDW satellites as function of energy. For comparison, we conducted similar measurements at the Bragg peak positions as well. By looking at diffraction from the CDW at very different temperatures, we demonstrated that resonant x-ray scattering is not sensitive to the CMW when performed at the Ta-L_3 edge. Our experimental results prove that the kinematic theory can be used to describe the energy dependence of the CDW satellite, whereas the energy dependence of the Bragg reflections needs to be understood using the dynamic theory. In both cases, scattering is subject to the same large core-hole lifetime as measured in the absorption spectra. Consequently, the energy behavior of the diffraction intensities is predominated by the LDW only. Resonant x-ray diffraction conducted at the Ta-L_3 edge turns out to be a suppression of the diffraction intensities rather than an enhancement. We pointed out this is due to the large Thomson scattering component of the Ta atomic form factor. Polarization analysis is useful in reducing Thomson scattering. However, as we have learned in our experiment, an ultra pure polarization is required if one wants to study exclusively the effect of resonant x-ray scattering.

6.1 Experimental Conditions

Our diffraction experiment was conducted at the Cornell High Energy Synchrotron Source at Cornell University in many different runs. Before we present the experimental data, let us talk about the general aspects of the experiments. We will

discuss sample preparation, beam properties and the diffraction geometry.

6.1.1 Sample

In our experiment we used a single crystal of $1T$-TaS_2. The mosaic was measured to be $\sim 0.04^\circ$ based on the widths of several Bragg peaks. The crystal was grown in 1999 and contains 4% Nb[1]. Clearly showing the characteristic hexagonal shape, the crystal has a diameter $\sim$ 3 mm, and the thickness is approximately 500 μm. Since this thickness is large compared to the absorption length $\sim$ 17 μm (below the edge), our crystal is a bulk. We measured x-ray diffraction in a reflection mode.

In order to study the difference between the N-C phase and the C phase of the CDW of $1T$-TaS_2, we needed to change the temperature of our sample. Making use of a closed-cycle helium refrigerator, which was carefully adapted for CDW experiments by former group members and has been routinely used in this work, we could easily cool the sample to temperatures well below the NC-C phase transition temperature 180 K. For detailed discussions about the design and the operation of the refrigerator, the readers are referred to Ref. [9].

6.1.2 X-ray

Our x-ray diffraction data were collected at the C1 beamline at the Cornell High Energy Synchrotron Source. As far as the synchrotron x-ray beam is concerned, our experiment demands both a narrow energy band pass and good polarization purity. Depending on the monochromators installed in the beamline, these prop-

[1] As we have discussed in Section 5.3, such doping has only very little effect on x-ray scattering.

erties varied in different runs[2]. For a Si(111) double crystal monochromator, the energy resolution was approximately 5 eV. Given that the beam was predominantly linearly polarized within the horizontal plane, we utilized a polarimeter and determined the degree of linear polarization [10] was no better than 96.5%. Both the energy resolution and polarization purity could be improved by using a Si(220) double crystal monochromator. It was determined that the energy resolution of the x-ray beam from the Si(220) monochromator was $2 \sim 3$ eV. The degree of linear polarization was found to be 98% (horizontally polarized).

We chose to focus the x-ray beam (3 : 1 sagittal focused) at C1, resulting in some finite angular divergence corresponding to several milliradian. Immediately after the monochromator we had a Rh-coated mirror. Undesirable harmonics present in the x-ray beam from the high-energy source were carefully removed.

6.1.3 Diffraction geometry: four-circle mode

In Chapter 5 we explained that atomic scattering depends on both the incident polarization and the scattering polarization (Eq(5.10)). Hence it is very important that we can specify the geometry whenever we talk about resonant x-ray diffraction. The relative orientation between the x-ray polarizations and the crystal structure should be given. In our diffraction experiment, we used a four-circle diffractometer [3], on which our sample was deliberately mounted so that the $\mathbf{c}_0$-axis was made parallel to the diffractometer's ϕ axis. When changing the angles, the diffractometer was operated in the "omega-equals-zero" mode [4]. In this specific mode, the diffractometer-2θ angle is always set to be twice as large as the diffractometer-θ angle. The diffraction condition is fulfilled by the ϕ-rotation which moves reflec-

[2]For a detailed discussion of the energy resolution and of the polarization purity at C1, see Appendix .

tions to 90° from the the diffraction plane and by the χ-rotation which brings the reflections back into the diffraction plane. In the omega-equals-zero mode, the angle between the $\mathbf{c}_0$-axis and the diffraction plane is automatically maximized.

As far as the polarization effect of resonant x-ray diffraction is concerned, our choice of the omega-equals-zero mode was to make the polarization analysis as simple as possible. We did not consider to optimize the coupling of x-ray with any specific atomic orbital[3]. One can imagine that if we rotate the sample around the scattering vectors (so-called azimuthal scans), the relative orientation between the crystal and the polarization would be changed correspondingly. Resonant scattering would then occur differently. We know that, however, it would be a small effect, since the angular dependence needs to be averaged over all the unoccupied $5d$ states in the conduction bands.

6.2 Resonant X-ray Diffraction at CDW satellites

In our diffraction experiment, we measured the intensities of CDW satellites as functions of x-ray energy. According to the discussion of Section 4.2, we interpret the experimental data using the kinematic theory of x-ray diffraction. As Eq (4.19) suggests, both the LDW and the CMW can produce diffraction at the CDW satellites. Since the CMW causes very little diffraction, we can approximate the intensity by looking at only the diffraction by the LDW

$$I^{\mathbf{G}^{\mp}}_{\mathrm{TaS_2},\alpha\beta} \approx \Big(\frac{1}{\mu}\Big)\frac{\pi^3 c^3}{\omega^3}\frac{4r_0^2 I_0}{v_c^2 \sin 2\theta}|F_{\alpha\beta}|^2 \tag{6.1}$$

As we have changed the x-ray energy by only ± 40 eV around the Ta-L_3 edge (9.881 KeV), we can completely ignore the energy dependence associated with

[3]As an example of such coupling: the Ta $5d_{z^2}$ orbital corresponds to the matrix element with $(\hat{\mathrm{e}}^{\alpha} \cdot \mathbf{c}_0)(\mathbf{c}_0 \cdot \hat{\mathrm{e}}^{\beta})$ as its dependence on the x-ray polarizations.

ω^{-3}. The intensities of CDW satellites vary with x-ray energy because both $F_{\alpha\beta}$ and μ correspond to strong energy dependence near the absorption edge.

Let us first calculate the structure factor, taking into account that the CDW is characterized by the supercell[4] described in Section 3.3.1. Because of the LDW, the atoms are displaced. In the original lattice $\mathbf{R}$, the position of the jth atom is

$$\mathbf{r}_j = \mathbf{R} + \mathbf{d}_j + \Delta\mathbf{u}_j \tag{6.2}$$

as we recall the displacement $\Delta\mathbf{u}_j$ is determined by Eq (3.23). Making use of the superlattice $\underline{\mathbf{R}}$, we can rewrite the atomic position as

$$\mathbf{r}_j = \underline{\mathbf{R}} + \underline{\mathbf{d}}_j \tag{6.3}$$

with $\underline{\mathbf{d}}_j$ standing for the position of the atom inside the supercell. By construction, there are 39 Ta atoms and 78 S atoms in a supercell. All these atoms need to be included when we calculate the structure factor

$$F_{\alpha\beta}(\mathbf{Q},\omega) = \sum_j f_{j,\alpha\beta}(\mathbf{Q},\omega)\cdot e^{i\mathbf{Q}\cdot\underline{\mathbf{d}}_j} \tag{6.4}$$

Given any polarization combination α and β, Eq (5.10) and (5.11) can then be used in this equation for the atomic form factor of Ta. For S, there is no interesting feature in the atomic form factor near the Ta-L_3 edge. We can therefore write [2]

$$f'_{\mathrm{S}}(\omega) + if''_{\mathrm{S}}(\omega) = 0.27 + 0.37i \tag{6.5}$$

for S the same way as for Ta discussed in Eq (5.11), and we will assume that the dispersion correction of S is a diagonalized tensor. For the Thomson scattering components $f^0_{\mathrm{Ta},\alpha\beta}$ and $f^0_{\mathrm{S},\alpha\beta}$, we shall use the analytical approximations described in the International Tables for Crystallography [6].

[4]For this calculation, we can assume the superstructure of the CDW in the C phase. The lattice parameters of the corresponding supercell are $\underline{\mathbf{a}}_0 \equiv (4\mathbf{a}_0 + \mathbf{b}_0)$, $\underline{\mathbf{b}}_0 \equiv (-\mathbf{a}_0 + 3\mathbf{b}_0)$, and $\underline{\mathbf{c}}_0 \equiv 3\mathbf{c}_0$.

As our x-ray beam was produced by the synchrotron, the incident polarization $\hat{e}^{\alpha}$ was a unit vector in the horizontal plane. With the help of a polarimeter, we could selectively look at either polarization-*preserved* scattering ($\hat{e}^{\beta} = \hat{e}^{\alpha}$) or polarization-*flipped* scattering ($\hat{e}^{\beta} = \hat{e}^{\alpha} \times \mathbf{q}'/|\mathbf{q}'|$). Since Thomson scattering corresponds to the diagonalized component of the atomic form factor tensor, only the polarization-preserved scattering will see Thomson scattering. In Figure 6.1 we show the kinematic theory calculated for a CDW satellite (1.245 $\overline{0.068}$ 1.667). Clearly the polarization-preserved scattering and the polarization-flipped scattering give very different results. Because the dispersion correction of Ta is small compared to $f^0_{\mathrm{Ta},\alpha\beta}$, in the polarization-preserved scattering the real part of the atomic form factor never becomes inferior to the imaginary part in magnitude. Correspondingly the kinematic theory is predominated by $(f^0_{\mathrm{Ta},\alpha\beta} + f'_{\mathrm{Ta},\alpha\beta})$, which exhibits a minimum near the absorption edge. In the polarization-flipped scattering, the intensity is characterized by the dispersion correction only. From Eq (5.11) we see the off-diagonal elements are small compared to the diagonal elements. This explains why the polarization-flipped scattering is relatively weak.

We could also measure *unpolarized* scattering. In this case, we did not let the diffracted beam pass the polarimeter. The measured intensity was therefore the combination of both the polarization-preserved and the polarization-flipped scattering, and we expect the intensity is predominated by the polarization-preserved scattering.

6.2.1 Experiment setup

X-ray diffraction configuration

Our x-ray diffraction experiment used a rather simple setup. In Figure 6.2 we

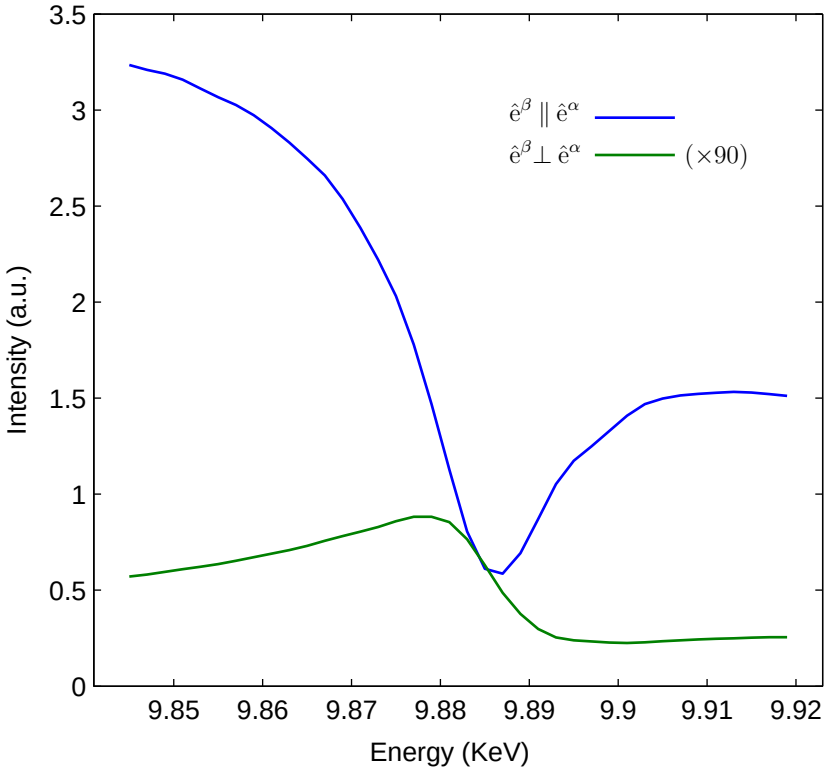

Figure 6.1: The calculated intensity of the CDW satellite (1.245 $\overline{0.068}$ 1.667) as a function of x-ray energy based on Eq (6.1). The intensity looks completely different in polarization-preserved scattering ($\hat{e}^\beta \parallel \hat{e}^\alpha$) and in polarization-flipped scattering ($\hat{e}^\beta \perp \hat{e}^\alpha$). In polarization-preserved scattering, the dispersion corrections are added to the large Thomson scattering components f^0. By contrast, only the dispersion correction is measured in polarization-flipped scattering.

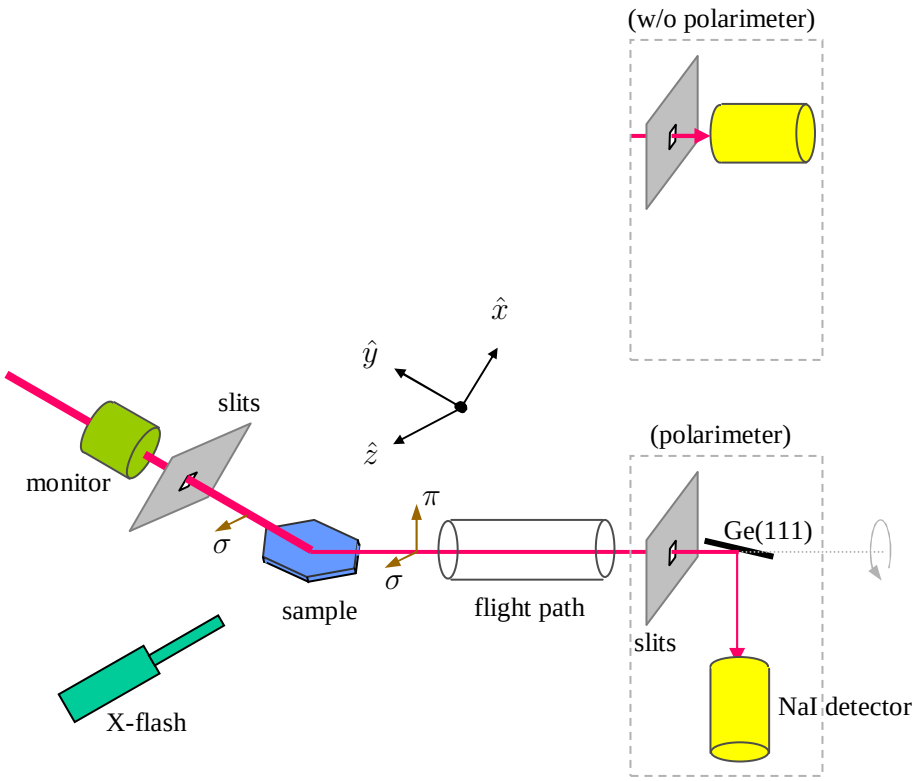

Figure 6.2: The schematic for the x-ray diffraction experiment of CDW satellites. The $1T$-TaS_2 crystal was mounted on a *vertical* four-circle diffractometer, whose coordinate system was defined in accordance with the standard definition [3]. X-ray was diffracted in the $x-y$ plane, and z is the direction of the incident polarization. The x-ray polarization is referred to as the σ- (π-) polarization if it is perpendicular (parallel) to the $x-y$ plane. Depending on whether we put the polarimeter in place, diffraction could be measured with or without polarization analysis. To monitor fluorescence, an energy-resolving detector (X-flash) was used to look at the sample along the z direction.

show the experiment configuration. On the four-circle diffractometer at C1, x-ray diffraction took place in the vertical plane, with the incident x-ray beam being characterized by the σ-polarization. Immediately before the sample was a set of slits which limited the beam to 0.5×0.5 mm^2. In the case where the polarimeter was used, x-ray diffraction was once again reflected at an analyzer crystal. Otherwise diffraction was directly collected by a NaI scintillator detector after passing through a final set of slits. The large distance (75 cm) from the sample to the detector ensured that the measured intensity was very little contaminated by fluorescence. In this experiment, we used a Si(220) monochromator.

Polarimeter

The geometry of the polarimeter deserves a more detailed discussion. For the analyzer of the polarimeter, we took advantage of the (620) reflection of a (111)-cut Ge crystal. At 9.881 KeV, the Bragg angle of this particular reflection is $\theta_a = 44.6123°$, which in turn provides a superb suppression $\cos^2 2\theta_a \sim 1/5500$ for $\pi - \pi$ reflection. We also calculated the Darwin width equal to 27.5×10^{-6} rad $= 0.00157°$. Comparing this number with the widths of the CDW satellites (typical values are $\sim 0.15°$), we found we were seriously limited by the small angular acceptance of the (620) reflection. To increase the signal-to-noise ratio, we invoked an asymmetric reflection geometry. The (111)-cut crystal allowed us to make an incident angle θ_i as shallow as $1.5233°$. For such a shallow incident, the asymmetry parameter $b = \sin(2\theta_a + \theta_i)/\sin\theta_i = 37.59$. According to the Liouville's theorem [3], we blew up the angular acceptance by a factor $\sqrt{b}/\tan\theta_a = 6.215$. The final angular acceptance was $0.0098°$. We made the analyzer pass more than 5% of diffraction created by the sample.

6.2.2 Result

Unpolarized intensity of CDW satellites

In Figure 6.3 we plot the unpolarized intensities of two CDW satellites as functions of x-ray energy. In these energy scans, the sample was kept at the room temperature. As we can see in the Figure, the intensities of CDW satellites show clear minimum around 9.886 KeV. The intensities are asymmetric about the minimum. The intensities are higher at the lower-energy side than the higher-energy side. In this part of the experiment, we measured five different CDW satellites. It is found the intensity minimum and the asymmetric shoulders are the common characteristics of all the CDW satellites.

The kinematic theory tells us why the CDW satellites show this interesting energy dependence in their intensities. For comparison, we also plot the calculated intensities in Figure 6.3 based on Eq (6.1). As can clearly be seen in the Figure, the kinematic theory describes the data fairly well. Especially around the minimum, we succeed in reproducing the energy dependence of the measured intensities. At energies that are well-below and well-above the absorption edge, the theory predicts intensities that are consistent with the observed values[5]. Besides the incident intensity I_0, which in turn serves as a scaling constant in Eq (6.1), there is no adjustable parameter in the kinematic theory. Everything needed to be measured and was measured in experiments. We determine that the kinematic theory is indeed an adequate description of the energy behavior of the CDW satellites.

[5]We noticed, however, there are errors in the theory regarding the relative intensities of the higher-energy side and the lower-energy side. We attribute such errors to our method of deriving the atomic form factor from the absorption spectra. Physically, the only thing that matters in resonant scattering is the direct transitions between the core level states and the valence band states. The absorption spectra, on the other hand, may include other effects such as multiple scattering and the auger effect. A complete theory of the absorption spectra can certainly go beyond the interpretation discussed in Chapter 5 (as primarily given in Eq (5.1) and (5.3)). We are therefore not surprised at the errors.

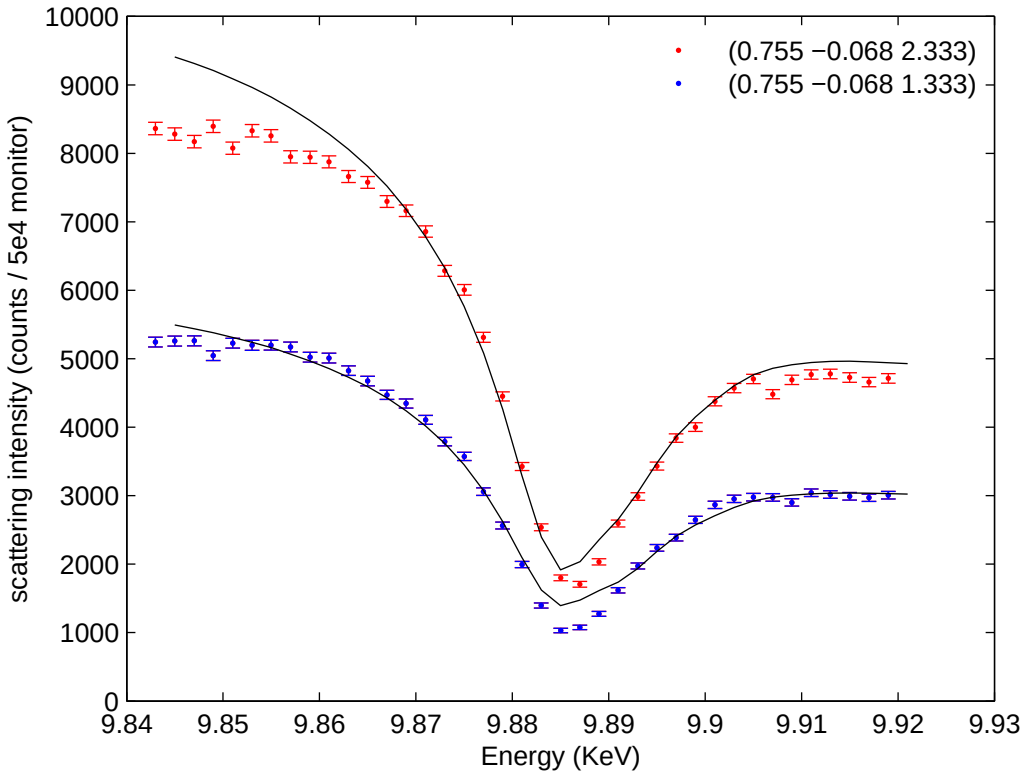

Figure 6.3: Energy scans taken at the two CDW satellites (0.755 $\overline{0.068}$ 1.333) and (0.755 $\overline{0.068}$ 2.333) at room temperature. Without a polarimeter, the measured intensities include both the polarization-preserved scattering and the polarization-flipped scattering. The solid lines are the calculated intensities due to the kinematic theory in Eq (6.1).

When we first saw the intensity minimum of the CDW satellites around the Ta-L_3 edge, we could not understand why resonant x-ray scattering turns out to be a reduction rather than an enhancement in x-ray diffraction. According to the kinematic theory, the intensity is directly proportional to $|F_{\alpha\beta}|^2$ and is inversely proportional to μ. Inside the structure factor, it is the large real part of the Ta atomic form factor that determines the energy dependence of $|F_{\alpha\beta}|^2$. From our discussion about the Ta atomic form factor, especially the numerical values given in Figure 5.6, we realize that $|F_{\alpha\beta}|^2$ corresponds to a minimum near the Ta-L_3 edge. The large absorption associated with the white-line further reduces the diffraction intensities. The low intensities on the high-energy side are a direct consequence of x-ray absorption which dominates when the energy is higher than the absorption edge.

CDW satellites at different temperatures

By cooling down the sample, we made the CDW of $1T$-TaS_2 undergo a phase transition at 180 K. As we have discussed in Section 3.3.2, the CDW in the C phase develops a pseudogap in the $5d_{z^2}$ valence band. It is interesting to determine whether resonant x-ray diffraction is sensitive to such a change in the electronic structure.

In Figure 6.4 and 6.5 we show the polarized intensities of a CDW satellite ($1.245\ \overline{0.068}\ 1.667$) at four different temperatures. The intensities are normalized so they can easily be compared. In the case where σ-scattering (polarization-preserved) is measured, we find the intensities show an energy dependence that is very similar to the unpolarized intensities. Here, the structure factor is strongly affected by the dispersion correction of the atomic form factor of Ta, but the measured intensities are still dominated by Thomson scattering. Things are quite

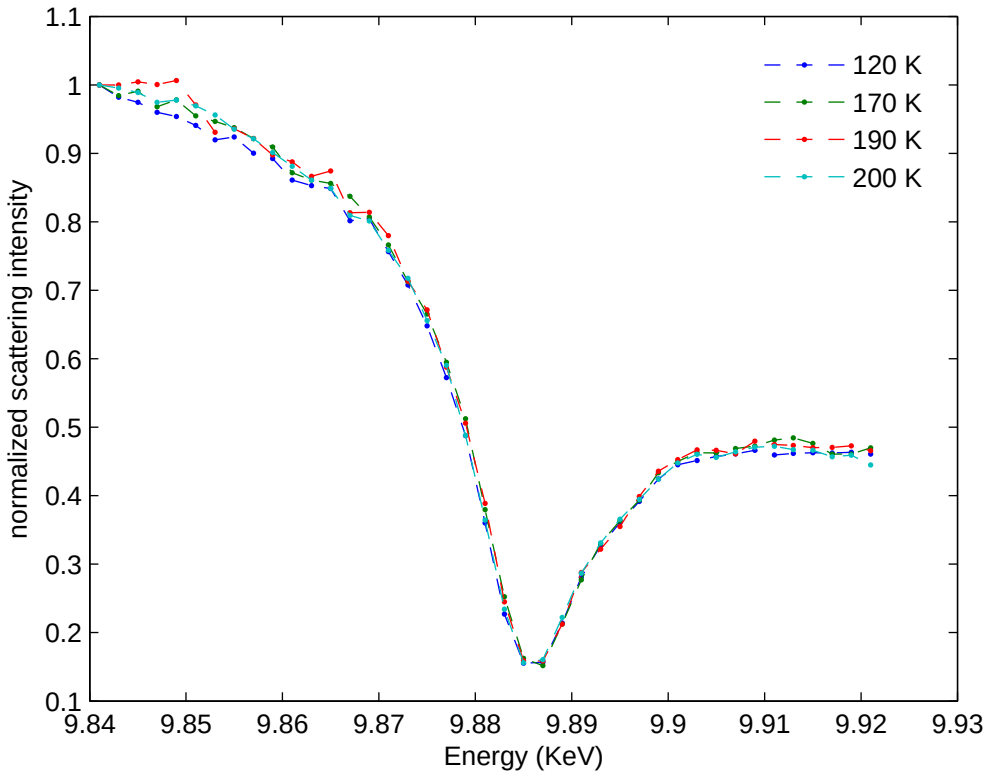

Figure 6.4: Energy scans of the CDW satellite (1.245 $\overline{0.068}$ 1.667) peak intensity at different temperatures. Here the polarimeter selects only scattering that is polarization-preserved, i.e. the $\sigma - \sigma$ scattering.

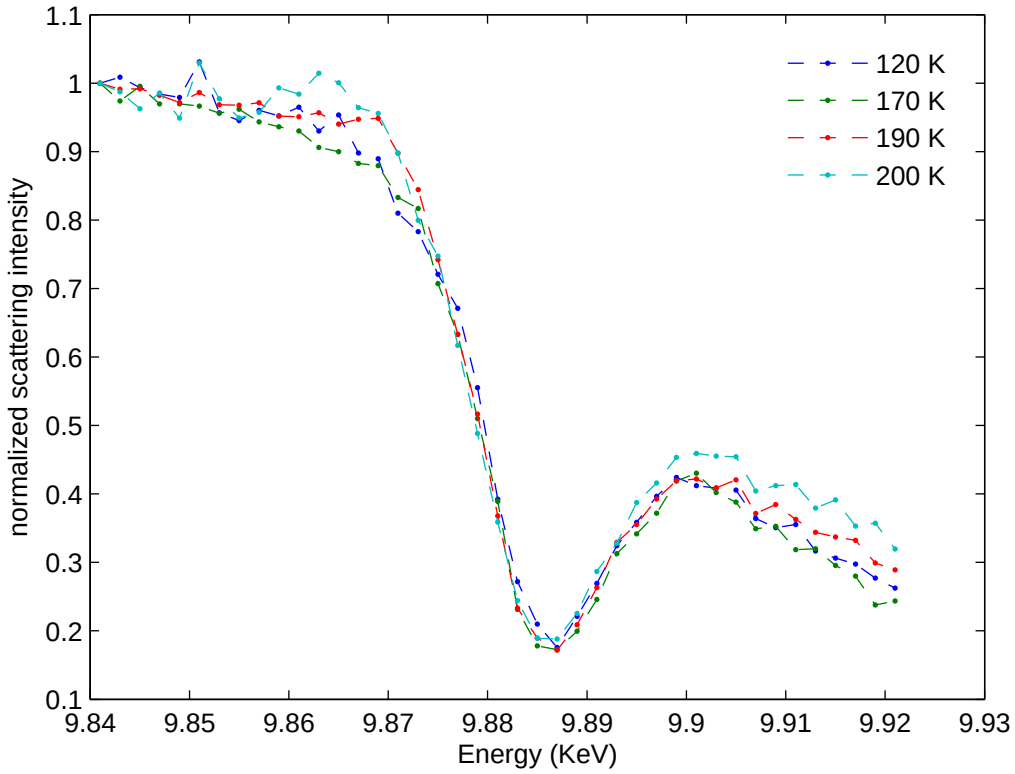

Figure 6.5: Energy scans of the CDW satellite (1.245 $\overline{0.068}$ 1.667) peak intensity at different temperatures. In these measurements, the polarimeter was set up to select scattering with the flipped polarization (σ to π). However, because we had a finite π-polarization component ($\sim 2\%$) in the incident x-ray beam, the results must contain $\pi - \pi$ scattering, too. From the discussion of Figure 6.1, we learn that the polarization-preserved scattering is approximately one hundred times as strong as the polarization-flipped scattering. Our experiment was conducted with just enough sensitivity to see the $\sigma - \pi$ scattering in the $\pi - \pi$ scattering background.

different in the π-scattering (polarization-flipped) measurement. Here Thomson scattering is totally irrelevant. By looking at $\sigma - \pi$ scattering, we would have only seen scattering due to the dispersion corrections. However, because we did not have a perfect polarized x-ray beam, we included some certain amount of π-π scattering in the measured intensities. Being polarization-preserved, π-π scattering is characterized by the same energy function as σ-σ scattering. Thus σ-π scattering is obtained from the mixed data in Figure 6.5 by subtracting the functions shown in Figure 6.4. If we compare the two Figures, we see a gentle hump appearing on the lower energy side of the minimum in π-scattering. As we have discussed in Figure 6.1, this is the polarization-flipped component in the intensity of the CDW satellite. Finally, the decreasing intensities between 9.90 KeV and 9.92 KeV in the π-scattering measurement are hard to understood. It might be because we failed to capture the entire reflection coming off from the analyzer crystal. At these high energies, the analyzer crystal was working at some really shallow incident angles. At 9.92 KeV, the footprint of x-ray diffraction was estimated to be more than 7 cm, exceeding the size of the active area of the NaI detector.

As neither the $\sigma - \sigma$ scattering nor the $\sigma - \pi$ scattering shows measurable temperature effects in the intensity of the CDW satellite[6], we determine that at the Ta-L_3 edge, resonant x-ray diffraction is not sensitive to the CDW in the different phases. Physically, this is understandable because the CMW is indeed a very small charge modulation appearing in the nearly empty $5d$ bands.

[6]In π-scattering, our measurements at different temperatures do not always agree with each other. We attribute this problem to the poor counting statistic and other systematic errors. Given that the CMW involves only a tiny fraction of conduction electrons and occurs only around the Fermi energy, the intensity change appearing in Figure 6.5 between 9.86 KeV and 9.87 KeV should not be considered to be CDW-related.

6.3 Resonant X-ray Diffraction at Bragg Peaks

When we conducted the diffraction experiment for Bragg diffraction peaks, we did not measure the Darwin reflectivity curves. Instead, it is the area under the Darwin reflectivity curves that we measured as the intensities of the Bragg peaks. Using Eq (4.27) we estimate the angular Darwin widths are in the order of 10^{-2} mrad for the Bragg peaks we studied. As the x-ray beam at C1 showed an angular divergence much larger than the angular Darwin widths, our diffraction experiment measured the integrated reflectivity of each Bragg peak.

6.3.1 Model

Just like our discussion about the CDW satellites due to the kinematic approach, in the dynamical theory, resonant x-ray diffraction is attributed to the dispersion correction of Ta which shows strong energy variance near the L_3 edge. Indeed, the dynamical theory can be best appreciated by differentiating the distinct roles played by the real and the imaginary parts of the dispersion correction. Using the (002) Bragg peak as an example, we illustrate the physical concept as follows. In Figure 6.6(b), we plot the Darwin reflectivity curve at several different energies. With increasing x-ray energy, the Darwin reflectivity curve changes its shape. Before the reflectivity finally gets stabilized above the edge, it actually becomes really low at the white-line. It is known that within the Darwin width, the reflectivity may become very different from unity if x-ray is largely attenuated. Since absorption is directly related to f''_{Ta}, the shape of the Darwin reflectivity curve is determined solely by the imaginary part of the dispersion correction. On the other hand, the Darwin width depends on both the real and the imaginary part of the

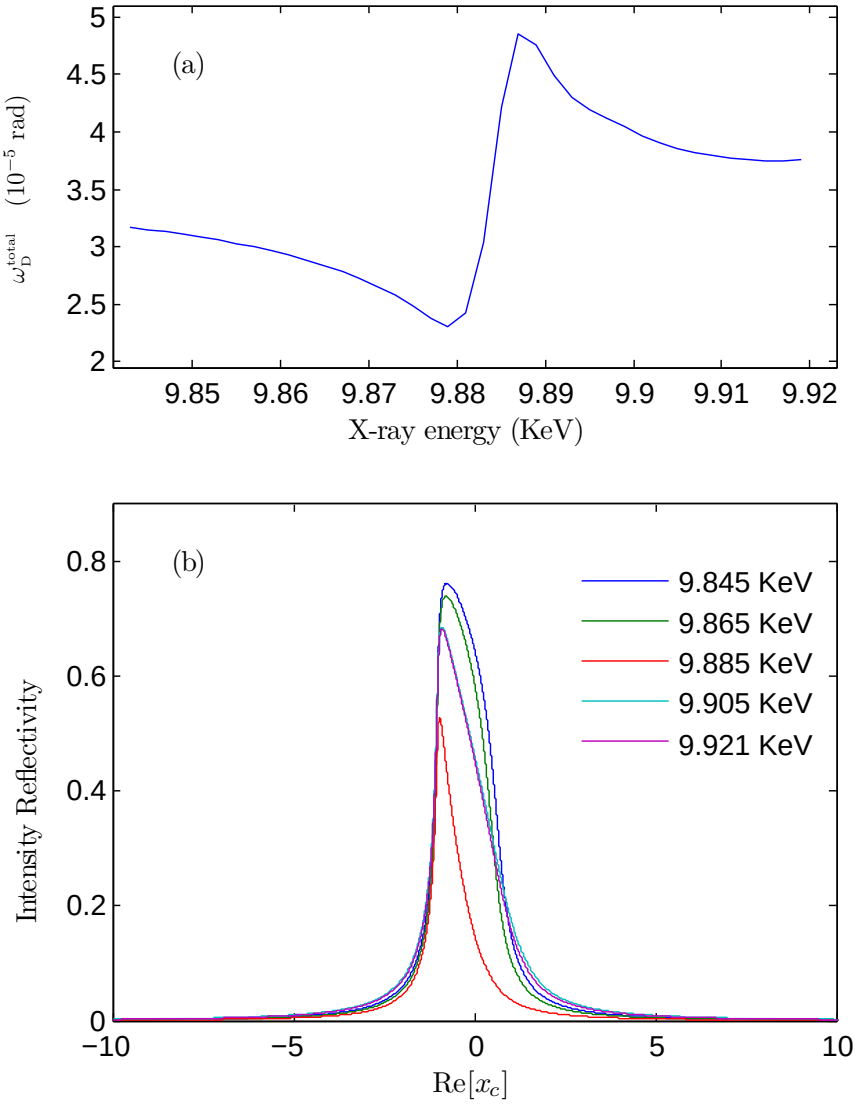

Figure 6.6: (a) The Darwin width $\omega_{\mathrm{D}}^{\mathrm{total}}$ and (b) the Darwin reflectivity curve of the (002) Bragg diffraction peak of 1T-TaS_2 as a function of x-ray energy.

dispersion correction. In Figure 6.6(a) we show the Darwin width as a function of x-ray energy (Eq (4.27)). By carefully analyzing the energy dependence of the Darwin width, we find the maxima (minima) in the Figure indeed results from the real (imaginary) part of the dispersion correction. Since the integrated reflectivity is proportional to the product of the area under the Darwin reflectivity curve and the Darwin width, the imaginary part of the dispersion correction is associated with the reduction of the measured intensity of the Bragg peak.

As we have already pointed out in Section 4.3, the CDW is a second-order effect for Bragg peaks. When we calculate the structure factor, we use the unit cell pertaining to the original structure of $1T$-TaS_2.

6.3.2 Experiment

We measured Bragg reflection peaks using a horizontal four-circle diffractometer. The setup is similar to the experiment shown in Figure 6.2, except the incident polarization is now along the x direction (π-polarized). For the monochromator, we used Ge rather than Si. We measured the intensities of several Bragg peaks without using a polarimeter. The entire experiment was conducted at room temperature.

6.3.3 Result

In Figure 6.7 we plot both the measured and the calculated intensities of three Bragg peaks as functions of x-ray energy. Representing all the Bragg peaks we have studied, these peaks show clear minimum around 9.886 KeV as well as uneven shoulders. However, compared to the situation of CDW satellites, Bragg peaks are

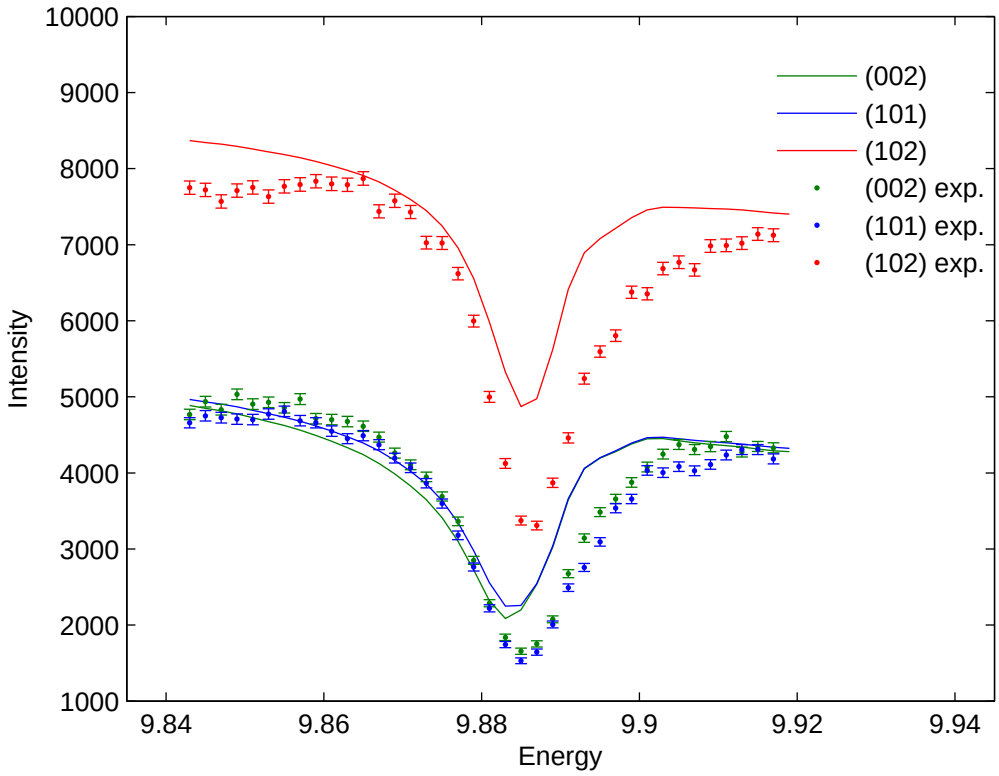

Figure 6.7: Energy scans of three major Bragg reflection peaks of $1T$-TaS_2. Solid lines represents the predicted energy behavior due to the integrated reflectivity based on the dynamical theory.

less asymmetric around the minimum[7]. As we can clearly see in the Figure, the dynamical theory captures all these observed features. We want to emphasize the fact that when we determined the calculated intensities, no adjustable parameter has been assumed except the overall scaling factor. Everything came out from the dynamical theory automatically.

Although the dynamical approach of x-ray diffraction works fairly well for Bragg peaks, there are clear discrepancies between the theory and the observation. One thing we have noticed is that the theory always predicts intensities that rise too early before the white-line. We wonder whether this is because the absorption effect can actually appear in a more delicate way than our dynamical treatment. For example, it is commonly known that in the case of large absorption, x-ray diffraction becomes very sensitive to sample properties such as surface roughness and mosaic[8]. These situations, however, have not been considered in our simple treatment. If we assume that mosaic indeed plays an important role in our experiment, a proper description of the measurement will be a mixture of the dynamical theory and the kinematic theory. Based on this idea, we may create a model that better fits the data around the minimum. Given the fact that our sample is indeed subject to finite mosaic broadening ($\sim$ 1 mrad), the imperfectness of the crystal seems to be a plausible explanation for the discrepancy found in Figure 6.7.

[7]As a matter of fact, because the kinematic approach failed to predict the correct sizes of the measured intensities below and above the absorption edge, we began to realize that our understanding of x-ray diffraction at Bragg peaks requires the use of the dynamical theory.

[8]By increasing x-ray absorption, the angular width of dynamical diffraction is decreased. Mosaic renders difficult so-called secondary extinction [8] within the diffracting crystal. In dynamical theory, this means diminishing Bragg diffraction.

BIBLIOGRAPHY

[1] Kristin Lee Ringland. *The Structure and Kinetics of Charge Density Waves*. PhD thesis, Cornell University, January 2000. Section 4.3.

[2] Doon Gibbs, D. R. Harshman, E. D. Isaacs, D. B. McWhan, D. Mills, and C. Vettier. Polarization and resonance properties of magnetic x-ray scattering in holmium. *Phys. Rev. Lett.*, 61(10):1241–1244, Sep 1988.

[3] Certified Scientific Software. `spec`™: X-ray diffraction software. Internet resource at http://www.certif.com/spec_ manual/fourc_ 4_ 1.html. Four-Circle Reference.

[4] W. R. Busing and H. A. Levy. Angle calculations for 3- and 4-circle x-ray and neutron diffractometers. *Acta Crystallographica*, 22(4):457–464, Apr 1967.

[5] Lawrence Berkeley National Laboratory Center for X-Ray Optics. X-ray interactions with matter. Internet resource at http://henke.lbl.gov/optical_constants/asf.html. The Atomic Scattering Factor Files.

[6] *International tables for crystallography*, volume C. Dordrecht, Boston, 3rd edition, 2004. Published for the International Union of Crystallography by Kluwer Academic.

[7] Jens Als-Nielsen and Des McMorrow. *Elements of modern X-ray physics*. John Wiley and Sons Ltd, New York, 2001. Section 5.4.7.

CHAPTER 7

SUMMARY AND DISCUSSION

In this chapter we summarize our study of resonant x-ray diffraction from the CDWs in $1T$-TaS_2. To further enhance our appreciation of the phenomenon of resonant x-ray scattering, we will then compare our study with similar experiments performed in other systems. Potential future works will also be discussed.

7.1 Project Summary

Using basic quantum mechanics together with the tight-binding theory, we demonstrate that resonant x-ray scattering can be used to study the extended valence-band states of solids. In $1T$-TaS_2, the CDW affects the Ta atomic form factor, of which the dispersion correction is modulated in accordance with the CMW. Furthermore, our analysis due to the Peierls theory shows that the modulation is a meager change of the atomic form factor. Recognizing the CMW is indeed imposed to the system as a superstructure, we have determined that x-ray scattering will be generated at $\mathbf{G} \mp \mathbf{k}_{\mathrm{CDW}}$ — the so-called CDW satellite positions in the reciprocal space.

Given that the CMW and the LDW can both yield x-ray scattering at the CDW satellites, we set out to look at their difference in resonant x-ray scattering. In our theory we showed that diffraction of the CMW is characterized by the CMW modulation of the Ta atomic form factor, whose imaginary part $\tilde{f}''_{\mathrm{Ta}}$ peaks only around the edge of the CDW gap. Accordingly, diffraction of the CMW is localized in energy. Diffraction of the LDW, on the other hand, depends on the full dispersion correction of the atomic form factor. Since the dispersion correction results from

the entire valence bands, diffraction of the LDW corresponds to energy features on a much larger scale in resonant x-ray scattering. In our experiments, we observed only diffraction of the LDW; the CMW is not visible in the resonant x-ray scattering measurement done at the Ta-L_3 edge. We pointed out the core-hole lifetime is a quantity of critical importance in resonant x-ray scattering. At the L_3 edge, diffraction of the CMW is broadened by the 5-eV core-hole lifetime $\Gamma_{\mathrm{Ta}}^{\mathrm{L3}}$. The corresponding large natural width of the atomic transitions is very unfavorable in the resonant x-ray diffraction experiment of our CDW, as the CMW appears in the continuous valence bands and is indeed a very delicate energy structure.

The CMW of 1T-TaS_2 is known to show Mott localization around the NC-C phase transition temperature. In principle, CDW satellites will reflect such a physical change in resonant x-ray scattering. We measured the intensities of several CDW satellites at temperatures both above and below the transition temperature. We could barely discern a temperature effect. This null result is attributed to the smallness of $\tilde{f}''_{\mathrm{Ta}}$ as it was described earlier.

Although in our diffraction experiment we could not exclusively probe the CMW, we have learned a great deal about resonant x-ray scattering from CDWs. We have demonstrated that the kinematic theory is an effective description for resonant x-ray diffraction at the CDW satellites. Hence the effect of x-ray absorption in resonant x-ray scattering is now well understood. The significance of our kinematic theory is also elucidated in the comparison between the CDW satellites and the Bragg reflections, for which the dynamical theory is needed instead. We benefit particularly from having the thorough discussion about resonant x-ray scattering given in Chapter 2. As we have learned there, the real part of the dispersion correction extends all the way to the zero frequency. No wonder we could always observe polarization-flipped scattering even when we stay below the absorption edge. In

the polarization-preserved measurement, scattering was dominated by Thomson scattering. As far as the numbers are concerned, the dispersion correction has a rather small real part at the L_3 edge. Physically, this means that most Ta electrons scatter with x-ray energy higher than the binding energies. We recognize this is the nature of the Ta-L_3 edge.

In order to determine the atomic form factor, we had to perform a very careful measurement on the x-ray absorption spectra of 1T-TaS_2. We found that the x-ray polarization has only a marginal effect on x-ray absorption. We attribute the results described in the earlier report to the thickness effect.

Indeed, we have accomplished a systematic study on both resonant x-ray scattering and CDWs in this research project. The fact that we are not able to measure the CMW may sound disappointing, but there is always something we can do. With the thorough understanding we can easily improve our experiment, as well as apply the techniques to study other interesting condensed matter systems. The ideas will be discussed in the following.

7.2 Resonant X-ray Scattering in Other System

Resonant x-ray scattering has been seen in many different systems. Let us first look at how the technique is used to extract structural information about some of the most interesting phenomena in condensed-matter physics. We will study two well-known experiments. They are magnetic x-ray scattering from holmium and resonant soft x-ray scattering from doped cuprate $La_{1.875}Ba_{0.125}CuO_4$.

7.2.1 Magnetic x-ray scattering from holmium

As one of the very first demonstrations of resonant x-ray scattering, magnetic x-ray scattering was discovered for elemental holmium (Ho, Z=67) approximately two decades ago [10]. The name "magnetic x-ray scattering" was coined because here the interaction between x-ray and atomic electrons involves the orbital magnetic moment and the spin magnetic moment of the electrons. Despite of this difference, magnetic x-ray scattering is described by a theory that is very similar to that developed in this thesis. The experiment was conducted by Gibbs, *et al.* in 1988. They looked at magnetic x-ray scattering at the Ho-L_3 edge at 8.067 KeV.

Holmium forms a spiral antiferromagnet. Magnetic x-ray scattering senses the magnetic superstructure, resulting in diffraction satellites around the Bragg peaks [10]. As the lattice is free of any displacement, there is no lattice diffraction at the satellites; those satellites are forbidden reflections in convention x-ray diffraction. The fact that this Ho experiment measures resonant x-ray scattering at those otherwise forbidden positions is an important difference compared to our CDW experiment. Whatever the Ho atomic form factor is, magnetic x-ray scattering results only from the variation of the atomic form factor. There is no Thomson scattering at the satellites. Inside the material, the Ho $5d$ bands are virtually empty. All those bands contribute in magnetic x-ray scattering. Yet their effect will not show up in the final diffraction. The observed satellites are exclusively magnetic x-ray scattering.

Figure 7.1 shows what the researchers saw in their magnetic x-ray scattering experiment. The x-ray absorption coefficient is measured to characterize the absorption edge. A prominent white-line is clearly seen in the absorption spectra. Diffraction satellites up to the forth order beautifully show up at energies slightly lower than the white-line at 8.071 KeV. By analyzing the polarization properties

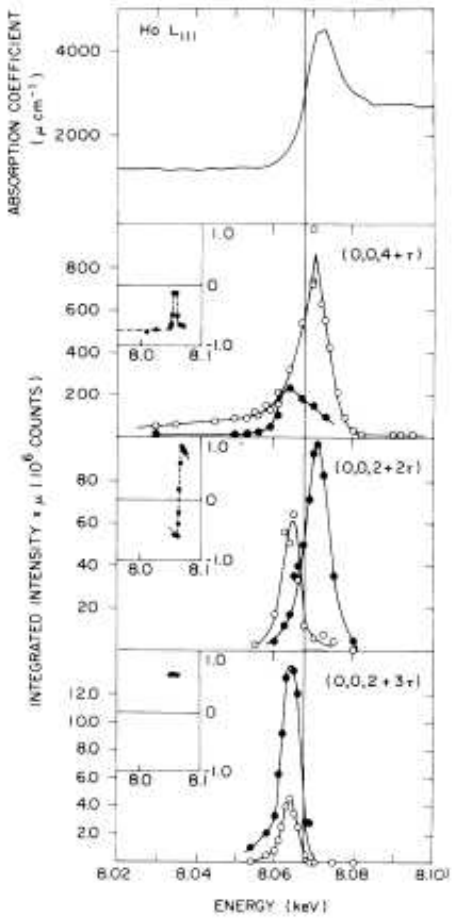

Figure 7.1: Top: Measured absorption coefficient of Ho antiferromagnet around the Ho L_3 edge. Lower: Integrated intensities plotted vs energy for the linear components scattered parallel (open circles) and perpendicular (filled circles) to the diffraction plane at three different diffraction satellites. Inset, lower: Corresponding degree of linear polarization plotted vs energy. The solid vertical line indicates the energy of the edge. Reproduced from Ref. [10].

of those satellites [4], the researchers determined there are two different resonant processes for magnetic x-ray scattering. The result is presented in such a way that the absorption effect has been consistently removed by multiplying the intensity functions with the the absorption coefficient. This manipulation is consistent with our description of the absorption effect in the kinematic theory.

These energy scans show that magnetic x-ray scattering corresponds to features which are approximately 5-eV to 10-eV-wide. One would recall our discussion of the natural width. For the Ho-L_3 edge, the core-hole lifetime was calculated to be 4.26 eV [1]. Based on our description, this number sets the lower bound of the widths of the resonant effect. The experimental finding supports this interpretation.

7.2.2 Probing valence electron orders using resonant soft x-ray scattering

We now consider a relatively more recent work on resonant x-ray scattering from doped antiferromagnetic cuprate $La_{1.875}Ba_{0.125}CuO_4$ (LBCO). The paper was published in 2005 by Abbamonte *et al.* [5]. This experiment particularly attracts our attention because it deals with a physical situation very similar to our CDW problem. The researchers studied the spatial ordering of the valence-band charges in LBCO using resonant soft x-ray scattering.

In LBCO, the charge/spin superconductivity appears only in the low-temperature tetragonal (LTT) phase and coincides with the suppression of the critical temperature [6]. Because of doping, O can have unoccupied $2p$ orbital, that is holes. Finite interactions exist between the hole modulation and the underlying lattice. As a result, the LTT phase is characterized by charge strips which have been pinned

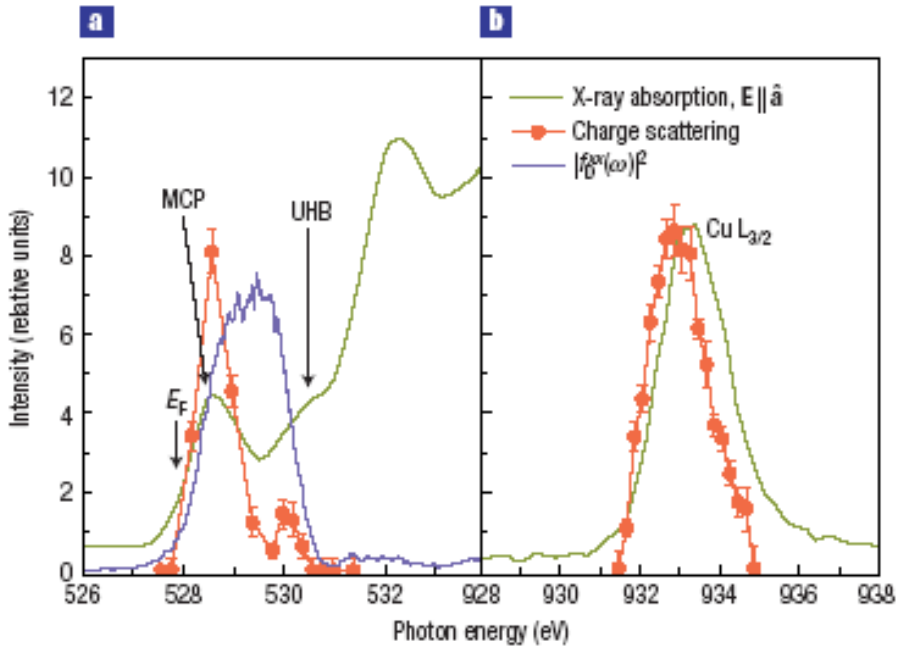

Figure 7.2: The energy dependence of the (0.25 0 L) charge scattering of LBCO compared with the x-ray absorption spectra (green lines). **a.** Data near the O-K edge. Red circles, intensity of charge scattering at $L = 0.72$ showing enhancements at the MCP and UHB. E_F is the Fermi energy. Blue line, see the original reference. **b.** Data near the Cu-L_3 edge for $L = 1.47$. Reproduced from Ref. [5].

by the distorted lattice. Like the CDW of 1T-TaS_2, the modulation of the hole distribution shares the same spatial period with the distorted lattice.

As the researchers have described in their paper, the determination of the hole distribution involves both x-ray absorption measurements and x-ray diffraction measurements. Using the x-ray absorption spectra taken at the O-K edge, they showed there are a distinct mobile carrier peak (MCP, located at 528.6 eV), corresponding to transitions into the doped hole levels, and an upper Hubbard band (UHB, located at 530.4 eV), corresponding to transitions into the d-level of a neighboring Cu atom. Given that the spectral weight of the MCP increases with the hole density, the MCP is related to the local hole density. Similarly, at the Cu-L_3 edge, it was found that the x-ray absorption spectra shows a main peak (933 eV) together with a ligand hole sideband peak (934.3 eV). See the reproduced plots described in Figure 7.2.

When it came to measure x-ray diffraction, the researchers took diffraction of the Cu main peak to be a measure of the distortions in the Cu sublattice and took diffraction of the MCP to be a measure of the hole distribution. As Figure 7.2 shows, the experiment saw nice peaks at both the Cu main peak and at the MCP. Given that we always observed x-ray resonance scattering in our energy scans as a resonant "dip", why is the outcome of this LBCO experiment so different? Is there any fundamental difference between resonant x-ray scattering from Cu and O and resonant x-ray scattering from Ta?

After we carefully thought about the theory of resonant x-ray scattering, we realized that at those specific absorption edges, the real parts of the dispersion corrections of Cu and of O are very large negative numbers so the real parts of the atomic form factors are rather small compared to the imaginary parts. In Figure 7.3 (7.4), we show the atomic form factor of Cu (O) as a function of x-ray energy,

assuming a direction of the forward scattering $\vec{\mathbf{Q}} = 0$. We notice immediately that at the Cu-L_3 (O-K) edge, the changes are so prominent that the real part of the atomic form factor actually turns negative. Looking at other atomic species, we find this situation is very common in light elements. When such an atomic form factor is used in the kinematic theory of resonant x-ray diffraction, they always result in a resonant peak right below the absorption edge. Now recall the discussion in Chapter 2 about the energy behavior of x-ray scattering. An atomic form factor with a small real part means the atom has not yet been driven hard enough to create Thomson scattering. In this aspect, resonant peaks are more directly related to the resonant x-ray scattering behavior of atoms than resonant dips. Taking this as their advantage of having light elements resonating with x-ray, the researchers saw the clear resonant peaks in the LBCO experiments.

The LBCO experiment is indeed a very clever method to probe the charge order independent from the lattice distortion. They used two different resonant x-ray scattering to measure each phenomenon separately. As a final remark, I would like to point out that the paper can directly attribute diffraction of the CMP peak to the hole modulation only because it assumes there is no O displacement inside the distorted lattice.[1] If O does displace in accordance with the Cu sublattice, just like the situation we had in the CDW problem, there will be a lattice component in diffraction of the CMP. As the distorted lattice may overwhelm the hole modulation in terms of their diffraction power, determining the charge order using resonant soft x-ray scattering can actually become a much more challenging job.

[1]Given that Cu is displaced, however, it is not obvious to me why O should not have any concomitant displacement.

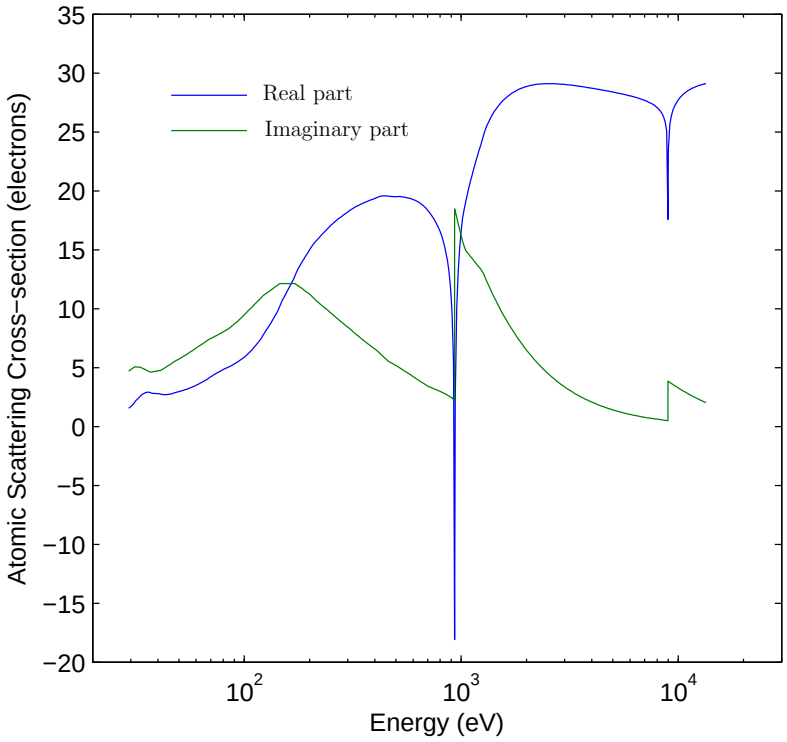

Figure 7.3: The real part and the imaginary part of the atomic form factor of Cu ($Z = 29$), assuming $\vec{\mathbf{Q}} = 0$. Note around the Cu-L_3 edge at 932.7 eV the real part actually take negative values. Also the real part only become close to its maximum after the L_3 edge. This plot is drawn to show the general trend of the function of the atomic form factor. Detailed structures such as white-lines at the absorption edges are not shown. Reproduced from data found in the CXRO website [2].

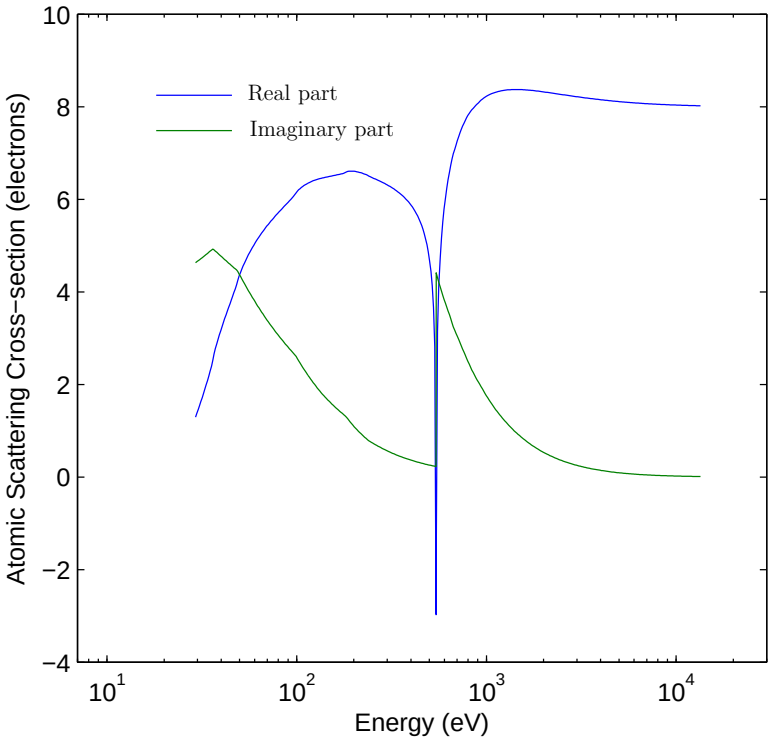

Figure 7.4: The real part and the imaginary part of the atomic form factor of O ($Z = 16$), assuming $\vec{\mathbf{Q}} = 0$. Note around that the O-K edge at 543.1 eV, the real part becomes negative. Also the real part only become close to its maximum after the K edge. This plot is drawn to show the general trend of the function of the atomic form factor. Detailed structures around the absorption edge are not shown. Reproduced from data found in the CXRO website [2].

7.2.3 Comparison with the CDW experiment

A very useful concept that is commonly used to predict the the strength of the resonant x-ray diffraction is the number of the resonating electrons (or "states", as a more precise term in the resonant scattering theory) in each unit cell. We want to generalize this concept and estimate the "contrast" of the atomic form factors of resonating atoms. We would like compare the experiment of magnetic x-ray scattering from Ho, the experiment of resonant soft x-ray scattering from LBCO, and our experiment of resonant x-ray scattering from the CDW of $1T$-TaS_2.

Judging from the positions of the satellites, the magnetic superstructure of Ho corresponds to a period six times greater than that of the lattice structure in the c_0^* direction. We can then infer that the difference of the atomic form factor in magnetic x-ray scattering is one out of six states per unite cell. For the LBCO experiment, the paper gives a number which is equal to the difference of 0.063 holes between the "peak" and the "trough" of the carrier modulation. In our own experiment, we have determined that the size of the CMW is equal to one thirteenth electrons per Ta atom. As far as these numbers are concerned, our CDW is not that different from the LBCO (0.077 compared to 0.065). It is, however, very difficult for us to isolate the CMW effect in our experiment.

From the band structure calculation, we have learned that $1T$-TaS_2 has several unoccupied Ta-$5d$ bands besides the $5d_{z^2}$ band. Given the large core-hole lifetime of the Ta-L_3 edge, electronic transitions to all these bands get mixed in resonant x-ray scattering measured at the CDW satellites. We really compare the CMW modulation of 1/13 electrons per Ta atom with all the nine un-occupied valences of each atom. The CMW therefore corresponds to a contrast of 0.0085 electrons per Ta atom. This contrast is so tiny that it is virtually an order of magnitude smaller than what was measured in the LBCO experiment.

7.3 Probing Extended Electronic States Using Resonant X-ray Scattering

Using our CDW as an example, we have developed a good understanding about resonant x-ray scattering caused by systems with extended electronic states. At the end of this thesis, I would like to discuss some interesting experiments/ideas that we have been thinking about and will eagerly pursue in the future. By doing so, I hope to show the potential of resonant x-ray scattering as a unique technique of structural study. Resonant x-ray scattering provides a method to study many different problems in a simple and direct way.

7.3.1 The CDW experiments at other edge

As the structural change pertaining to the CDW of $1T$-TaS_2 has long been recognized to be the key characteristic that distinguishes this material from other CDW systems, determining the spatial structural of the CMW is of great scientific importance. Although other techniques such as ultra-low-temperature STM can also be used to measure the CMW, we consider resonant x-ray scattering to be an incomparable tool for it can be done in a straightforward manner. For instance, it is just not possible for the STM to look at Mott localization which is known to happen at 180K. Therefore, we like to continue searching for the right ways of doing things and see if we can eventually make resonant x-ray scattering sensitive to the CMW.

We want Ta to scatter without strong Thomson scattering. This means we have to work at a lower-energy absorption edge. I show in Figure 7.5 the atomic form factor of Ta, with the energies and the core-hole lifetime of the most important

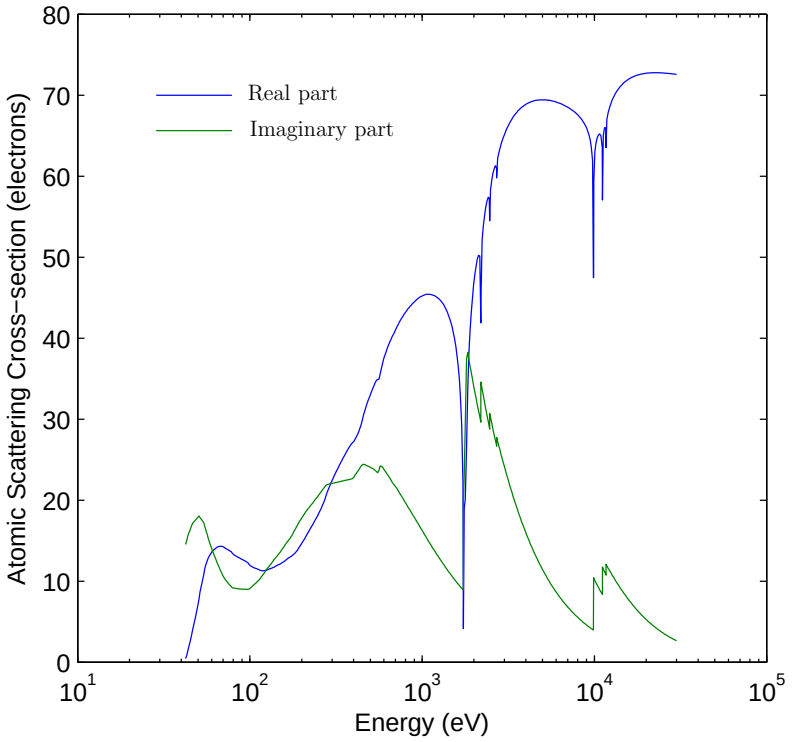

Figure 7.5: The real part and the imaginary part of the atomic form factor of Ta as a function of x-ray energy, assuming $\vec{\mathbf{Q}} = 0$. The Ta-M_5 edge corresponds to a minimum of the real part appearing at 1.735 KeV. This plot is created to show the general trend of the function of the atomic form factor. Detailed structures such as white-lines around the absorption edges are not shown. Reproduced from data found in the CXRO website [2].

Table 7.1: Energies and core-hole lifetime of the Ta absorption edges, reproduced from Ref. [1]. In the third column, numbers that appear in parenthesis are estimated by looking at the corresponding values of Nb, taking into account the size effect.

Edge	Energy (KeV)	Γ (eV)
K	67.416	37.7
L_1	11.682	5.58
L_2	11.136	5.15
L_3	9.881	4.88
M_3	2.194	(> 2)
M_5	1.735	(0.1 – 1)
N_2	0.4634	7.4
N_3	0.4009	5.0

edges listed in Table 7.1. We see there are several different edges below 3 KeV. A simple calculation immediately rejects the N_2 edge and the N_3 edge: At these soft absorption edges, the scattering vector is too short to hit any CDW satellite point in reciprocal space. Nevertheless, we want to work at an edge with a small core-hole lifetime. It seems the M_5 edge is our best choice. At the M_5 edge, transitions that go into the $5d$ conduction bands must be quadrupole transitions. We expect resonant x-ray scattering to have very different properties than those found at the L_3 edge. In terms of the required measurements, we can repeat what we have done in our diffraction experiment and in our absorption experiment. From the absorption spectra, we should be able to determine whether the natural width of the atomic transitions is small enough to resolve the interesting diffraction signal due to the CMW. Specifically, at this lower-energy edge, the real part of the atomic form factor of Ta is small compared to the imaginary part (see Figure 7.5). This means we can probably see resonant peaks rather then resonant dips when

the intensities of the CDW satellites are measured as functions of energy.

In our communication with P. Abbamonte, it was once discussed that we might want to try our experiment at the Ta-M_3 edge. Using our theory presented in this thesis study, I created a simulation and showed that the situation will be very similar to what has been seen at the L_3 edge. As the real part of the atomic form factor of Ta remains larger than the imaginary part, I predict we will see resonant dips in the energy scans. Moreover, diffraction of the CMW will still be difficult to resolve, given the large core-hole lifetime found for the M_3 edge.

7.3.2 Surface charge density waves

We can also use resonant x-ray scattering to look at a completely different type of CDWs called surface charge density waves (SCDWs). For discussion purpose, I will use the SCDW found on a lead-coated germanium surface [7] as an example. See Figure 7.6. On the (111)-surface of germanium crystals, it is discovered that Pb adatoms (1/3 coverage) occupy the T_4 sites, forming a regular hexagonal arrangement. While they all appear equivalent at room-temperature, the Pb adatoms become different if the system is cooled to approximately $-20°$C. In the STM images, one can clearly see that the electronic states show a spatial profile with a (3×3) symmetry. In the low-temperature phase, the Pb-adatom plane is rumpled. The in-plane Pb displacement is of the order of ~ 0.2Å. The characteristic size of the CDW gap can be determined by means of electron energy-loss spectroscopy, and it is determined to be of the order of ~ 65 meV. This CDW phenomenon is commonly referred to as the SCDW of the α-phase Pb/Ge(111).

Physically, the presence of adatoms changes the property of the substrate atoms in resonant x-ray scattering. In surface resonant x-ray scattering experiments [8, 9],

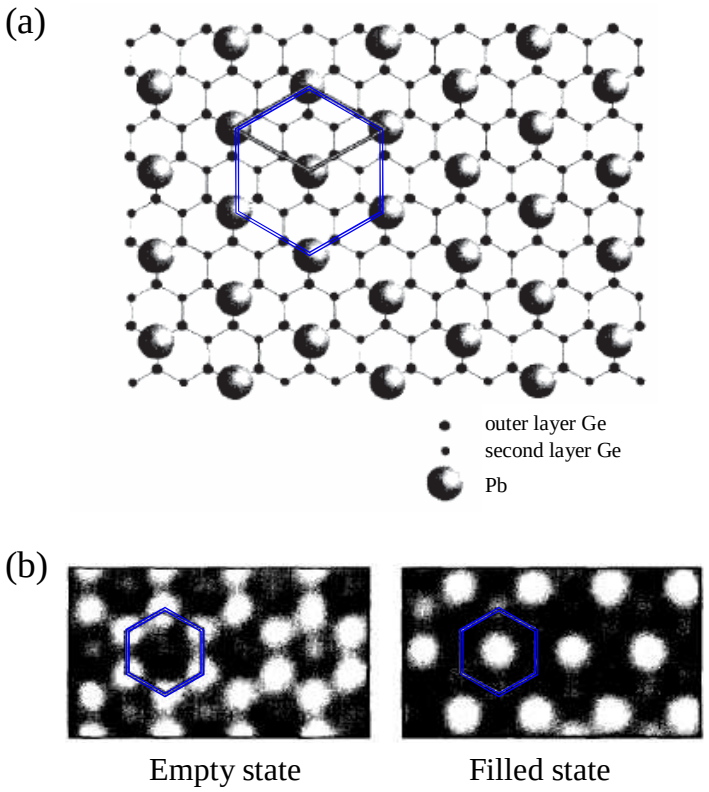

Figure 7.6: (a) Schematic of the α-phase of Pb/Ge(111), which consists of 1/3 monolayer of equivalent Pb adatoms spaced $\sim$ 7Å apart in a hexagonal array of T_4 sites atop the bulk-truncated germanium, with the Pb adatoms forming a clear $(\sqrt{3} \times \sqrt{3})R30°$ arrangement. (b) Low-temperature ($T \approx 60$ K) STM data from the α-phase. The filled-state (empty-state) image was acquired with a negative (positive) sample bias, hence representing the spatial profile of occupied (unoccupied) electronic states at the Pb sites. The blue hexagons are drawn to show the corresponding position in the lattice. Reproduced from Ref. [7]

the effects of O adsorption and of CO adsorption on the (111) surface of platinum crystals has been carefully demonstrated and studied. For the SCDW of the α-phase Pb/Ge(111), I propose to examine Ge absorption edges in resonant x-ray scattering measured at (1/3 1/3 L) in reciprocal space. The idea is simple. I think the Ge beneath Pb adatoms will feel the different electronic structure of the adatoms and scatter differently. Assuming that the Ge substrate does not get reconstructed with the SCDW, only the Pb displacement and the Ge atoms will create x-ray diffraction at the satellite positions. But diffraction of the Pb displacement is featureless at Ge's absorption edges. We can then separate the distorted lattice and the spatial profile of the electronic states in the SCDW based on their different energy dependence in resonant x-ray scattering.

The idea of using Ge to probe the Pb electronic states is not such a wild idea. As long as there is a good coupling between Ge and Pb, I think this method will allow us to detect the electronic states of the SCDW. It relies on the assumption that the Ge substrate does not move with the Pb atoms, which is very similar to the LBCO experiment (Section 7.2.2). There the hole modulation is probed by O, which is assumed to stay fixed in the underlying lattice. In both these experiments, resonant x-ray scattering happens in such a way that it is sensitive to only the contrast of the atomic form factor of the resonating species. Indeed, this is how most experiments have been designed and realized on resonant x-ray scattering.

7.3.3 Surface plasmons

Surface plasmons are collective vibration modes of conduction electrons at the interface between a metal and a insulator [10]. One can think of surface plasmons as some kind of CDW that exist at the surface of a metal, as surface plasmons

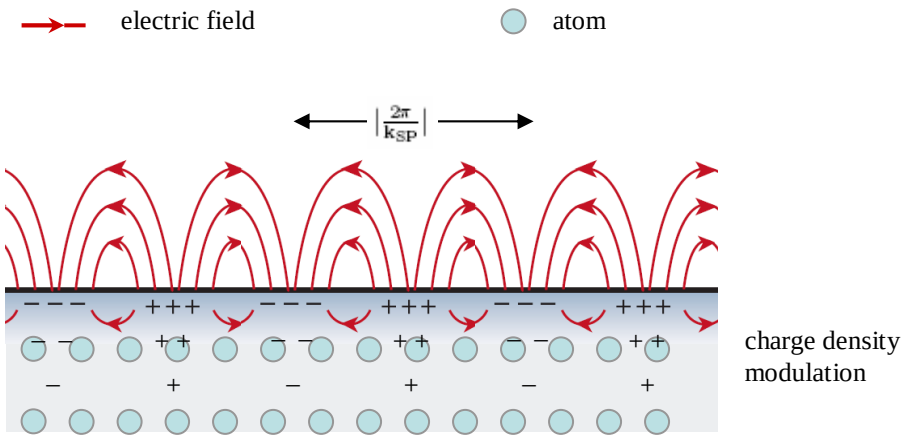

Figure 7.7: In snapshots, a surface plasmon is a simple density modulation of the electron gas inside a metal. The spatial period of the modulation is called the wavelength of the surface plasmon. When the ionic background is included, a surface plasmon can be viewed to be alternating regions with opposite charges. The charge distribution quickly decays with distance from the surface. Typical decay lengths are of the order of $\sim$ 10nm. For atoms staying within the decay length, depending on where they are in the surface plasmon, the number of their valence electrons varies. Being x-ray scatters, they become slightly-different from each other. As our theory of the CDW problem shows, resonant x-ray scattering will be created in accordance with the charge density modulation. There will be satellites created at $\mp\mathbf{k}_{\rm SP}$. Here, $\mathbf{k}_{\rm SP}$ is the wavevector of the surface plasmon.

are also fluctuations in the electron density surrounding the metal lattice sites. However, surface plasmons and CDWs are independent physical phenomena. Surface plasmons are not static; they propagate and get attenuated along the metal surface. The wavevector of surface plasmons is a continuous variable. Last but not least, surface plasmons do not cause lattice distortions.

Here I would like to argue that surface plasmons could be interesting to resonant x-ray scattering, in the sense that surface plasmons can have very interesting spatial structures in metals. Inside today's optical devices, techniques based on surface plasmons have gained a unique position for surface plasmons is an essential component to control/manipulate light on a subwavelength length scale. In those applications, one of the key problems is how surface plasmons are actually distributed in a specific optical component. In practice, one will usually have to measure the photons emitted by surface plasmons, and then compare the observed photon field with theoretical simulations to get the structure of surface plasmons. Methods like this are not simple. It will be nice if we can find some other methods so surface plasmons can be studied more directly.

In Figure 7.7, I explain the idea of using resonant x-ray scattering to measure the spatial structure of surface plasmons. In principle, it will be very similar to our experiment of the CDW. But because surface plasmons involve no lattice distortion, the size and the shape of the satellites will be a direct measure of the structure of the surface plasmons.

It needs to be pointed out that in an surface plasmon experiment, the characteristic length will be very different from the characteristic length in a CDW experiment. While most CDWs have their wavelengths $\preceq$ 1nm, wavelengths of surface plasmons are usually in the order of 1000 nm. Should there be any satellite being created in resonant x-ray scattering, they will therefore be very close

to Bragg reflections in the reciprocal space. To properly resolve the satellites, a good **Q**-resolution is necessary. In this aspect, I think the experiment should be performed at some low-enough energies and look at satellites that appear around the origin $\mathbf{Q} = 0$.

7.3.4 Image charges

Imagine we can bring a conductor very close to a piece of $1T$-TaS_2. Under the influence of the CDW, electrons inside the conductor will get redistributed until an electrostatic equilibrium is finally reached. If the distance between the two objects is very short, the charges will have the similar arrangement as the CDW. We will have a charge image which reflects the spatial order of the CMW on the surface of the conductor. The image is essentially a charge density modulation, something that we have been arguing is visible in resonant x-ray scattering. This will be a very interesting experiment that we may try in the future.

There are two big concepts in the proposed experiment about image charges. First, we want to set up a diffraction experiment to look at resonant x-ray scattering from the conductor, rather than the CDW. Just like our discussion of the SCDW (Section 7.2.2), if we assume the lattice of the conductor retains its perfect order, we will see only the CMW in diffraction. In other words, we immediately solve the problem about separating the CMW from the LDW. Second, the use of the conductor allows us to disengage the x-ray study from the sample properties. In principle, we can look at anything that creates image charges inside the "mirror" (the conductor). For instance, the "object" can be a charged nano-scaled capacitor array created by today's semiconductor technology. Additionally, the diffraction experiment itself does not need to be re-define every time we try a different sam-

ple. This image-charge method can become a standard technique of mapping out interesting charge density modulations in completely different systems.

BIBLIOGRAPHY

[1] J. C. Fuggle and J. E. Inglesfield. *Unoccupied electronic states : fundamentals for XANES, EELS, IPS and BIS*, volume 69, chapter Appendix B: Core-Hole Lifetime Broadening, pages 347–351. Springer, Berlin, 1992.

[2] Lawrence Berkeley National Laboratory Center for X-Ray Optics. X-ray interactions with matter. Internet resource at http://henke.lbl.gov/optical_constants/asf.html. The Atomic Scattering Factor Files.

[3] Doon Gibbs, D. R. Harshman, E. D. Isaacs, D. B. McWhan, D. Mills, and C. Vettier. Polarization and Resonance Properties of Magnetic X-Ray Scattering in Holmium. *Phys. Rev. Lett.*, 61(10):1241–1244, Sep 1988.

[4] J. P. Hannon, G. T. Trammell, M. Blume, and Doon Gibbs. X-Ray Resonance Exchange Scattering. *Phys. Rev. Lett.*, 61(10):1245–1248, Sep 1988.

[5] P. Abbamonte, A. Rusydi, S. Smadici, G. D. Gu, G. A. Sawatzky, and D. L. Feng. Spatially modulated 'Mottness' in $L_{2-x}B_xCO_4$. *Nature Physics*, 1:155–158, dec 2005.

[6] A. R. Moodenbaugh, Youwen Xu, M. Suenaga, T. J. Folkerts, and R. N. Shelton. Superconducting properties of $L_{2-x}B_xCO_4$. *Phys. Rev. B*, 38(7):4596–4600, Sep 1988.

[7] J.M. Carpinelli, H.H. Weitering, E.W. Plummer, and R. Stumpf. Direct observation of a surface charge density wave. *Nature*, 381:398–400, may 1996.

[8] Y. S. Chu, H. You, J. A. Tanzer, T. E. Lister, and Z. Nagy. Surface Resonance X-Ray Scattering Observation of Core-Electron Binding-Energy Shifts of Pt(111)-Surface Atoms during Electrochemical Oxidation. *Phys. Rev. Lett.*, 83(3):552–555, Jul 1999.

[9] A. Menzel, K.-C. Chang, V. Komanicky, Y. V. Tolmachev, A. V. Tkachuk, Y. S. Chu, and H. You. High-density electrosorbed carbon monoxide monolayers on Pt(111) under atmospheric pressure. *Phys. Rev. B*, 75:035426.

[10] William L. Barnes, A. Dereux, and Thomas W. Ebbesen. Surface plasmon subwavelength optics. *Nature*, 424:824–830, Aug 2003.

APPENDIX A

THE QUANTUM THEORY OF X-RAY SCATTERING

Indeed, reviews of the quantum mechanical theory of x-ray scattering can be found in many references [1, 2, 3, 4]. Those discussions, with their emphases on different theoretical aspects, are subject to various assumptions and/or approximations. To fully appreciate the theory, we ought to derive the theory using our own language. By getting exposed to the formalism, we clear up several important concepts in the quantum mechanical theory.

The Hamiltonian

As in many other quantum mechanical problems, we must first specify the Hamiltonian. Scattering happens when waves hit an object, causing some secondary waves propagating with different polarizations and wavevectors. In the problem we are dealing with here, x-ray will be the wave, and the object can be an isolated atom or as big as a macroscopic solid. Given that scattering happens because electrons and photons (quantized x-ray) interact with each other, scattering is described by the Hamiltonian:

$$\mathcal{H} = \sum_j \frac{[\mathbf{p}_j + e\mathbf{A}(\mathbf{r}_j, t)]^2}{2m_e} + \sum_j U(\mathbf{r}_j) + \sum_u \sum_{\mathbf{l}} \hbar\omega_{\mathbf{l}} \hat{a}^\dagger_{u\mathbf{l}} \hat{a}_{u\mathbf{l}} \tag{A.1}$$

For this Hamiltonian, we give our interpretation as follows: The first two terms are the kinetic energy and the potential energy of electrons, respectively, whereas the last term represents the energy stored in the photon field. For the electrons, $\mathbf{p}_j$ ($\mathbf{r}_j$) is the momentum (position) of the jth electron, and U is the potential. For x-ray, u is the polarization index, $\mathbf{l}$ is the wavevector, and $\hat{a}^\dagger$ ($\hat{a}$) is the creation (annihilation) operator of photons. The coupling between the electrons and the photons

occurs through $\mathbf{A}$— the vector potential of x-ray. Using second quantization, one can write the vector potential in the operator form

$$\mathbf{A}(\mathbf{r},t)=\sum_{u}\sum_{\mathbf{l}}\hat{\mathrm{e}}^{u}\Big(\frac{\hbar}{2\varepsilon_0 V\omega_{\mathbf{l}}}\Big)^{\frac{1}{2}}\Big[\hat{a}_{u\mathbf{l}}e^{i(\mathbf{l}\cdot\mathbf{r}-\omega t)}+\hat{a}^{\dagger}_{u\mathbf{l}}e^{-i(\mathbf{l}\cdot\mathbf{r}-\omega t)}\Big] \tag{A.2}$$

where $\hat{\mathrm{e}}^{u}$ is the polarization vector. Rearranging Eq (A.1) we obtain

$$\mathcal{H}=\sum_{j}\Big(\frac{\mathbf{p}_j^2}{2m_e}+U(\mathbf{r}_j)\Big)+\sum_{u}\sum_{\mathbf{l}}\hbar\omega_{\mathbf{l}}\hat{a}^{\dagger}_{u\mathbf{l}}\hat{a}_{u\mathbf{l}}+\sum_{j}\Big[\frac{e^2}{2m_e}\mathbf{A}^2+\frac{e}{m_e}\mathbf{A}\cdot\mathbf{p}_j\Big] \tag{A.3}$$

where terms involving the vector potential have been deliberately grouped and separated from the rest of the Hamiltonian. The smallness of the electron charge means we can treat the vector potential as perturbations in the Hamiltonian. The "unperturbed" Hamiltonian is the sum of the energy of the electrons and the energy stored in the photon field. Correspondingly the state vectors of the electron-photon system will be *direct products* [1] of the state vectors for the electron eigenstates and the state vectors for the photon eigenstates.

Quantum states and operators

We want to use Eq (A.3) to determine how elastic x-ray scattering is created by atomic electrons. Due to the time dependence of the vector potential, electrons will oscillate in the x-ray field [5]. We will assume that corresponding transitions of the jth electron take place between a core-level state $|s\rangle$ and a high energy state $|n\rangle$. For x-ray, we use wavevectors and polarizations to specify the modes of photons. Without losing generality, we can assume that incident x-ray ($\mathbf{l}=\mathbf{q}$) and scattered x-ray ($\mathbf{l}=\mathbf{q}'$) both have the form of plane waves[1]. For the incident (scattered) wave, $\hat{\mathrm{e}}^{\alpha}$ ($\hat{\mathrm{e}}^{\beta}$) is the polarization and $n_{\alpha,\mathbf{q}}$ ($n_{\beta,\mathbf{q}'}$) is the number of photons appearing in this specific mode. As photons appear in only the two modes, the photon

[1]For experiments that are performed with synchrotron radiation source, the incident x-ray is pluses rather than continuous plane waves. One can then superimpose the plane wave states to construct the proper photon mode.

eigenstates can be denoted by the occupation numbers as $|n_{\alpha,\mathbf{q}}; n_{\beta,\mathbf{q}'}\rangle$. In the event of scattering, the occupation numbers changes so that one photon is removed from the incident mode $|n_{\alpha,\mathbf{q}}\rangle$, and one photon added to the scattering mode $|n_{\beta,\mathbf{q}'}\rangle$. For discussion purposes, we will assume the photon eigenstates $|n_{\alpha,\mathbf{q}}; n_{\beta,\mathbf{q}'}\rangle$ are $|1;0\rangle$ before the scattering event, and $|0;1\rangle$ after the scattering event.

As far as the operators are concerned, our assumption of two photon modes allows us to write the vector potential explicitly

$$\mathbf{A}(\mathbf{r}_j, t) = \left(\mathrm{A}_{\mathbf{q}} e^{-i\omega t}\hat{a}_{\alpha\mathbf{q}} + \mathrm{A}^{\dagger}_{\mathbf{q}} e^{i\omega t}\hat{a}^{\dagger}_{\alpha\mathbf{q}}\right) + \left(\mathrm{A}_{\mathbf{q}'} e^{-i\omega t}\hat{a}_{\beta\mathbf{q}'} + \mathrm{A}^{\dagger}_{\mathbf{q}'} e^{i\omega t}\hat{a}^{\dagger}_{\beta\mathbf{q}'}\right) \tag{A.4}$$

where we have used A and $\mathrm{A}^{\dagger}$ to denote the time-independent parts of the plane waves. For the incident wave,

$$\mathrm{A}_{\mathbf{q}} = \left(\frac{\hbar}{2\varepsilon_0 V\omega}\right)^{\frac{1}{2}} (e^{i\mathbf{q}\cdot\mathbf{r}_j})\hat{\mathrm{e}}^{\alpha} \qquad \text{and} \qquad \mathrm{A}^{\dagger}_{\mathbf{q}} = \left(\frac{\hbar}{2\varepsilon_0 V\omega}\right)^{\frac{1}{2}} (e^{-i\mathbf{q}'\cdot\mathbf{r}_j})\hat{\mathrm{e}}^{\alpha} \tag{A.5}$$

Similar expressions of $\mathrm{A}_{\mathbf{q}'}$ and $\mathrm{A}^{\dagger}_{\mathbf{q}'}$ can also be written for the scattered wave. (Keep in mind that scattering has the different polarization $\hat{\mathrm{e}}^{\beta}$.) Using this operator form of vector potential, we will determine how scattering is created based on the perturbed Hamiltonian Eq (A.3).

In due course we will have to use Fermi's golden rule to determine the cross-section of x-ray scattering. In Fermi's golden rule, the key ingredient is the transition matrix elements of the perturbations in the Hamiltonian. In the time-dependent perturbation theory, those terms $\dfrac{e^2}{2m_e}\mathbf{A}^2$ and $\dfrac{e}{m_e}\mathbf{A}\cdot\mathbf{p}_j$ appearing in Eq (A.3) correspond to different scattering processes. We will familiarize ourselves with the important difference.

Time-dependent perturbation theory

From the time-dependent perturbation theory, it is known that transition matrix

elements can be computed to first order to get the transition amplitudes by enclosing the time-independent perturbations with a ket state and a bra state. The condition of elastic scattering requires that the ket state and the bra state are constructed by the same initial state $|s\rangle$. For $\frac{e}{m_e}\mathbf{A}\cdot\mathbf{p}_j$, this means

$$\langle 0;1|\langle s|\frac{e}{m_e}\mathbf{A}(\mathbf{r}_j,0)\cdot\mathbf{p}_j|s\rangle|1;0\rangle = \frac{e}{m_e}\langle 0;1|\mathbf{A}(\mathbf{r}_j,0)|1;0\rangle\cdot\langle s|\mathbf{p}_j|s\rangle = 0 \qquad \text{(A.6)}$$

The final equality holds for two reasons. First, projecting $|1;0\rangle$ onto $|0;1\rangle$ through $\mathbf{A}(\mathbf{r}_j,0)$ should always give a zero because the vector potential is linear in the creation/annihilation operators. Also, the second matrix vanishes because $\mathbf{p}_j$ changes the parity for the electron eigenstate. Hence $\frac{e}{m_e}\mathbf{A}\cdot\mathbf{p}_j$ does not correspond to scattering in first order. In fact, as we must point out, $\frac{e}{m_e}\mathbf{A}\cdot\mathbf{p}_j$ is the perturbation that leads to photoelectric absorption in the perturbation theory computed to first order.

Besides $\frac{e}{m_e}\mathbf{A}\cdot\mathbf{p}_j$, there is also $\frac{e^2}{2m_e}\mathbf{A}^2$ appearing in the Hamiltonian. In the time-dependent perturbation theory, this term too should be taken into account to evaluate the transition amplitude. When the vector potential is squared, it produces eight different cross terms in the creation and the annihilation operators. Two of them have the right forms of either $(\hat{a}_{\alpha\mathbf{q}}\hat{a}^\dagger_{\beta\mathbf{q}'})$ or $(\hat{a}^\dagger_{\beta\mathbf{q}'}\hat{a}_{\alpha\mathbf{q}})$, and they are responsible for x-ray scattering, given that their effect is to subtract a photon from $|n_{\alpha,\mathbf{q}}\rangle$ and add another one to $|n_{\beta,\mathbf{q}'}\rangle$. One can repeat the calculation and verify

$$\begin{aligned} c^{(1)}_{\mathbf{A}\cdot\mathbf{A}} &= \langle 0;1|\langle s|\frac{e^2}{2m_e}\mathbf{A}(\mathbf{r}_j,0)\cdot\mathbf{A}(\mathbf{r}_j,0)|s\rangle|1;0\rangle \\ &= \langle s|\frac{e^2}{2m_e}\mathrm{A}_{\mathbf{q}}\cdot\mathrm{A}^\dagger_{\mathbf{q}'}|s\rangle\langle 0;1|\hat{a}_{\alpha\mathbf{q}}\hat{a}^\dagger_{\beta\mathbf{q}'}+\hat{a}^\dagger_{\beta\mathbf{q}'}\hat{a}_{\alpha\mathbf{q}}|1;0\rangle \\ &= \frac{e^2\hbar}{2m_e\varepsilon_0 V\omega}(\hat{\mathrm{e}}^\alpha\cdot\hat{\mathrm{e}}^\beta)\langle s|e^{-i\mathbf{Q}\cdot\mathbf{r}_j}|s\rangle \end{aligned} \qquad \text{(A.7)}$$

where we have used Eq (A.5) for the definitions of $\mathrm{A}_{\mathbf{q}}$ and $\mathrm{A}^\dagger_{\mathbf{q}'}$, and $\mathbf{Q}\equiv\mathbf{q}'-\mathbf{q}$ is the scattering vector. In this equation, the matrix element appearing in the final result is nothing but a fourier transform of the density of the electronic state $|s\rangle$.

It is evident that $c^{(1)}_{\mathbf{A}\cdot\mathbf{A}}$ is the transition amplitude for Thomson scattering.

Given that there are photoelectric absorption as well as Thomson scattering in the perturbation theory, we recognize that the first-order expansion of the transition matrix elements can not be the full story of x-ray scattering. In optics, we have the known fact that absorption, as a form of dissipation, exists aside from dispersion of light. The anticipated correspondence will not be seen in quantum mechanics until the time-dependent perturbation theory is computed to second order. In second order, scattering results from $\frac{e}{m_e}\mathbf{A}\cdot\mathbf{p}_j$, but this time the perturbation must act twice in order to take effect. Let us describe how it can happen in time. The first action which happens at t_1 can either annihilate the photon in $|n_{\alpha,\mathbf{q}}\rangle$ or create a photon in $|n_{\beta,\mathbf{q}'}\rangle$. When the second action which happens at t_2, it must create a photon in $|n_{\beta,\mathbf{q}'}\rangle$ if that photon has not be created. Otherwise there will be no scattering. On the other hand, if scattering has already been created but the photon in $|n_{\alpha,\mathbf{q}}\rangle$ has not yet been annihilated, the second action must take care of that photon and annihilate it. Between t_1 and t_2 the electron is promoted to a high energy state $|n\rangle$. When the entire system (electrons plus photons) is concerned , there are two types of intermediate states. In the first type, the jth electron is in $|n\rangle$, and no photons are present. The state vector is $|n\rangle|0;0\rangle$. In the second type, the electron is also in $|n\rangle$, but there is one photon in each photon mode. The state vector is therefore $|n\rangle|1;1\rangle$. In general, $|n\rangle$ can be any unoccupied state of the electron system.

Without really proving it, we will write down the transition amplitudes of these second-order scattering processes based on what we just described. In the case where there are no photons present in the intermediate state, the transition

amplitude is

$$d^{(2)}_{|0;0\rangle} = \Big(\frac{e}{m_e}\Big)^2 \sum_n \frac{\langle 0;1|\langle s|\mathrm{A}^\dagger_{\mathbf{q}'}\cdot\mathbf{p}_j\hat{a}^\dagger_{\beta\mathbf{q}'}|n\rangle|0;0\rangle\langle 0;0|\langle n|\mathrm{A}_{\mathbf{q}}\cdot\mathbf{p}_j\hat{a}_{\alpha\mathbf{q}}|s\rangle|1;0\rangle}{\hbar(\omega-\omega_{ns})+i\frac{\Gamma_s}{2}}$$
$$= \Big(\frac{e}{m_e}\Big)^2 \sum_n \frac{\langle s|\mathrm{A}^\dagger_{\mathbf{q}'}\cdot\mathbf{p}_j|n\rangle\langle n|\mathrm{A}_{\mathbf{q}}\cdot\mathbf{p}_j|s\rangle}{\hbar(\omega-\omega_{ns})+i\frac{\Gamma_s}{2}} \tag{A.8}$$

On the other hand, if there are two photons appearing in the intermediate state, the transition amplitude is given by

$$d^{(2)}_{|1;1\rangle} = -\Big(\frac{e}{m_e}\Big)^2 \sum_n \frac{\langle 0;1|\langle s|\mathrm{A}_{\mathbf{q}}\cdot\mathbf{p}_j\hat{a}_{\alpha\mathbf{q}}|n\rangle|1;1\rangle\langle 1;1|\langle n|\mathrm{A}^\dagger_{\mathbf{q}'}\cdot\mathbf{p}_j\hat{a}^\dagger_{\beta\mathbf{q}'}|s\rangle|1;0\rangle}{\hbar(\omega+\omega_{ns})+i\frac{\Gamma_s}{2}}$$
$$= -\Big(\frac{e}{m_e}\Big)^2 \sum_n \frac{\langle s|\mathrm{A}_{\mathbf{q}}\cdot\mathbf{p}_j|n\rangle\langle n|\mathrm{A}^\dagger_{\mathbf{q}'}\cdot\mathbf{p}_j|s\rangle}{\hbar(\omega+\omega_{ns})+i\frac{\Gamma_s}{2}} \tag{A.9}$$

Interested readers are referred to the standard textbook [1] for how these results are obtained in the perturbation theory[2]. As transition amplitudes are additive, we will add $d^{(2)}_{|0;0\rangle}$ and $d^{(2)}_{|1;1\rangle}$ together

$$c^{(2)}_{\mathbf{A}\cdot\mathbf{p}} = d^{(2)}_{|0;0\rangle} + d^{(2)}_{|1;1\rangle}$$
$$= \Big(\frac{e}{m_e}\Big)^2 \sum_n \Big(\frac{\langle s|\mathrm{A}^\dagger_{\mathbf{q}'}\cdot\mathbf{p}_j|n\rangle\langle n|\mathrm{A}_{\mathbf{q}}\cdot\mathbf{p}_j|s\rangle}{\hbar(\omega-\omega_{ns})+i\frac{\Gamma_s}{2}} - \frac{\langle s|\mathrm{A}_{\mathbf{q}}\cdot\mathbf{p}_j|n\rangle\langle n|\mathrm{A}^\dagger_{\mathbf{q}'}\cdot\mathbf{p}_j|s\rangle}{\hbar(\omega+\omega_{ns})+i\frac{\Gamma_s}{2}}\Big)$$
$$= \frac{e^2\hbar}{2m_e^2\varepsilon_0 V\omega}\sum_n \Big(\frac{\langle s|O^{\beta\dagger}(\mathbf{q}')|n\rangle\langle n|O^\alpha(\mathbf{q})|s\rangle}{\hbar(\omega-\omega_{ns})+i\frac{\Gamma_s}{2}} - \frac{\langle s|O^\alpha(\mathbf{q})|n\rangle\langle n|O^{\beta\dagger}(\mathbf{q}')|s\rangle}{\hbar(\omega+\omega_{ns})+i\frac{\Gamma_s}{2}}\Big) \tag{A.10}$$

where we have used $O^\alpha(\mathbf{q}) = \mathbf{p}_j\cdot\hat{\mathrm{e}}^\alpha\, e^{i\mathbf{q}\cdot\mathbf{r}_j}$ as a convenient shorthand. Comparing $c^{(2)}_{\mathbf{A}\cdot\mathbf{p}}$ with $c^{(1)}_{\mathbf{A}\cdot\mathbf{A}}$ computed in Eq (A.7), we find they are of the same order of magnitude. In summary, in the time-dependent perturbation theory, Eq (A.10) is the transition amplitude for elastic scattering computed to second order.

Fermi's Golden Rule

Using the transition amplitudes we can calculate the scattering cross-section. We

[2]In both Eq (A.8) and Eq (A.9), we have included $i\Gamma_s/2$ in the denominators to account for the effect of finite lifetimes associated with the intermediate states. For Γ_s, the subscript is used to indicate its dependence on the initial state $|s\rangle$. It is also worth pointing out that the signs of these imaginary numbers need to be consistent so causality is not violated.

will first have to determine the transition rate W, with which the incident wave is converted to scattering. According to Fermi's Golden Rule, W is proportional to $\varrho^{\gamma}(E)\Delta\Omega$, where ϱ^{γ} is the density of state corresponding to the final state of x-ray, and $\Delta\Omega$ is the solid angle centered on $\mathbf{q}'$— the wavevector of scattering. Fermi's Golden Rule states that

$$W_{\Delta\Omega} = \frac{2\pi}{\hbar}\left|c^{(1)}_{\mathbf{A}\cdot\mathbf{A}} + c^{(2)}_{\mathbf{A}\cdot\mathbf{p}}\right|^2 \varrho^{\gamma}(E)\Delta\Omega \tag{A.11}$$

Recall the definition that $\varrho^{\gamma}(E)dE$ is the number of photon states between E and $E + \Delta E$ in the phase space. It follows that

$$\varrho^{\gamma}(E) = \Big(\frac{V}{8\pi^3}\Big)\Big(\frac{1}{\hbar^3 c^3}\Big)E^2 \tag{A.12}$$

The (differential) scattering cross-section can immediately be calculated

$$(\frac{d\sigma}{d\Omega}) = \lim_{\Delta\Omega\to 0}\frac{W_{\Delta\Omega}V}{c\Delta\Omega} = \Big(\frac{V}{2\pi}\Big)^2(\frac{\omega^2}{\hbar^2 c^4})\left|c^{(1)}_{\mathbf{A}\cdot\mathbf{A}} + c^{(2)}_{\mathbf{A}\cdot\mathbf{p}}\right|^2 \tag{A.13}$$

Plugging our results for the transition amplitudes, we find the scattering cross-section can be expressed as follows

$$\begin{aligned}\Big(\frac{d\sigma}{d\Omega}\Big)_e = r_0^2 \Big|&(\hat{\mathrm{e}}^{\alpha}\cdot\hat{\mathrm{e}}^{\beta})\langle s|\, e^{-i\mathbf{Q}\cdot\mathbf{r}_s}\,|s\rangle \\ &+\frac{1}{m_e}\sum_n\Big(\frac{\langle s|O^{\beta\dagger}(\mathbf{q}')|n\rangle\langle n|O^{\alpha}(\mathbf{q})|s\rangle}{\hbar(\omega-\omega_{ns})+i\frac{\Gamma_s}{2}} - \frac{\langle s|O^{\alpha}(\mathbf{q})|n\rangle\langle n|O^{\beta\dagger}(\mathbf{q}')|s\rangle}{\hbar(\omega+\omega_{ns})+i\frac{\Gamma_s}{2}}\Big)\Big|^2\end{aligned} \tag{A.14}$$

where we have rewritten the overall prefactor using the classical electron radius r_0. As it has been clearly said in the derivation, Eq (A.14) is the scattering cross-section for a single atomic electron. Given that $\hbar\omega_{ns}$ is much greater than Γ_s for most atomic transitions, it is frequent that one will talk about only a single Γ_s in an atom as well as completely ignore this imaginary number in the denominator of the second term appearing inside the big parenthesis. In any case, Eq (A.14) shows that the cross-section is energy-dependent, and this must happen because of the very existence of $c^{(2)}_{\mathbf{A}\cdot\mathbf{p}}$.

By carefully going through the derivation, we expose ourselves to the essential ideas used in the quantum theory of x-ray scattering. Not only we can now write the theory correctly, but we can then determine how approximations should be made so the applications will remain self-consistent. For instance, it is known that in the so-called dipole-dipole approximation, one will replace the operator $O^{\alpha}(\mathbf{q}) = \mathbf{p}_j \cdot \hat{\mathrm{e}}^{\alpha}\, e^{i\mathbf{q}\cdot\mathbf{r}_j}$ in Eq (A.11) by $O^{\alpha}(\mathbf{q}) \sim \mathbf{p}_j \cdot \hat{\mathrm{e}}^{\alpha}$. This approximation completely ignores the spatial components of $\mathrm{A}^{\dagger}_{\mathbf{q}'}$ and of $\mathrm{A}_{\mathbf{q}}$, and will inescapably result in a transition matrix amplitude $c^{(1)}_{\mathbf{A}\cdot\mathbf{A}}$ without any $\mathbf{Q}$-dependence (See Eq (A.7)). When it comes to form the scattering cross-section of an atom, this means the atomic form factor will *not* decay with the wavevector, which is certainly not realistic. Therefore, while it seems to be a commonly-accepted statement found in many different textbooks, I think it is improper to assume that we can always divide an atomic form factor into a $\mathbf{Q}$-dependent-only part plus a $\mathbf{Q}$-independent dispersion correction.

APPENDIX B

CDW SATELLITES AND THEIR STRUCTURES

In Chapter 4 I claimed that diffraction of the CMW can be measured independently at the primary CDW satellites. That statement, indeed, was made without proof. Additionally, as I did argue that spatial structure of the CMW may become different from that of the LDW, we have not yet talked about how structural information of the CMW can be extracted by doing resonant x-ray scattering. This chapter is created to give those questions a comprehensive discussion.

Proof of Eq (4.8)

In Section 4.1.1, I showed that the cross-section of a CDW without the LDW component can be written as

$$\Big(\frac{d\sigma}{d\Omega}\Big)_{\mathrm{CMW},\alpha\beta} = r_0^2 \Big| \sum_{\mathbf{R}} e^{-i\mathbf{Q}\cdot\mathbf{R}} \Big(f_{\alpha\beta}(\mathbf{Q},\omega) + \tilde{f}_{\alpha\beta}(\omega)\cos(\mathbf{k}_{\mathrm{CDW}}\cdot\mathbf{R}) \Big) \Big|^2 \tag{B.1}$$

Here, let us explain how this cross-section should be evaluated around the CDW satellites and around the Bragg peak positions. To do so, we must realize that

$$\Big| \sum_{\mathbf{R}} e^{-i\mathbf{Q}\cdot\mathbf{R}} \Big(f + \tilde{f}\cos(\mathbf{k}_{\mathrm{CDW}}\cdot\mathbf{R}) \Big) \Big|^2 = \overline{\sum_{\mathbf{R}} e^{-i\mathbf{Q}\cdot\mathbf{R}} \Big(f + \tilde{f}\cos(\mathbf{k}_{\mathrm{CDW}}\cdot\mathbf{R}') \Big)} \cdot \sum_{\mathbf{R}'} e^{-i\mathbf{Q}\cdot\mathbf{R}'} \Big(f + \tilde{f}\cos(\mathbf{k}_{\mathrm{CDW}}\cdot\mathbf{R}') \Big) \tag{B.2}$$

In other words, when the square of the lattice sum is evaluated, the lattice sum must be computed before the multiplication. We have two independent lattice sums, and $\mathbf{R}'$ is introduced to address the point[1]. To simplify the equation, we have dropped the subscript $\alpha\beta$ for polarizations.

To proceed, let us play a common trick and rewrite the cosine functions using

[1] Ultimately, this is how *two-point correlations* arise in x-ray scattering. We will see the reason shortly

$\cos(\mathbf{k}_{\rm CDW}\cdot\mathbf{R}) = (1/2)(e^{i\mathbf{k}_{\rm CDW}\cdot\mathbf{R}} + e^{-i\mathbf{k}_{\rm CDW}\cdot\mathbf{R}})$. Do the substitutions. And we will find out

$$\begin{aligned}
&\overline{\sum_{\mathbf{R}} e^{-i\mathbf{Q}\cdot\mathbf{R}}\Big(f+\tilde{f}\cos(\mathbf{k}_{\rm CDW}\cdot\mathbf{R}')\Big)}\cdot\sum_{\mathbf{R}'} e^{-i\mathbf{Q}\cdot\mathbf{R}'}\Big(f+\tilde{f}\cos(\mathbf{k}_{\rm CDW}\cdot\mathbf{R}')\Big)\\
&\quad=\sum_{\mathbf{R}\mathbf{R}'} e^{i\mathbf{Q}\cdot(\mathbf{R}-\mathbf{R}')}\Big(\overline{f}+\overline{(\tilde{f}/2)}(e^{-i\mathbf{k}_{\rm CDW}\cdot\mathbf{R}}+e^{i\mathbf{k}_{\rm CDW}\cdot\mathbf{R}})\Big)\\
&\qquad\qquad\times\Big(f+(\tilde{f}/2)(e^{i\mathbf{k}_{\rm CDW}\cdot\mathbf{R}'}+e^{-i\mathbf{k}_{\rm CDW}\cdot\mathbf{R}'})\Big)\\
&\quad=\sum_{\mathbf{R}\mathbf{R}'} e^{i\mathbf{Q}\cdot(\mathbf{R}-\mathbf{R}')}\Big(|\,f|^2+\frac{1}{4}|\,\tilde{f}\,|^2(e^{i\mathbf{k}_{\rm CDW}\cdot(\mathbf{R}-\mathbf{R}')}+e^{-i\mathbf{k}_{\rm CDW}\cdot(\mathbf{R}-\mathbf{R}')})\Big)\\
&\quad=N\Big\langle\sum_{\mathbf{R}} e^{i\mathbf{Q}\cdot(\mathbf{R}-\mathbf{R}_0)}\Big(|\,f|^2+\frac{1}{4}|\,\tilde{f}\,|^2(e^{i\mathbf{k}_{\rm CDW}\cdot(\mathbf{R}-\mathbf{R}_0)}+e^{-i\mathbf{k}_{\rm CDW}\cdot(\mathbf{R}-\mathbf{R}_0)})\Big)\Big\rangle \qquad \text{(B.3)}
\end{aligned}$$

The important physical concept appears in the final equality. We assume that the CMW corresponds to a translational invariance inside the lattice. Hence the system is an ensemble of the CMW position with respect to an arbitrarily-chosen point $\mathbf{R}_0$, and $\langle\ \ \rangle$ is an average over all $\mathbf{R}_0$. Since no fluctuations have been included in the system, the average is currently unnecessary. Using this result in Eq (B.1), we are readily to obtain Eq (4.8).

The two-point phase-phase correlation

Fluctuations can be realized through CDW phases. Let us explain the physical significance of the CDW phase fluctuations. CDWs are characterized by their order parameters, which can generally be expressed as $\Delta(\mathbf{r}) = \Delta_0 e^{i\phi}$, and Δ_0 and ϕ are the amplitude and the phase in an order parameter, respectively. In general, Δ_0 and ϕ can both be functions of position $\mathbf{r}$. For any given CDW, the correlation of its order parameter measures the changes in the spatial structure. Yet at sufficiently low temperatures, fluctuations of Δ_0 are negligible. The correlation essentially becomes a correlation between the phases at two points:

$$\langle\overline{\Delta(\mathbf{r}_1)}\Delta(\mathbf{r}_2)\rangle = |\Delta_0|^2\langle e^{-i[\phi(\mathbf{r}_1)-\phi(\mathbf{r}_2)]}\rangle = |\Delta_0|^2 e^{-\frac{1}{2}\langle[\phi(\mathbf{r}_1)-\phi(\mathbf{r}_2)]^2\rangle} \qquad \text{(B.4)}$$

where in the final equality we have used the Baker-Hausdorff theorem[2]. Only if the CDW phase stay the same throughout the entire crystal, $\langle\overline{\Delta(\mathbf{r}_1)}\Delta(\mathbf{r}_2)\rangle$ can be a constant. Any fluctuations in the phase mean that the correlation will decay with increasing distance $|\mathbf{r}_2 - \mathbf{r}_1|$.

As we have explained in the introductory chapter, the phase of the CMW (ϕ_E) and the phase of the LDW (ϕ_L) can actually become independent variables when a CDW is not found in the ground state. Should the CMW and the LDW correspond to different spatial structures, we expect there will be two different phase correlations

$$\langle\,[\phi_E(r_1) - \phi_E(r_2)]^2\,\rangle \equiv \mathcal{G}_E(r_1, r_2) \tag{B.6}$$

$$\langle\,[\phi_L(r_1) - \phi_L(r_2)]^2\,\rangle \equiv \mathcal{G}_L(r_1, r_2) \tag{B.7}$$

each of which is defined for the CMW and for the LDW, respectively. Can these two different phase correlations be measured experimentally?

In x-ray diffraction experiments, it is well known that diffuse scattering arises as a consequence of finite correlations [6]. By measuring diffuse scattering around the CDW satellites, our group has shown that the phase correlation of a LDW can be extracted using conventional x-ray scattering technique [7, 8]. In principle, one should be able to determine the phase correlation of a CMW by using resonant x-ray scattering. I will describe the theory in the following.

Structures of CDW satellites

When good phase correlations are lost, both CDW satellites and Bragg reflections

[2]If z is a stochastic variable drawn from a Gaussian distribution e^{-z^2}, then

$$\langle e^{iqz}\rangle = e^{-\frac{1}{2}q^2\langle z^2\rangle} \tag{B.5}$$

for any arbitrary real number q. Known as the Baker-Hausdorff theorem, this result can quickly be checked by expanding the left-hand side into a Taylor series up to second order.

suffer. We will first determine how a CMW phase can affect x-ray scattering. Technically speaking, the effect is as simple as adding a phase ϕ_E into the cosine function in Eq (B.1) and recalculating the cross-section. Repeating what we have done in Eq (B.3), we come up with

$$\left(\frac{d\sigma}{d\Omega}\right)_{\text{CMW}} = Nr_0^2 \left(|f|^2 \sum_{\mathbf{R}} e^{i\mathbf{Q}\cdot(\mathbf{R}-\mathbf{R}_0)} + \frac{|\tilde{f}|^2}{4} \sum_{\mathbf{R}} e^{i\mathbf{Q}^+\cdot(\mathbf{R}-\mathbf{R}_0)} \left\langle e^{i[\phi_E(\mathbf{R})-\phi_E(\mathbf{R}_0)]} \right\rangle + \frac{|\tilde{f}|^2}{4} \sum_{\mathbf{R}} e^{i\mathbf{Q}^-\cdot(\mathbf{R}-\mathbf{R}_0)} \left\langle e^{-i[\phi_E(\mathbf{R})-\phi_E(\mathbf{R}_0)]} \right\rangle \right) \quad \text{(B.8)}$$

where $\mathbf{Q}^{\pm} = \mathbf{Q} \pm \mathbf{k}_{\text{CDW}}$. Because of the phase, the satellite reflections no longer appear as simple lattice sums. Instead, they contain an averaged phaser, which, according to the Baker-Housdorff theorem, can immediately be recast and becomes $\exp[-(1/2)\mathcal{G}_E(\mathbf{R}, \mathbf{R}_0)]$. It is evident that the correlation arises out of the average introduced in Eq (B.3). Physically, the CMW is different with respect to each reference point $\mathbf{R}_0$. X-ray scattering measures the characteristic length with which the CMW varies its phase.

Being the cross-section for only the CMW component of a CDW, Eq (B.8) can still be manipulated so it includes the LDW component as well. We have explained how such an inclusion can be done in Section 4.1.3. To reflect the LDW, we substitute the lattice coordinate $\mathbf{R}$ with $\mathbf{R} + \mathbf{u}_0 \sin(\mathbf{k}_{\text{CDW}} \cdot \mathbf{R} + \phi_L)$, where ϕ_L again becomes a local offset of the LDW position. We will therefore need the average

$$\left\langle \sum_{\mathbf{R}} e^{i\mathbf{X}\cdot\left(\mathbf{R}+\mathbf{u}_0 \sin(\mathbf{k}_{\text{CDW}}\cdot\mathbf{R}+\phi_L(\mathbf{R}))-\mathbf{R}_0-\mathbf{u}_0 \sin(\mathbf{k}_{\text{CDW}}\cdot\mathbf{R}_0+\phi_L(\mathbf{R}_0)) \right)} \right\rangle \approx |J_0|^2 \sum_{\mathbf{R}} e^{i\mathbf{X}\cdot(\mathbf{R}-\mathbf{R}_0)} + |J_1|^2 \sum_{\mathbf{R}} e^{i\mathbf{X}^+\cdot(\mathbf{R}-\mathbf{R}_0)} \left\langle e^{i[\phi_L(\mathbf{R})-\phi_L(\mathbf{R}_0)]} \right\rangle + |J_1|^2 \sum_{\mathbf{R}} e^{i\mathbf{X}^-\cdot(\mathbf{R}-\mathbf{R}_0)} \left\langle e^{-i[\phi_L(\mathbf{R})-\phi_L(\mathbf{R}_0)]} \right\rangle \quad \text{(B.9)}$$

when computing the lattice sums. In turn the three different reflections in Eq (B.8) will split into nine terms, resulting in Bragg peaks as well as CDW satellite

peaks up to second order. In Eq (B.9), one should recall that we have created those notations such that $\mathbf{X}^{\pm} = \mathbf{X} \pm \mathbf{k}_{\rm CDW}$, whereas $\mathbf{X} = \mathbf{Q}, \mathbf{Q}^{\pm}$; and J_i is the ith-order Bessel function evaluated at $\mathbf{X}\cdot\mathbf{u}_0$. It should be evident that the $|J_1|^2$ terms appearing in Eq (B.9) give us the desired phase correlation $\mathcal{G}_L(\mathbf{R}, \mathbf{R}_0)$ for the LDW.

Let us explicitly write down the cross-section so its structure can be best appreciated. Given that $\mathbf{R}_0$ is just an arbitrary point in the lattice, it is rather convenient to make it coincide with the origin. In turn the two correlations will be functions of $\mathbf{R}$ only, and we will write them as $\mathcal{G}_E(\mathbf{R})$ and $\mathcal{G}_L(\mathbf{R})$, respectively. Around the Bragg reflections, the cross-section is

$$\Big(\frac{d\sigma}{d\Omega}\Big)^{\mathbf{Q}\sim\mathbf{G}}_{\rm CDW} = Nr_0^2\Big(|f|^2\cdot|J_0(\mathbf{Q}\cdot\mathbf{u}_0)|^2\sum_{\mathbf{R}} e^{i\mathbf{Q}\cdot\mathbf{R}} + |\tilde{f}|^2\cdot\frac{|J_1(\mathbf{Q}^+\cdot\mathbf{u}_0)+J_1(\mathbf{Q}^-\cdot\mathbf{u}_0)|^2}{4}\sum_{\mathbf{R}} e^{i\mathbf{Q}\cdot\mathbf{R}}e^{-\frac{1}{2}[\mathcal{G}_L(\mathbf{R})+\mathcal{G}_E(\mathbf{R})]}\Big) \quad \text{(B.10)}$$

The two correlations are combined, and together they appear in the second term only. Because correlations decay with $\mathbf{R}$, the corresponding lattice sum extends only over a finite range. Consequently the second term will have an appreciable width, with its contribution known as diffuse scattering. According to this result, the CMW yields only diffuse scattering around the Bragg reflections.

In contrast to the Bragg reflections, things are much more interesting at the CDW satellite reflections. For the primary CDW satellite reflections located at $\mathbf{G}\mp\mathbf{k}_{\rm CDW}$, we find the cross-section

$$\Big(\frac{d\sigma}{d\Omega}\Big)^{\mathbf{Q}\sim\mathbf{G}^{\mp}}_{\rm CDW} = Nr_0^2\Big(|f|^2\cdot|J_1(\mathbf{Q}\cdot\mathbf{u}_0)|^2\sum_{\mathbf{R}} e^{i\mathbf{Q}^{\pm}\cdot\mathbf{R}}e^{-\frac{1}{2}\mathcal{G}_L(\mathbf{R})} + |\tilde{f}|^2\cdot\frac{|J_0(\mathbf{Q}^{\pm}\cdot\mathbf{u}_0)|^2}{4}\sum_{\mathbf{R}} e^{i\mathbf{Q}^{\pm}\cdot\mathbf{R}}e^{-\frac{1}{2}\mathcal{G}_E(\mathbf{R})}\Big) \quad \text{(B.11)}$$

Here, the two correlations appear separately. The $|J_1|^2$ term is related to the LDW. Diffuse scattering of this term is set by the LDW correlation $\mathcal{G}_L(\mathbf{R})$. Similarly, the

$|J_0|^2$ term is the CMW contribution in the x-ray scattering. This term too appears with the form of diffuse scattering, and $\mathcal{G}_E(\mathbf{R})$ of the CMW is the only correlation that matters for this term. Indeed, we regard Eq (B.11) as a notable result. It says that the CMW and the LDW are independent at these satellite reflections.

Yet there are still more reflections to be found at $\mathbf{G} \mp 2\mathbf{k}_{\text{CDW}}$. The cross-section of these secondary satellite reflections is determined to be

$$\left(\frac{d\sigma}{d\Omega}\right)_{\text{CDW}}^{\mathbf{Q}\sim\mathbf{G}^{\mp\mp}} = Nr_0^2\,|\tilde{f}|^2 \cdot \frac{|J_1(\mathbf{Q}^{\pm}\cdot\mathbf{u}_0)|^2}{4} \sum_{\mathbf{R}} e^{i\mathbf{Q}^{\pm\pm}\cdot\mathbf{R}} e^{-\frac{1}{2}[\mathcal{G}_L(\mathbf{R})+\mathcal{G}_E(\mathbf{R})]} \tag{B.12}$$

where by $\mathbf{Q}^{\pm\pm}$ we mean $\mathbf{Q} \pm 2\mathbf{k}_{\text{CDW}}$. For the secondary satellite reflections, diffuse scattering is due to the combination of $\mathcal{G}_L(\mathbf{R})$ and $\mathcal{G}_E(\mathbf{R})$. The fact that this cross-section is proportional to $|J_1|^2$ indicates these reflections are much weaker than the second term in Eq (B.11).

Measuring the CMW correlation $\mathcal{G}_E(\mathbf{R})$

From Eq (B.10) – (B.12) we determine that the primary satellite reflections are the only place where the structure of the CMW can be measured independent from the LDW. Given that $|\tilde{f}|^2$ peaks around the Fermi energy, diffuse scattering of the CMW appears only if we can tune x-ray energy to the right point. One can therefore compare diffuse scattering measured at and off the Fermi energy. Any change in the line shape will indicate the CMW has a different correlation from the LDW. Pervious work on line shape analysis shows that diffuse scattering of the LDW can be fit to a pseudo-Voigt line shape, which is actually a mixture of a Gaussian and a Lorentzian function [9]. As we anticipate the CMW corresponds to a similar line shape, our line shape analysis really depends on how much scattering in the satellite reflections is created by the CMW and not by the LDW. We rely on optimized experimental conditions so any changes in the rather-generalized line shape can be properly detected and measured.

APPENDIX C

X-RAY PROPERTIES OF THE C1 BEAMLINE AT CHESS

During our experiments at CHESS, we carefully characterized the x-ray properties of the C1 beamline. Here we discuss our methods of determining the energy resolution and the polarization purity at C1.

Energy resolution

The radiation generated by the synchrotron source contains a wide range of wavelengths. It is therefore commonly referred to as a white beam. As the key component of the beamline, the monochromator selectively passes a narrow wavelength band $\Delta\lambda$. By taking derivative of the Bragg Law, we immediately see that

$$\frac{\Delta\lambda}{\lambda} = \frac{\Delta\theta}{\tan\theta} \tag{C.1}$$

where θ is the monochromator angle, and $\Delta\theta$ is the (effective) angular bandwidth of the white beam. In our experiments the throughput of the monochromator was tailored by the sample slits of a size equal to $500\mu\text{m} \times 500\mu\text{m}$. We calculated the angular bandwidth

$$\Delta\theta = \frac{\sqrt{(1.5\text{ mm})^2 + (0.5\text{ mm})^2}}{14500\text{ mm}} \approx 1.09 \times 10^{-4}\text{rad}$$

Inside the square root 1.5 mm is the size of the electron beam; in the denominator 14500 mm is the distance between the source and the sample slits. This number can then be plugged in Eq (C.1). At the Ta-L_3 edge, x-ray energy $E = 9.881$KeV. Because $\Delta\lambda/\lambda = -\Delta E/E$, the energy resolution is given by $|\Delta E| = 1.09 \times 10^{-4} \tan\theta \times E$, which is a function of the monochromator angle θ.

At 9.881KeV, a Si(220) monochromator corresponds to a Bragg angle equal to 19.0722°. For this monochromator, $|\Delta E| = 3.11$ eV. On the other hand, if we use

a Si(111) monochromator, the Bragg condition is satisfied at $\theta = 11.5427°$. With this Bragg angle, we would get a slightly larger energy resolution $|\Delta E| = 5.27$ eV.

From this discussion about the energy resolution, it is clear that $|\Delta E|$ is primarily determined by the size of the electron beam at the C1 beamline. The sample slits only tailor the energy resolution in a less important manner. One can ask what is the corresponding value of the energy resolution if we do not use any defining slit at all. In April 2008, we went back to the beamlime and performed a measurement. We diffracted x-ray by a Si(220) crystal in both the non-dispersive geometry and the dispersive geometry. See the discussion of Figure C.1. With the angular bandwidth $\Delta\theta \sim 0.0072°$, we determined that $|\Delta E| \sim 3.42$ eV when the Si(220) monochromator is operated at 9.660KeV.

Polarization property

Using the polarimeter we can measure the polarization purity of the x-ray beam at C1. Figure C.2 shows an example of such measurements that we have performed at the beamline, assuming a Si(220) monochromator was used to produce the monochromatic x-ray beam. The degree of linear polarization (D.L.P.) is defined to be [10]

$$\text{D.L.P.} = \frac{(I_\sigma^{\text{int}} - I_\pi^{\text{int}})}{(I_\sigma^{\text{int}} + I_\pi^{\text{int}})} \tag{C.2}$$

Knowing that the angular acceptance of the analyzer crystal was small compared to the angular divergence of the x-ray beam, we rotated the analyzer crystal and measured the rocking curves of the two x-ray components polarized both perpendicular (σ) and parallel (π) to the vertical diffraction plane. In Eq (C.2), I^{int} stands for the integrated intensities of the rocking curves. In those measurements, it was very important that the rocking curves were measured over a sufficiently large

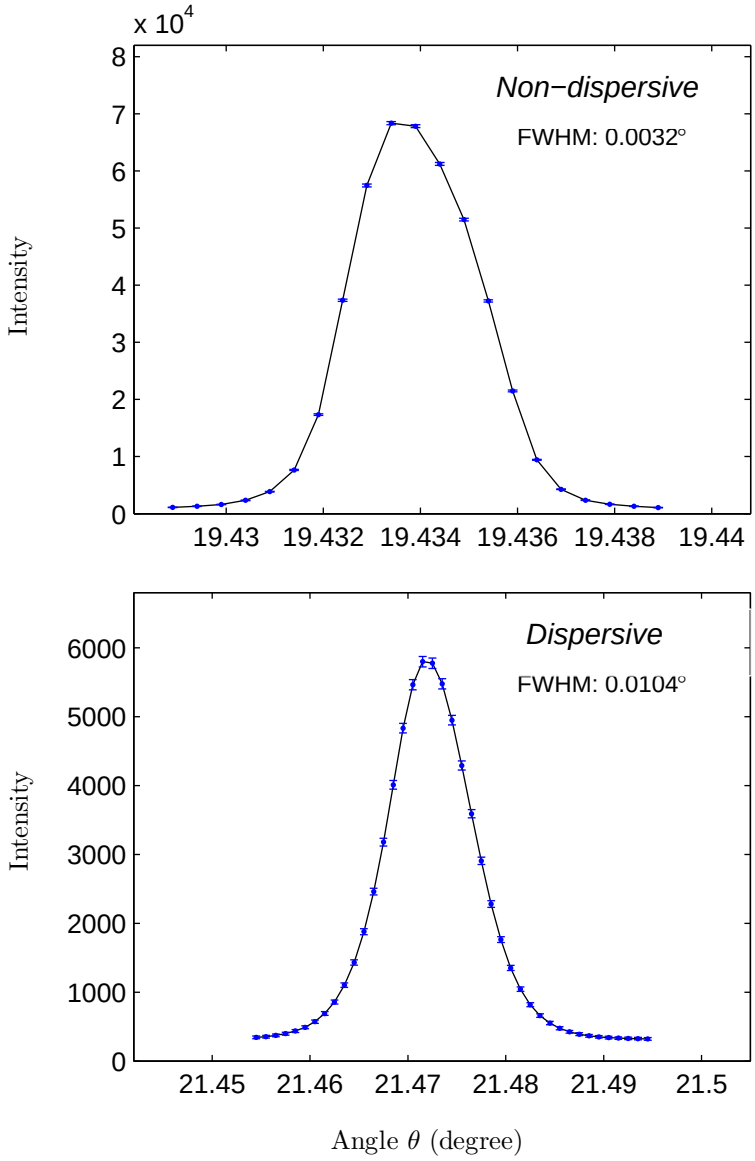

Figure C.1: Rocking curves of the (220)-reflection of a Si (220)-cut crystal, measured at 9.660 KeV in the non-dispersive geometry (top) and the dispersive geometry (bottom), corresponding to a beamline setup without and with the x-ray mirror, respectively. (As we have changed the direction of the x-ray beam, the absolute values of the angles in these scans are not important.) From these scans we can determine the angular bandwidth, which is the difference of the two FWHMs (page 200, Ref [3]). Lines are drawn to guide the eye.

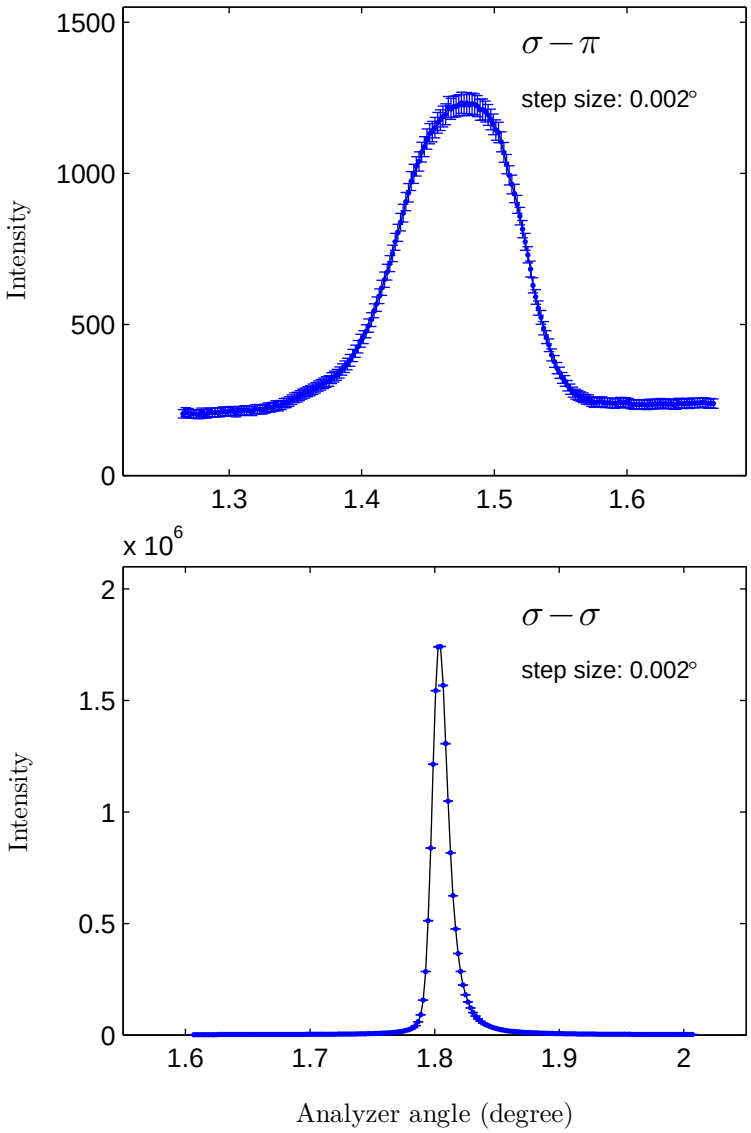

Figure C.2: Rocking curves of the (620)-reflection of the (111)-cut Ge crystal as the analyzer. The monochromatic x-ray beam was produced by the Si(220) monochromator at the C1 beamline. In the case of π–π (σ–σ) scattering, reflection by the analyzer took place in the horizontal (vertical) plane. There are 200 points in each scan. The integrated intensities are the areas under these curves subtract the background. Lines are drawn to guide the eye.

range so the background level could be properly determined. Also we recognized that in the case of $\sigma-\pi$ scattering, the footprint of the x-ray beam on the analyzer crystal became unfavorably large because the horizontally diverging beam hit the crystal at a rather shallow incident angle ($\sim 1^{\circ}$). In turn, our detector only captured approximately one third of reflection coming from the analyzer crystal. In Figure C.2, I_{π}^{int} becomes underestimated by about 67%.

According to our polarization analysis, we determined that the D.L.P. was $\sim 98\%$ when we used the Si(220) monochromator at the beamline. A similar measurement like Figure C.2 shows that the D.L.P. was $\sim 96.5\%$ when the monochromatic beam was produced by the Si(110) monochromator instead.

BIBLIOGRAPHY

[1] J. J. Sakurai. *Advanced quantum mechanics.* Addison-Wesley Publishing Company, MA, 1967. Chapter 2.

[2] M. Blume. *Resonant Anomalous X-ray Scattering: Theory and Applications*, pages 495–512. North-Holland, 1994.

[3] Jens Als-Nielsen and Des McMorrow. *Elements of modern X-ray physics.* John Wiley and Sons Ltd, New York, 2001.

[4] Rubin H. Landau. *Quantum Mechanics II : A Second Course in Quantum Theory.* Wiley, New York, 2nd edition, 1996. Chapter 20 and 21.

[5] Stephen Gasiorowicz. *Quantum physics.* Wiley, New York, 2nd edition, 1996. Chapter 16.

[6] André Guinier. *X-ray Diffraction in Crystals, Imperfect Crystals, and Amorphous Bodies.* W. H. Freeman, New York, 1963.

[7] E. Sweetland, C-Y. Tsai, B. A. Wintner, J. D. Brock, and R. E. Thorne. Measurement of the charge-density-wave correlation length in $NbSe_3$ by high-resolution x-ray scattering. *Phys. Rev. Lett.*, 65(25):3165–3168, Dec 1990.

[8] J. D. Brock, A. C. Finnefrock, K. L. Ringland, and E. Sweetland. Detailed structure of a charge-density wave in a quenched random field. *Phys. Rev. Lett.*, 73(26):3588–3591, Dec 1994.

[9] Kristin Lee Ringland. *The Structure and Kinetics of Charge Density Waves.* PhD thesis, Cornell University, January 2000. Section 4.3.

[10] Doon Gibbs, D. R. Harshman, E. D. Isaacs, D. B. McWhan, D. Mills, and C. Vettier. Polarization and Resonance Properties of Magnetic X-Ray Scattering in Holmium. *Phys. Rev. Lett.*, 61(10):1241–1244, Sep 1988.